# UC Berkeley
## UC Berkeley Electronic Theses and Dissertations

**Title**
Integrated Nanoscale Antenna-LED for On-Chip Optical Communication

**Permalink**
https://escholarship.org/uc/item/1d31s4p6

**Author**
Fortuna, Seth Andrew

**Publication Date**
2017

Peer reviewed|Thesis/dissertation

# Integrated Nanoscale Antenna-LED for On-Chip Optical Communication

by

Seth Fortuna

A dissertation submitted in partial satisfaction of the

requirements for the degree of

Doctor of Philosophy

in

Engineering - Electrical Engineering and Computer Sciences

in the

Graduate Division

of the

University of California, Berkeley

Committee in charge:

Professor Ming C. Wu, Chair
Professor Eli Yablonovitch
Professor Jie Yao

Summer 2017

# Integrated Nanoscale Antenna-LED for On-Chip Optical Communication

# Abstract

Integrated Nanoscale Antenna-LED for On-Chip Optical Communication

by

Seth Fortuna

Doctor of Philosophy in Engineering - Electrical Engineering and Computer Sciences

University of California, Berkeley

Professor Ming C. Wu, Chair

Traditional semiconductor light emitting diodes (LEDs) have low modulation speed because of long spontaneous emission lifetime. Spontaneous emission in semiconductors (and indeed most light emitters) is an inherently slow process owing to the size mismatch between the dipole length of the optical dipole oscillators responsible for light emission and the wavelength of the emitted light. More simply stated: semiconductors behave as a poor antenna for its own light emission.

By coupling a semiconductor at the nanoscale to an external antenna, the spontaneous emission rate can be dramatically increased alluding to the exciting possibility of an antenna-LED that can be directly modulated faster than the laser. Such an antenna-LED is well-suited as a light source for on-chip optical communication where small size, fast speed, and high efficiency are needed to achieve the promised benefit of reduced power consumption of on-chip optical interconnect links compared with less efficient electrical interconnect links.

Despite the promise of the antenna-LED, significant challenges remain to implement an antenna-coupled device in a monolithically integrated manner. Notably, most demonstrations of antenna-enhanced spontaneous emission have relied upon optical pumping of the light emitting material which is useful for fundamental studies; however, an electrical injection scheme is required for practical implementation of an antenna-LED.

In this dissertation, demonstration of an electrically-injected III–V antenna-LED is reported: an important milestone toward on-chip optical interconnects.

In the first part of this dissertation, the general design principles of enhancing the spontaneous emission rate of a semiconductor with an optical antenna is discussed. The cavity-backed slot antenna is shown to be uniquely suited for an electrically-injected antenna-LED because of large spontaneous emission enhancement, simple fabrication, and directional emission of light.

The design, fabrication, and experimental results of the electrically-injected III–V antenna-LED is then presented. Clear evidence of antenna-enhanced electroluminescence is demonstrated including a large increase in the emitted light intensity with respect to an LED without antenna. Furthermore, it is shown that the active region emission wavelength is

influenced by the antenna resonance and the emitted light is polarized; consistent with the expected behavior of the cavity-backed slot antenna. An antenna-LED consisting of a InGaAs quantum well active region is shown to have a large 200-fold enhancement of the spontaneous emission rate.

In the last half of this dissertation, the performance of the antenna-LED is discussed. Remarkably, despite the high III–V surface recombination velocity, it is shown that an efficient antenna-LED consisting of an InGaAs active region is possible with an antenna-enhanced spontaneous emission rate. This is true provided the active region surface quality is preserved through the entire device process. A novel technique to preserve and clean InGaAs surfaces is reported. Finally, a rate-equation analysis shows that the optimized antenna-LED with cavity-backed slot antenna is fundamentally capable of achieving greater than 100 GHz direct modulation rate at high efficiency thus showing that an antenna-LED faster than the laser is achievable with this device architecture.

To Grandpap and Pampa

You taught me so much about how to be a good man.

# Contents

# List of Figures

# List of Tables

# Acknowledgments

I owe a large debt of gratitude to a significant number of people that have been instrumental either directly or indirectly to the research contained in this dissertation.

I have had the great privilege to be mentored by my graduate advisor Professor Ming C. Wu. I am grateful for Prof. Wu's guidance and support throughout my time here at Berkeley. I feel just as excited and motivated today about this project as I did the first day I walked in your office.

Thank you Professor Eli Yablonovitch for many inspiring discussions and being an advocate for this work. Thank you both to Professor Chang-Hasnain and Professor Yablonovitch for serving on my prelim and qual committees. Thank you also to Professor Jie Yao for serving on my dissertation committee. I would also like to acknowledge my masters degree advisor, Professor Xiuling Li from UIUC for her guidance over the years.

I would like to specifically acknowledge several students that I have worked with directly on this project: Michael Eggleston, Christopher Heidelberger, Kevin Messer, Kevin Han, Nicolas Andrade, and Sean Hooten. In general, thank you to many of the students and post-docs in the Chang-Hasnain, Yablonovitch, and Wu groups for technical help and many friendships over the years. Special thank you to the Albatross trivia team: Michael, Kevin, Anita Shankar, Vidya Ganapati, Amy Bergerud, Ben Rattle, and Jared Carter.

None of this research would be possible without the administrative staff from $E^3S$, BSAC, and the EECS department. Special thank you to Therese George for tolerating my unscheduled appearances at her office for help.

Thank you to the staff of the Marvell Nanolab and your dedication to running such a professional academic facility.

I must acknowledge several colleagues from industry that have helped to shape my early career: Jeremy Rowlette, Michael DiBattista, Andy Kurtz, Cameron Wagner, Vincent Nguyen, and Sungwook Huh. I hope you can forgive me for not doing a better job of staying in contact with all of you!

Thank you to my family for your encouragement, support, and love.

Finally, thank you to my fiancée Emily. One journey in life has come to an end. Another journey begins with you very soon. I can't wait.

# Chapter 1

# Introduction

Over three billion people – nearly half the population of humans on this planet – are connected to the internet. Every minute, over 200 million e-mail messages, 5 million Google searches, and 350,000 tweets traverse the internet [1]. Six billion devices such as TVs, kitchen appliances, and smart electric meters composing the "Internet of Things" were connected to the internet in 2016 with that number expected to triple by early next decade [2]. Within the same time frame, it is expected that $\approx 80\%$ of all consumer internet traffic will consist of streaming video; much of it high definition. Total internet traffic in 2016 was estimated at 1.2 zettabytes ($10^{21}$ bytes) and expected to grow three-fold by 2021 [3].

The increase in internet traffic has been paralleled by the rise of hyper-scale data centers which increasingly provide the computing and storage for e-commerce, content streaming, social networking, and cloud computing. It has been estimated that for every one bit of data traversing the internet, $10^6$ bits are communicated inside data centers [4]. The energy required to manage all of this data is immense: in the United States alone, 70 billion kilowatt-hours annually (the equivalent energy output of 8 nuclear reactors) are needed to power the roughly 12 million computer servers that comprise data centers [1]. At \$0.10 per kilowatt-hour, this amounts to roughly \$7 billion in annual energy costs [5]. Major technological innovations are needed to support the increasing bandwidth demand while minimizing energy costs. High-bandwidth and energy efficient optical interconnect links will play a critical role.

## 1.1 Energy efficiency through optical communication

Most of the energy usage in a data center (and computing in general) is the result of moving data from one point to another [6], [7]. The minimum amount of energy needed to move a bit of data through an electrical interconnect is fundamentally limited by the energy needed to charge and discharge the interconnect capacitance [6], [7]. There is no equivalent capacitance for an optical interconnect and therefore the fundamental minimum amount of energy is essentially the energy of the photons themselves plus any additional energy needed for electrical-to-optical and optical-to-electrical conversion. Because of reduced energy cost

per bit and high-bandwidth, optical interconnects have already replaced traditional copper electrical interconnects within advanced data centers for short-reach distances on the order of meters (e.g. server rack-to-rack communication). However, any serious attempt at reducing energy consumption in the data center also requires replacement of electrical interconnects that are still predominantly used for board-to-board, chip-to-chip, and ultimately on-chip communication.

## On-chip optical interconnects
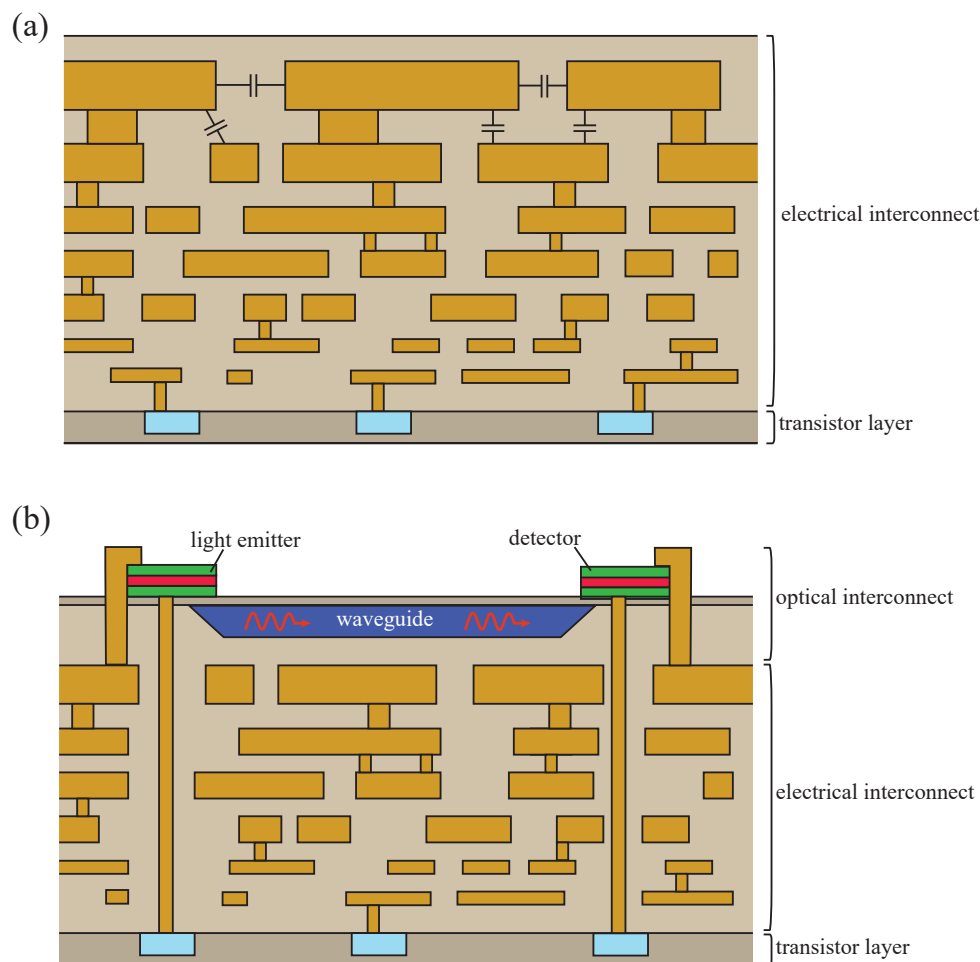


Figure 1.1: (a) Cross-section cartoon drawing of a typical modern CPU showing the chip is composed primarily of electrical interconnects; and (b) one possible implementation of an optical interconnect on-chip. Drawing inspired by [8].

Shown in Figure 1.1a is a simplified cross-section of a modern CPU. The majority of the chip contains 10 or more electrical interconnect layers for data communication with a thin

transistor layer for data processing. Communicating a bit of data on-chip requires charging and discharging the capacitance of the interconnect line ($C_l$) and transistor gate capacitance ($C_G$) with energy per bit of operation approximately given by

$$E_{bit} = (C_G + C_l)V^2 \tag{1.1}$$

where $V$ is the supply voltage. Within the past decade, two scaling trends have emerged:

1. The transistor size has scaled considerably such that $E_{bit} \approx C_l V^2$ for all but the shortest interconnect lengths.

2. Voltage supply scaling has stopped near 1 $V$ to maintain a reasonable on/off ratio.

For a typical interconnect capacitance of 2 pF/cm [9] and a 1 V power supply, the energy per bit for an electrical interconnect is estimated as $E_{bit} \approx C_l V^2 = 2$ pJ/bit/cm.

Consider now the situation in Figure 1.1b where one or more of the electrical interconnects have been replaced by an optical interconnect which consists of some light emitter, optical waveguide, and photodetector. Assuming the optical link can operate at the quantum limit, 20 photons are needed to represent a bit of information [10] and the fundamental minimum energy per bit is $\approx (20\frac{\text{photons}}{bit})(1\frac{eV}{photon})q = 3$ aJ/bit. Therefore, for all but the shortest interconnect lengths, on-chip optical interconnects are fundamentally more efficient than electrical interconnects. By replacing electrical interconnects with optical interconnects, significant reduction in the energy per bit can be achieved.

## 1.2   Light source for on-chip optical interconnects

There are generally two choices for an on-chip light emitter: (1) a device that emits spontaneous emission (i.e. a light emitting diode), or (2) a device that emits stimulated emission (i.e. a laser). Both devices need to fulfill three general design requirements:

1. **Nanoscale size**. This is important for several reasons. From a geometric point-of-view, small size means we can integrate more devices per unit area. From a power point-of-view, smaller size usually means smaller operating power and potentially less energy per bit. Particularly important for a light emitting diode, nanoscale size will ensure a single spatial mode and allow for efficient coupling to an on-chip waveguide. Finally, nanoscale implies that the light emitting device is directly modulated and does not need a bulky external modulator.

2. **Fast**. At a minimum, the device should be capable of direct modulation at the switching speed of a transistor. This is roughly 3 ps for the latest technology node which corresponds to $\approx 50$ GHz modulation speed [6]. Ideally, the modulation speed should be higher to accommodate faster transistor switching speeds in the future.

3. **Low energy per bit**. The emitter should be capable of consuming $< 100$ aJ/bit. This ultimately depends on the sensitivity of the photodetector and total optical link budget.

4. **Integrated**. The light emitting device needs to be coupled to an on-chip waveguide and, importantly, needs to electrically-injected.

Temporal coherence of light emission is not a requirement, nor is it compatible with the highest modulation bandwidth in any case. Waveguide dispersion is minimal at the optical interconnect length scales considered here ($\approx 1$ cm or less)[1]. Therefore a light emitting diode with broadband emission is acceptable and is compatible with coarse wavelength division multiplexing.

## Laser as a light source
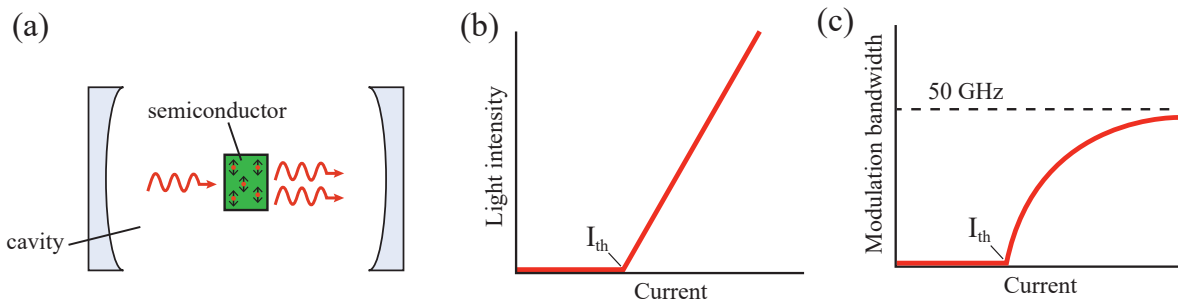


Figure 1.2: (a) Simple diagram of laser; (b) light intensity vs. current (L-I curve) for the laser; and (c) modulation bandwidth of the laser as a function of current

Perhaps the obvious approach for making an on-chip light emitter is to scale down the semiconductor laser into the nanoscale regime. The general characteristics of the laser are shown in Figure 1.2 and consist of some gain medium placed inside a resonant cavity. Presuming the gain medium consists of a semiconductor material, we must inject enough electron-hole pairs to reach the threshold condition before any usable light leaves the device (Figure 1.2b). Just above threshold, the photon density is small and the speed of the laser is slow (Figure 1.2c). The speed can be increased by injecting more electron-hole pairs up to a point before the gain eventually saturates; typically around 50 GHz [12]. Thus, the laser has inherently high energy per bit: some minimum amount of current needs to be injected to achieve the threshold condition and high injected current is needed to achieve high speed.

---

[1]Typical group velocity dispersion of a silicon photonic waveguide is about 4000 ps/(nm·km) [11]. The maximum bit rate ($B$) with the inclusion of dispersion is given by $B \approx [(\text{interconnect length})(\text{dispersion})(\text{spectral width})]^{-1}$ [10]. Assuming a broadband light source such as a light emitting diode with spectral width of $\approx 200$ nm at $\lambda_0 = 1.55$ $\mu$m, the maximum bit rate is calculated to be greater than 100 Gbps for a 1 cm long optical interconnect.

Scaling the laser into the nanoscale regime is challenging because the cavity needs to be sized such that the photons remain in the cavity long enough to contribute to stimulated emission. Unfortunately, physics works against us: photons cannot be confined to a dielectric cavity volume less than $\approx (\lambda_0/2n)^3$ according to the diffraction limit. Even before reaching this limit, the photons will leak out too fast before an appropriate photon density can be built up in the cavity. Surrounding the cavity with metal can help confine the photons but will increase the loss and energy per bit from the presence of lossy metal [13]–[24]. Photonic crystal lasers can be used to confine light near the diffraction limit and have been used to demonstrate fJ/bit operation at multi-GHz modulation speeds but have inherently large footprint and therefore do not meet the nanoscale size requirement [25]–[29].

## LED as a light source
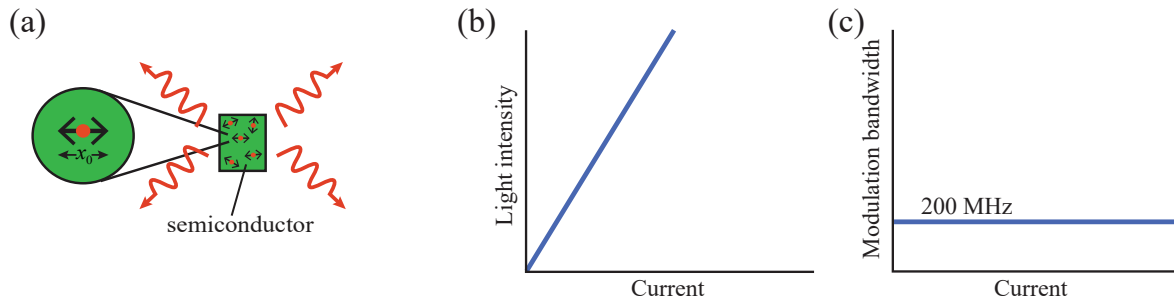


Figure 1.3: (a) Simple diagram of light emitting diode (LED); (b) light intensity vs. current (L-I curve) for the LED; and (c) modulation bandwidth of the LED as a function of current

Unlike the laser, the light emitting diode (LED) (Figure 1.3) does not need a cavity to confine photons and is easily scaled into the nanoscale regime. There is no threshold current requirement and the quantum efficiency of a well-designed LED can approach 100% [30]. As shown in Figure 1.3c the spontaneous emission lifetime is independent of photon density and therefore independent of drive current[2]. Unfortunately, the spontaneous emission lifetime is rather long ($\approx 1$ ns) and the direct modulation rate of the LED is limited to about 200 MHz. Thus, despite a number of other desirable qualities, the LED has largely been overlooked as an optical communication device in favor of the laser and the faster stimulated emission process.

### Increasing the spontaneous emission rate with an antenna

Why is spontaneous emission so slow? As shown in the inset of Figure 1.3, we can model spontaneous emission from electron-hole recombination as classical radiation from small ac

---

[2]In a semiconductor, the behavior shown in Figure 1.3b is strictly true in the low-injection regime where the minority carrier density is much lower than the majority carrier density. More on this in Chapter 6.

dipole current sources in the semiconductor where the length of the dipole emitter ($x_0$) is roughly equal to the lattice constant of the material ($x_0 \approx 0.5$ nm). It is well-known from antenna theory that a current source radiates most efficiently when its size is $\approx \lambda_0/2$. Since $x_0 \ll \lambda_0$, the spontaneous emission rate is low and the semiconductor slowly radiates the energy stored in the dipole emitter.
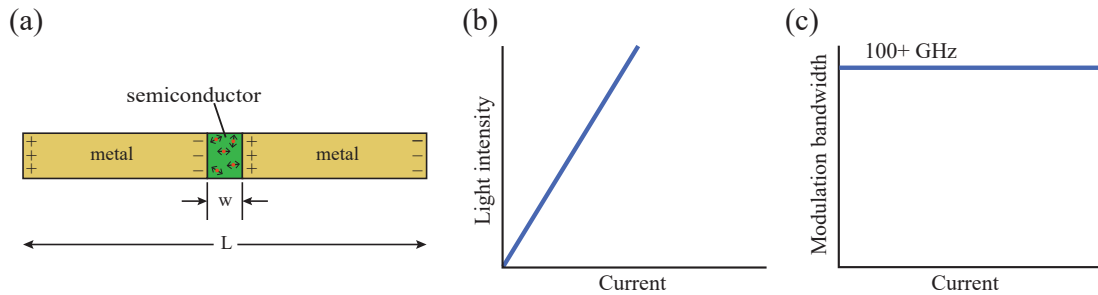


Figure 1.4: (a) Antenna-coupled LED (antenna-LED); (b) light intensity vs. current (L-I curve) for the antenna-LED; and (c) modulation bandwidth of the antenna-LED as a function of current.

For a given material and wavelength our only hope to increase the spontaneous emission rate is then to somehow increase the dipole length ($x_0$). This is achieved by coupling the slowly radiating semiconductor dipoles to a much better radiator such as a $\lambda_0/2$ dipole metal antenna (Figure 1.4a). Here the semiconductor is now placed in the feedgap of the dipole antenna. The ac dipole currents in the semiconductor will induce charge of opposite polarity on either side of the feedgap inducing a current to flow along the antenna arms. If the antenna is properly designed such that the length is $L \approx \lambda_0/2$, the antenna will efficiently radiate into the far-field. Thus the potential energy that is stored in the dipole moment (i.e. the electron-hole pair) is rapidly converted into radiated energy in an efficient manner and the spontaneous emission rate is significantly enhanced.

It will be shown later, that the spontaneous emission rate enhancement factor from the antenna is $\propto \left(\frac{L}{w}\right)^2$ where $w$ is the antenna feedgap width. For highly scaled antenna gap spacing ($w < 20$ nm), the increase in the spontaneous emission rate can easily exceed 1000-fold. Thus the original semiconductor with spontaneous emission lifetime of $\approx 1$ ns can have a lifetime shorter than 1 ps allowing direct modulation rates exceeding 100 GHz when coupled to an an antenna (Figure 1.4c). Using an antenna, it is possible to make an LED faster than the laser!

# 1.3 Toward an integrated antenna-LED for on-chip optical communication

The antenna-coupled LED (antenna-LED) is nanoscale and capable of fast and efficient operation and therefore meets most of our requirements for on-chip optical interconnects. But what about integrating the antenna-LED on-chip? There have been many demonstrations of antenna-enhanced spontaneous emission using single molecules [31]–[36], quantum dots [37]–[39], and other solid-state materials [40]–[44] but there has been minimal progress in implementing an antenna-coupled device in a monolithically integrated manner that is suitable for on-chip communication.

Notably, most demonstrations of antenna-enhanced spontaneous emission have relied upon optical pumping of the light emitting material as illustrated in Figure 1.5a. Optical pumping is useful for fundamental studies; however, for a practical antenna-LED an electrical injection scheme is required. It is not obvious how to implement an electrical contact as shown Figure 1.5b in a manner that does not perturb the antenna mode while still allowing for high spontaneous emission enhancement.
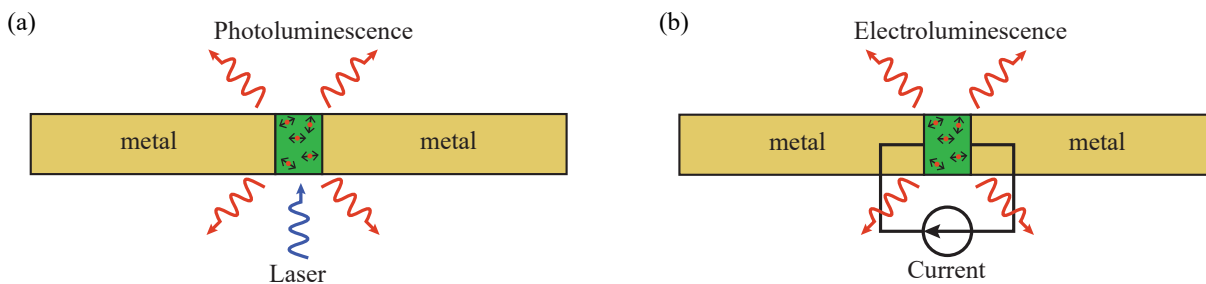


Figure 1.5: (a) Optical pumping antenna-coupled device and emission of photoluminescence; and (b) electrical injection of antenna-coupled device and emission of electroluminescence.

## Requirements for the electrically-injected antenna-LED

A few general design requirements for the successful implementation of an electrically-injected antenna-LED can be outlined:

1. **Electrical contact must not perturb antenna-mode.** The placement of electrical contacts must be done in a manner that does not reduce the spontaneous emission enhancement or unpredictably shift the antenna resonance.

2. **Easily integrated**. Repeatable and deterministic placement of the active region within the antenna feedgap is needed. This requires top-down fabrication and excludes the use of randomly dispersed antenna structures or light emitters.

3. **Low contact resistance and capacitance**. The RC-time constant of the antenna-LED must be shorter than the spontaneous emission lifetime.

4. **High device efficiency**. $< 100$ aJ/bit operation is desired.

5. **High spontaneous emission enhancement**. Ideally, the antenna-LED should be capable of operating faster than the laser with modulation speed exceeding 50 GHz.

Early attempts to increase the spontaneous emission rate of large-area electrically-injected quantum well LEDs relied on embedded metal nanoparticles [45], [46] or a flat metal sheet adjacent to the active region [47]–[50] but had limited success because of weak emitter-antenna coupling or low radiative efficiency. Electrically-pumped semiconductor LED structures coupled to metallic waveguides have been demonstrated although none of these reports show larger then 10-fold spontaneous emission enhancement [51]–[55]. Electrically-injecting a nanoscale metal-insulator-metal tunnel junction coupled to an optical antenna is an unusual photon emission mechanism, but the efficiency of such a device is expected to be limited to $\approx 1\%$ [56], [57].

New approaches to electrical-injection are clearly needed before the antenna-LED is suitable as an on-chip light source for optical interconnects.

## 1.4 Outline of this dissertation

In this dissertation, I report on an electrically-injected antenna-LED structure that is suitable for on-chip communication and meets the design requirements outlined above. In Chapter 2, the spontaneous emission lifetime is derived and it is shown that radiative lifetime is not an immutable property but can be modified through engineering of the environment surrounding a light emitter. Specifically, it is shown that a metal antenna can enhance the spontaneous emission rate by more than three orders of magnitude while maintaining reasonable efficiency. In Chapter 3, the behavior of specific antenna structures is discussed and several properties of the cavity-backed slot antenna are shown to make it an ideal choice for an electrically-injected antenna-LED. In Chapter 4, the design, fabrication, and measurement of a III–V antenna-LED coupled to a cavity-backed slot antenna including demonstration of a 200-fold increase in the spontaneous emission rate is reported. In Chapter 5, strategies for increasing the quantum efficiency of the antenna-LED is discussed. High quantum efficiency operation is shown to be possible with the III–V antenna-LED despite a large surface recombination velocity. In Chapter 6, through a rate equation analysis it is predicted that $> 100$ GHz speed with high efficiency is indeed eventually possible with the III–V antenna-LED. Strategies for designing the active region to achieve high speed and efficiency are discussed.

# Chapter 2

# Enhancement of spontaneous emission

Spontaneous emission of light has traditionally been considered a slow process and thus avoided in favor of the faster stimulated emission as a means to communicate information. It was shown by Purcell in his widely-cited work on the transition rate of nuclear magnetic moments [58] that the spontaneous emission lifetime is not an immutable property of an atom or molecule. Rather, the spontaneous emission rate can be increased by placing a radiator inside a resonant cavity which lead to the derivation of his famous Purcell factor.

Several decades after Purcell's work at radio frequencies, nano-fabrication has advanced to the point where the same physics are now being applied to enhance the spontaneous emission rate of light emitting radiators. It is now possible to imagine a light emitting device with spontaneous emission rate faster than the stimulated emission rate: an LED faster than the laser.

In this chapter, the intrinsic spontaneous emission lifetime will first be derived. The Purcell factor will then be derived in the normal manner and re-derived with an equivalent circuit model without invoking the concept of local density of states or mode volume. The equivalent circuit analysis technique will then be used to show that a spontaneous emission enhancement of greater than three orders of magnitude is possible with an optical antenna.

## 2.1 Spontaneous emission lifetime

### Einstein's phenomenological analysis

Consider a simple two-level system shown in Figure 2.1 consisting of an excited energy state with energy $E_1$ and lower ground state with energy $E_2$. Spontaneous emission of light occurs when an electron in the excited state spontaneously jumps to the ground state emitting a photon with energy $\hbar\omega = E_2 - E_1$ in the process to conserve energy (Figure 2.1a). The reverse process may also happen: an electron in the lower state may absorb a photon and jump to the excited state. An electron in the excited state can also be stimulated by another photon to jump to the ground state and release a photon; this process is called stimulated
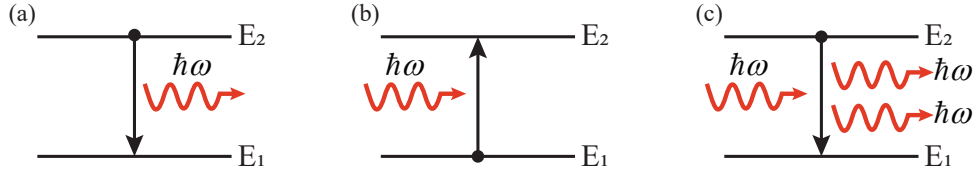
Figure 2.1: Transitions in a two-level system. (a) Spontaneous emission; (b) absorption; and (c) stimulated emission.

emission. Through a simple rate equation approach, Einstein derived relationships between the rates of these three processes [59]. Although his analysis is unable to predict the rates of these processes, it serves as a good starting point for understanding spontaneous emission [60].

Suppose there is an ensemble of such two-level systems placed in a blackbody cavity. The total number of electrons in the ground state is given by $N_1$ and the number of electrons in the excited state is $N_2$; then the rate of change of $N_1$ and $N_2$ can be written

$$\frac{dN_1}{dt} = A_{21}N_2 - B_{12}N_1\rho(\hbar\omega) + B_{21}N_2\rho(\hbar\omega) \tag{2.1}$$

$$\frac{dN_2}{dt} = -A_{21}N_2 - B_{21}N_2\rho(\hbar\omega) + B_{12}\rho(\hbar\omega) \tag{2.2}$$

where $A_{21}$, $B_{12}$, and $B_{21}$ are rate constants associated with the spontaneous emission, absorption, and stimulated emission processes. As described above, spontaneous emission occurs without the presence of a photon, whereas both absorption and stimulated emission require a photon to exist in the cavity. Therefore the rates of absorption and stimulated emission are proportional to the cavity photon density which was given by Planck as

$$\rho(\hbar\omega) = \rho_0(\hbar\omega)n_{ph}(\hbar\omega, T) \tag{2.3}$$

where $\rho_0$ is the density of optical modes in the blackbody cavity and $n_{ph}$ is the Bose-Einstein distribution. Assuming the populations $N_1$ and $N_2$ are in equilibrium with the cavity photon density, (2.1) and (2.2) will both be equal to zero and a relationship between the three rate coefficients can be derived as

$$A_{21} = \rho_0(\hbar\omega)B_{12} \tag{2.4}$$

$$B_{21} = B_{12} \tag{2.5}$$

The transition rate $(s^{-1})$ from the excited state to the ground state $(R_{2\rightarrow1})$ can now be written in a suggestive form as

$$R_{2\rightarrow1} = R_{stim} + R_{spon} \tag{2.6}$$

$$R_{2\rightarrow1} = \rho_0(\hbar\omega)B_{21}\left(n_{ph} + 1\right) \tag{2.7}$$

where the first term is the stimulated emission rate and the second term is the spontaneous emission rate. Several important conclusions from (2.7) are inferred:

- **The transition rate $(R_{2 \to 1})$ is proportional to the optical mode density.** $R_{2 \to 1}$ can be increased if one can find a way to increase $\rho_0(\hbar\omega)$.

- **Stimulated emission is proportional to the photon density** Thus it can be predicted that the speed of the laser is proportional to the photon density in the cavity.

- **Spontaneous emission is equivalent to stimulated emission from a single photon**. Increasing the photon density in the cavity will not increase the spontaneous emission rate. Although Einstein's analysis did not show this, the origin of this photon was shown to be from zero-point fluctuations in the vacuum field [61].

We have now derived expressions to relate the spontaneous emission, absorption, and stimulated emission rates in a two-level system; however, they are written in terms of the Einstein's coefficients $(A_{21}, B_{21}, B_{12})$ which require quantum mechanics to derive. In the next section, the stimulated emission rate coefficient $(B_{21})$ for the two-level system will be derived using quantum mechanics and then used to calculate the spontaneous emission rate $(A_{21})$ from (2.4). In this manner, we avoid directly solving $A_{21}$ which would otherwise require introducing the second quantization and the zero-point vacuum field.

## Fermi's Golden Rule

The transition rate from an initial quantum state $|i\rangle$ to a set of final states $|f\rangle$ for a time-dependent perturbation is given by Fermi's Golden Rule

$$R = \frac{2\pi}{\hbar} \sum_f |H_{fi}|^2. \tag{2.8}$$

where $H_{fi}$ is the matrix element for the light-matter interaction. Under the dipole-approximation, the matrix element for a downward transition from stimulated emission is written

$$|H_{fi}|^2 = \left(\frac{E_0}{2}\right)^2 |x_{fi}|^2 \tag{2.9}$$

where $E_0$ is the amplitude of the perturbing field and $x_{fi}$ is the transition dipole moment

$$x_{fi} = \int_V \psi_f^* x \psi_i dV. \tag{2.10}$$

For simplicity, it assumed that the electric field and dipole moment are polarized in the $\hat{x}$-direction but what follows can be generalized for any polarization.

As in the previous section, we examine a two-level system that is placed inside a blackbody cavity with background photon density given by (2.3). The electrical energy $(U_E)$ from the background radiation inside the cavity is given by

$$U_E = \frac{\epsilon E_0^2}{2} = \frac{\hbar\omega_0}{3}\rho(\hbar\omega_0). \tag{2.11}$$

Only a third of the photons have an electric field oriented in the same direction as the dipole moment hence the factor of three in the denominator of the right-hand side of (2.11). Since the two-level system consists of a single final state, the summation in (2.8) is trivial and for the stimulated emission rate ($R_{stim}$) for the two-level system can now be written as

$$R_{stim} = \frac{\pi\omega_0}{3\epsilon} |x_{12}|^2 \rho(\hbar\omega_0) \tag{2.12}$$

where $\hbar\omega_0 = \hbar\omega_2 - \hbar\omega_1$. Comparing (2.12) and (2.7), $B_{21}$ and $A_{21}$ can now be calculated as

$$B_{21} = \frac{\pi\omega_0}{3\epsilon} |x_{12}|^2 \tag{2.13}$$

$$A_{21} = \frac{\pi\omega_0}{3\epsilon} |x_{12}|^2 \rho_0(\hbar\omega_0) \tag{2.14}$$

For a free-space homogenous medium, the mode density is given by

$$\rho_0 = \frac{8\pi n^3}{h^3 c^3} (\hbar\omega)^2 \tag{2.15}$$

and the spontaneous emission rate into free-space is then given by

$$\frac{1}{\tau} = A_{21} = \frac{\omega_0^3 n}{3\pi\epsilon_0 \hbar c^3} |x_{12}|^2 \tag{2.16}$$

## Estimation of spontaneous emission lifetime ($\tau$) of a hydrogen atom

Using (2.16), an order of magnitude estimate can be given for the spontaneous emission rate of the first excited state in hydrogen to the ground state (the lifetime of the semiconductor will be discussed in more detail later in the dissertation). We can make a reasonable guess that the light-matter interaction will occur on the length scale of Bohr radius ($\approx 0.05$ nm) and we can estimate $|x_{fi}|^2 \approx [(q)(0.05 \times 10^{-9})]^2$. The transition energy of the first excited state to ground state is given by 13.6 eV and therefore the lifetime $\tau$ is estimated as

$$\tau = A_{21}^{-1} = \frac{3\pi\epsilon_0 \hbar c^3}{\left(\frac{q \cdot 13.6}{\hbar}\right)^3} x_{12}^{-2} \tag{2.17}$$

$$\approx 1 \times 10^{-9} \text{ s} \tag{2.18}$$

remarkably consistent with the lifetime calculated in a more rigorous quantum mechanical manner.

## Classical equivalent to the spontaneous emission rate

Classically, spontaneous emission can be modeled as radiation from an atomic oscillating dipole with dipole moment given by $p = qx_0$ and oscillation frequency $\omega_0$ (Figure 2.2a). The

(a)

(dipole)

$\leftrightarrow$

$\rightarrow |\, x_0 \,| \leftarrow$

(b)

Radiated power

$\omega_0$

(c)

$I_0 = q\omega_0$

$R_{rad}$
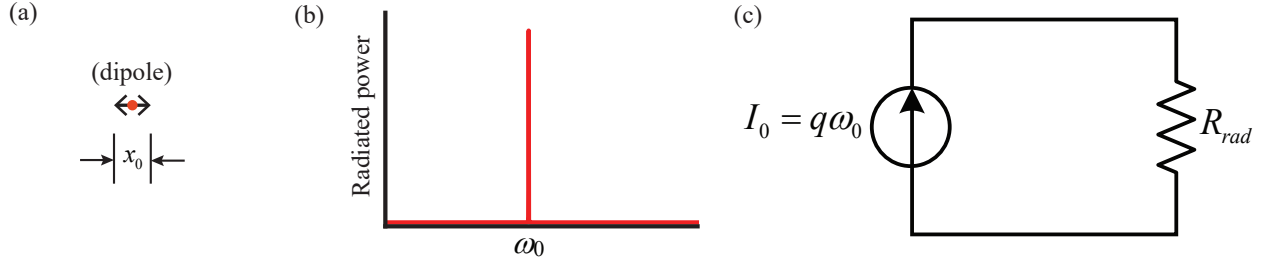
Figure 2.2: (a) Small oscillating dipole emitter with dipole length $x_0$ as a classical model of light emission in an atom or molecule; (b) emission spectrum showing high radiation Q for $x_0 \ll \lambda_0$; and (c) equivalent circuit model for dipole radiation of light.

power radiated ($P_{rad}$) by the classical dipole is given by antenna theory as

$$P_{rad} = \frac{1}{2} I_0^2 R_{rad}$$
$$= \frac{\pi}{3} Z_0 n \left( \frac{x_0}{\lambda_0} \right)^2 (q\omega_0)^2 \tag{2.19}$$

where $R_{rad}$ is the radiation resistance of the infinitesimally small dipole antenna and $I_0 = q\omega_0$ is the dipole current (Figure 2.2c). Written in this form, it is clear that the radiated power (and thus spontaneous emission rate) is small for the atomic oscillating dipole since the dipole length ($x_0 \approx 10^{-10}$ m) is much smaller than the wavelength of light ($\lambda_0 \approx 10^{-6}$ m) and therefore $\left( \frac{x_0}{\lambda_0} \right)^2 \to 0$. Using antenna language we can state that spontaneous emission is an inherently slow process owing to the size mismatch between the length of the atomic optical dipole oscillations responsible for light emission and the wavelength of the emitted light.

The equivalent spontaneous emission rate ($\tau^{-1}$) of the classical atomic oscillating dipole is then

$$\frac{1}{\tau} = \frac{P_{rad}}{\hbar \omega_0} = \frac{2\pi^2 n}{3\hbar \epsilon_0} \frac{(qx_0)^2}{\lambda_0^3} \tag{2.20}$$

which after some rearranging is identical to the rigorous quantum mechanical result in (2.16) provided $qx_0 = 2x_{12}$.

The quality factor (Q) of the small oscillating dipole moment is calculated as

$$Q = \omega_0 \tau = \frac{3\hbar}{\pi Z_0 n} \left( \frac{\lambda_0}{qx_0} \right)^2 \tag{2.21}$$

As expected, $Q \to \infty$ as $\left( \frac{x_0}{\lambda_0} \right)^2 \to 0$ since the radiated power for the small oscillating dipole is weak and the energy remains stored in the oscillating dipole for a long time as qualitatively shown in Figure 2.2b. Returning to the example of the hydrogen atom from the previous

section, the Q-factor exceeds $10^7$ indicating that the atom stores energy for a long time in an excited state before converting the energy into a radiating photon.

## 2.2 Purcell factor and equivalent circuit analysis of spontaneous emission enhancement

In this section, we derive the widely used Purcell factor which is used to calculated the enhancement of spontaneous emission rate for a dipole emitter placed in a cavity. It will be shown that the same physics can be modeled using an equivalent RLC circuit which is useful for predicting the spontaneous emission enhancement in a structure that does not have a well-defined local density of states or mode volume such as an antenna.

### Purcell factor
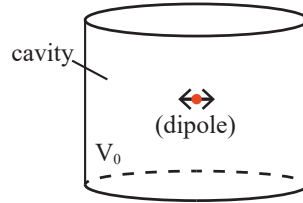


Figure 2.3: Dipole emitter placed in a generic cavity with volume $V_0$.

Imagine a dipole emitter placed inside of a cavity with volume $V_0$ that supports a single resonant mode at angular frequency $\omega_0$ with a quality-factor of $Q$ (Figure 2.3). The mode density ($g(\hbar\omega)$) in the cavity can be modeled by a Lorentzian function that satisfies the normalization condition $\int_0^\infty V_0 g(\hbar\omega)d(\hbar\omega) = 1$. Such a function is given by

$$g(\hbar\omega) = \frac{2Q}{\pi\hbar\omega_0 V_0}\frac{\Delta\omega_0^2}{4(\omega-\omega_0)^2 + \Delta\omega_0^2} \qquad (2.22)$$

with peak mode density of $g(\hbar\omega_0) = \frac{2Q}{\pi\hbar\omega_0 V_0}$. The mode density $g(\hbar\omega)$ is commonly refered to as the local density of states (LDOS). Plugging this density of states into (2.14) and taking into account that only $\frac{1}{3}$ of the dipoles will interact with the cavity mode, it is straightforward to derive spontaneous emission rate in the cavity as

$$\frac{1}{\tau_{cav}} = \frac{2Q}{3\epsilon V_0}\left|x_{12}\right|^2 \qquad (2.23)$$

The Purcell factor ($F_P$) can be derived by dividing (2.23) by the rate of spontaneous emission in a homogenous medium such that

$$F_P = \frac{\frac{2Q}{3\epsilon V_0}|x_{12}|^2}{\frac{\omega_0^3 n}{3\pi\epsilon\hbar c^3}|x_{12}|^2}$$
$$= \frac{3Q(\lambda_0/n)^3}{4\pi^2 V_0} \tag{2.24}$$

Therefore a large increase in the spontaneous emission rate requires a cavity that has a high quality factor and low volume to maximize the $Q/V_0$ ratio.

If we define a normalized mode volume such that $V_m = V_0/(\lambda_0/2n)^3$ then

$$F_P = \frac{6}{\pi^2}\frac{Q}{V_m}. \tag{2.25}$$

**Limitations of the Purcell factor**

Some care needs to be taken in blindly applying the Purcell factor (2.27) to determine the spontaneous emission rate enhancement in a structure. The normalized mode volume ($V_m$) is not always straightforward to define in a cavity with a mode that has spatial variance. Normalized mode volume is particularly nebulous to define in a low-Q structure such as an optical antenna in which the mode is radiating into free space [62], [63]. The Purcell factor should be abandoned completely if an accurate spontaneous emission rate enhancement is desired for a low-Q antenna structure or a non-resonant structure. In this case, circuit analysis can be used to derive the spontaneous emission enhancement factor.

**Equivalent circuit analysis**
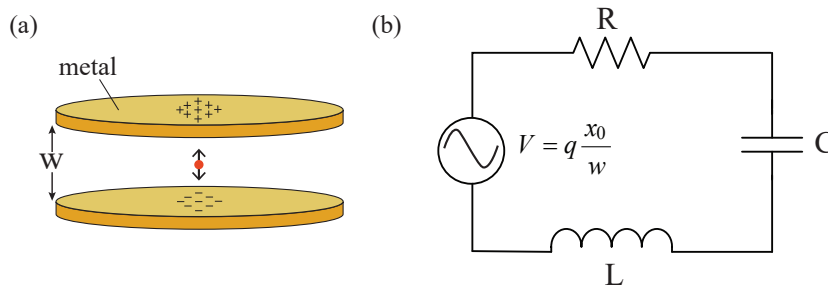


Figure 2.4: Derivation of Purcell factor using circuit model; (a) simple cavity consisting of dipole emitter placed between two parallel metal plates; (b) equivalent circuit model of cavity in (a).

Following [64], consider an dipole placed in the gap of a parallel plate capacitor with plate spacing $w$ much smaller than the lateral extent of the plates (Figure 2.4a). According to the Ramo-Shockley Theorem [65], [66], the dipole will induce a charge and therefore voltage on the capacitor plates given by $V = q\frac{x_0}{w}\frac{1}{C}$ where $x_0$ is the dipole moment length and $w \ll \lambda_0$ is the plate separation. A time-varying voltage on the capacitor plates will support a time-varying magnetic field and thus the capacitor at high frequency is capable of storing both electric and magnetic energy. Therefore, the capacitor can be equivalently represented as an RLC circuit with resonance frequency given by $\omega_0 = (LC)^{-\frac{1}{2}}$ as shown in Figure 2.4b. The quality factor $(Q)$ of the RLC circuit is given by $Q = (R\omega_0 C)^{-1}$ where the resistance $(R)$ consists of both metal and radiation loss. The power delivered to the cavity is then

$$P = \frac{1}{2}\frac{V^2}{R} = \frac{1}{2R}\left(\frac{q\frac{x_0}{w}}{C}\right)^2 = \frac{(qx_0)^2\omega_0}{2\epsilon_0}\left(\frac{Q}{V_0}\right) \tag{2.26}$$

The ratio of the power delivered by the dipole to the cavity to that of free space is given by dividing (2.26) by (2.19)

$$\frac{P}{P_0} = \frac{(qx_0)^2\omega_0}{2\epsilon_0}\left(\frac{Q}{V_0}\right) \bigg/ \frac{\pi}{3}Z_0 n\left(\frac{x_0}{\lambda_0}\right)^2 (q\omega_0)^2$$
$$= \frac{6}{\pi^2}\left(\frac{Q}{V_m}\right) \tag{2.27}$$

which remarkably recovers the Purcell factor derived in the previous section.

Deriving the spontaneous emission rate enhancement using circuit analysis gives additional physical insight into how to engineer a structure to achieve maximum spontaneous emission enhancement. The inductance $(L)$, resistance $(R)$, and capacitance $(C)$ can be derived in terms of physical parameters of the structure and rationally chosen to achieve maximum spontaneous emission enhancement. Beyond the simple cavity and RLC circuit shown here, circuit analysis can be used to analyze more sophisticated structures and include additional parasitic resistance or reactive elements to further increase the accuracy of the model .

## 2.3 Spontaneous emission rate enhancement with an optical antenna

Consider the small oscillating dipole moment with angular frequency $\omega_0$ that is placed in the feedgap of the dipole antenna as shown in Figure 2.5a. Similar to what was done for the generic cavity in the previous section, the dipole antenna in Figure 2.5a can be modeled as an equivalent circuit as shown in Figure 2.5b. For now, we will only be concerned about the radiated power at resonance and therefore the inductance and capacitance can be ignored since the reactance of the antenna goes to zero on resonance. Ignoring loss in the metal,

(a)



(b)
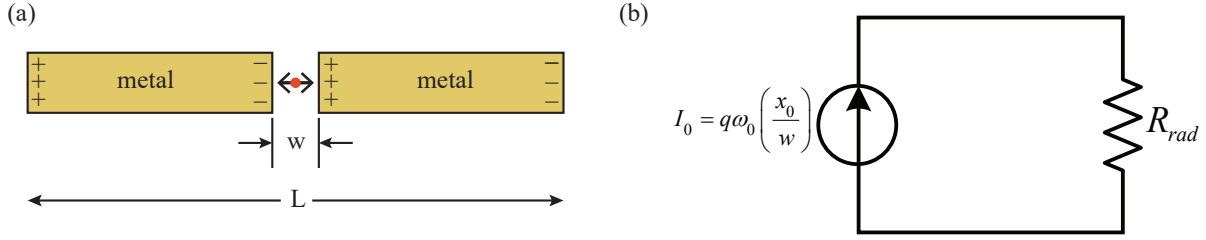
Figure 2.5: (a) Dipole emitter coupled to an external dipole antenna; and (b) equivalent circuit model for (a).

the equivalent circuit on resonance consists of a current source driving a radiation resistance where the current is the induced current from the dipole placed in the antenna feedgap. The induced current in the two metal arms is given by Ramo-Shockley Thereom as $I_0 = q\omega_0 x_0/w$. An approximate expression for radiation resistance $R_{rad}$ of the dipole antenna is well known from the electromagnetic textbooks [67] and is given by $R_{rad} = \frac{\pi}{6} Z_0 \left(\frac{L}{\lambda_0}\right)^2 (q\omega_0)^2$. The power radiated by the dipole moment coupled to the dipole antenna is then given by

$$P_{rad} = \frac{1}{2} I_0^2 R_{rad} \tag{2.28}$$

$$= \frac{\pi}{12} Z_0 n \left(\frac{L}{\lambda_0}\right)^2 \left(\frac{x_0}{w}\right)^2 (q\omega_0)^2. \tag{2.29}$$

The spontaneous emission enhancement is calculated by dividing (2.28) by the power radiated by the bare dipole (2.19) which gives

$$\frac{P_{rad}}{P_0} = \frac{\frac{\pi}{12} Z_0 n \left(\frac{L}{\lambda_0}\right)^2 \left(\frac{x_0}{w}\right)^2 (q\omega_0)^2}{\frac{\pi}{3} Z_0 n \left(\frac{x_0}{\lambda_0}\right)^2 (q\omega_0)^2}$$

$$= \frac{1}{4} \left(\frac{L}{w}\right)^2 \tag{2.30}$$

Therefore, a small antenna feedgap and large antenna length is desired to maximize spontaneous emission enhancement. In practice, the antenna size is often not an independent parameter but is set by the desired antenna resonance wavelength. For a dipole antenna with $L = \lambda_0/2 = 1.0$ $\mu$m and $w = 10$ nm, (2.30) predicts a remarkable 2500-fold increase in the spontaneous emission rate of a dipole emitter!

## Antenna vs. cavity for spontaneous emission enhancement

It was shown that both a cavity and an antenna can provide spontaneous emission enhancement. Therefore it is conceivable that either an antenna or cavity can be used to make a fast

LED device for optical communication. However, the antenna-LED has several advantages over the cavity-LED:

- **Broad enhancement spectrum**. An antenna is designed to radiate power quickly. The opposite is true for a cavity: a cavity is designed to store energy. In other words, the radiation quality-factor or $Q_{rad}$ of an antenna is smaller than a cavity. This is particularly relevant if we wish to enhance spontaneous emission of a material with a broad emission spectrum such as a semiconductor. The broadband antenna will enhance the semiconductor spontaneous emission spectrum more efficiently than a narrow-band cavity.

- **Nanoscale *and* efficient**. Antenna efficiency can be very high (approaching unity) because of the low $Q_{rad}$ (typically $< 50$) despite the relative lossy metal at optical frequencies. An equivalently sized metal-optic cavity is less efficient because of the high $Q_{rad}$ (typically $> 100$). The cavity radiation efficiency can be increased by using an all-dielectric cavity; however, at the expense of larger size.

## 2.4 Spontaneous emission rate enhancement of a semiconductor with an optical antenna
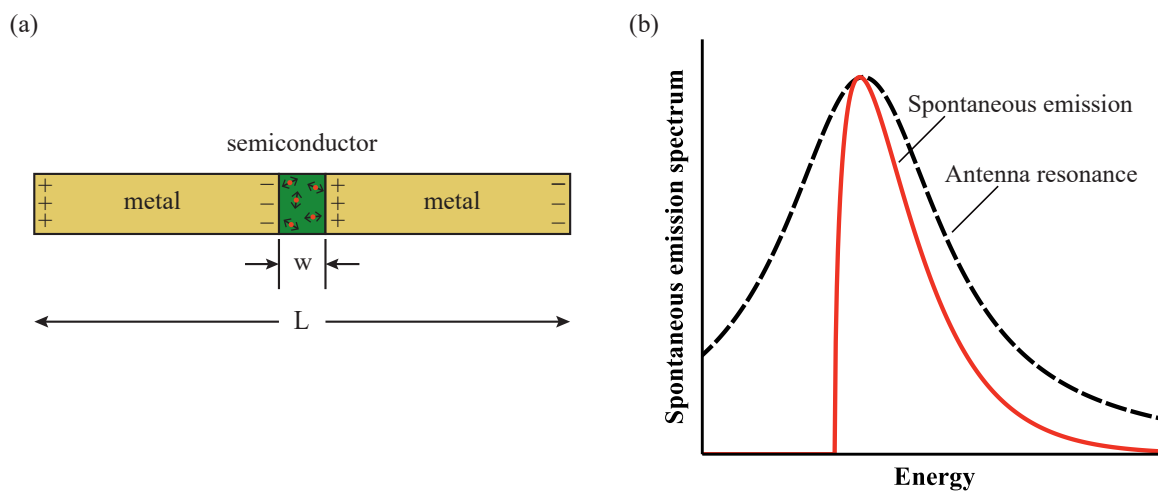


Figure 2.6: (a) Semiconductor coupled to a dipole antenna; and (b) desired antenna enhancement spectrum as compared with the broad emission spectrum of the semiconductor.

Light emission in a semiconductor can be modeled as an ensemble of randomly oriented oscillating dipoles embedded in a dielectric matrix (Figure 2.6a). Each dipole oscillates with a slightly different angular frequency and thus produce a broad emission spectrum. The

spontaneous emission rate can be enhanced by coupling the semiconductor to the feedgap of a suitably designed external antenna as shown in Figure 2.6. However, the random dipole orientation, broad emission spectrum, and high dielectric permittivity lead to several design challenges. A few of these design challenges related to the antenna-enhancement of a semiconductor will be highlighted now as they are central themes throughout the dissertation.

## Overlap between antenna resonance and broad spontaneous emission spectrum

The spontaneous emission spectrum of a semiconductor is broad (a few kT in width) and therefore we desire a broad antenna resonance to adequately enhance the spontaneous emission rate of all dipole emitters (Figure 2.6b).

## The effect of semiconductor with large refractive index ($n$) in the antenna feedgap

Placing a semiconductor with large refractive index in the antenna feedgap will reduce the spontaneous emission enhancement by a factor equal to relative permittivity $\epsilon_R$. For most semiconductors, $\epsilon_R \approx 12$ therefore there is about an order of magnitude reduction in spontaneous emission enhancement. For the dipole antenna, this can be seen by analyzing (2.30). For a given antenna resonance frequency, if a semiconductor is inserted into the antenna feedgap, the dipole length needs to be reduced by approximately a factor $n$ to maintain the same resonance frequency. Therefore, by (2.30), the spontaneous emission enhancement necessarily reduces by $n^2 = \epsilon_R$.

## Dipole averaging

The typical "bulk" semiconductor has isotropic emission and therefore the orientation of dipole emitters is random (see Figure 2.6a). Most antennas of interest have some polarization. Only those dipoles with orientation aligned with the antenna polarization will observe enhanced spontaneous emission. For a linear antenna such as the dipole or slot antenna (to be discussed later), only a third of the dipoles on average will couple to the antenna thus limiting the overall spontaneous emission enhancement. This effect of dipole averaging can be mitigated by choosing a material with some intrinsic polarization that aligns with the antenna mode such as a quantum well or other 2D semiconductor.

# Chapter 3

# Antenna design for the electrically-injected antenna-LED

In the previous chapter, it was shown that the spontaneous emission rate is slow because the size of the typical dipole emitter is small with respect to its emission wavelength. By coupling a dipole emitter to an antenna, the spontaneous emission rate can be increased dramatically, even exceeding the stimulated emission rate.

At the end of last chapter, several general design principles on enhancing the spontaneous emission rate of a semiconductor were discussed. In this chapter, we wish to further explore these concepts to design an appropriate antenna for the electrically-injected antenna-coupled LED (antenna-LED).

## 3.1    Electrically-injected dipole antenna-LED

The basic dipole antenna has been well studied at optical frequencies and therefore serves as a logical starting point to design an electrically-injected antenna-LED [40], [68]–[72]. Perhaps the primary advantage of the dipole antenna is the ease of fabrication. The dipole antenna is typically fabricated in a straightforward manner using a standard lift-off procedure with e-beam lithography to deposit the dipole metal arms (typically Ag or Au).

It was shown that it is possible to use the antenna arms as electrical leads if contact is made to the arms at a region where the fields are small [56], [73]. This idea inspired the electrically-injected antenna-LED shown in Figure 3.1 which consists of a III–V pn junction ridge coupled to an arch-dipole antenna. The arch-dipole is similar to the standard dipole antenna except with inclusion of a metal arch over the feedgap [40]. The arch can be thought of as a matching LC network which can be used to increase the length of the dipole arms without shifting the resonance frequency and therefore from (2.30) provide increased spontaneous emission enhancement. The primary advantage here however is the self-alignment of the III–V ridge to the antenna without the need for careful lithographical alignment.
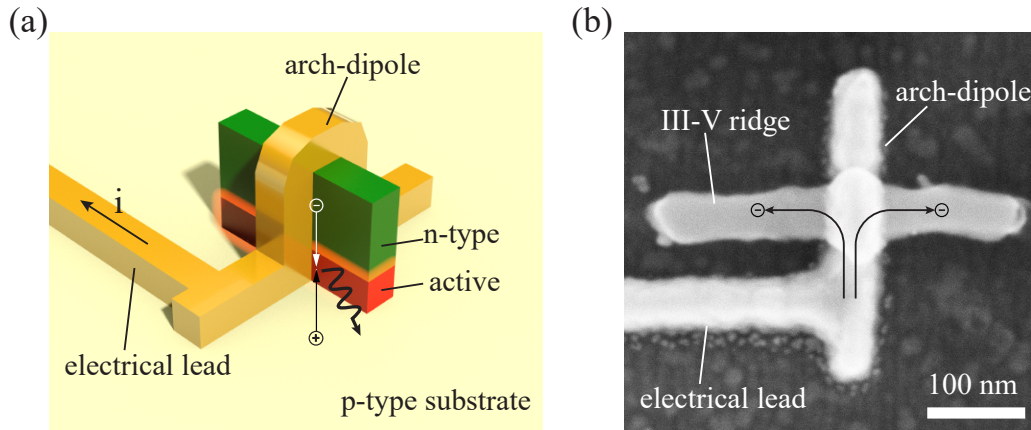
Figure 3.1: (a) Drawing of electrically-injected arch-dipole antenna-LED; and (b) top-down SEM image of fabricated antenna-LED

The fabrication of the arch-dipole antenna-LED was straightforward; a III–V pn junction ridge was first etched using a top-down approach with wet etching (although dry etching can be used as well). Next, the arch-dipole antenna was deposited on top of the ridge. Electrons were injected into the active region through one of the dipole arms whereas holes were injected through the p-type substrate.

## Issues with the electrically-injected dipole antenna-LED

Several problems were identified that make this approach non-ideal for the antenna-LED. As illustrated in Figure 3.1b, electrons can easily bypass the antenna feedgap and recombine with holes outside the antenna hotspot effectively reducing the overall spontaneous emission enhancement of the device. The ridge length can be scaled down such that it precisely fits within the feedgap; however, careful registration is needed between the ridge and antenna. Second, the contact area of the arch-dipole to the III–V is small ($\approx 10^{-11}$ cm$^2$) and results in a large series contact resistance.

Based on these considerations, the dipole antenna is not the best approach for an electrically-injected antenna-LED. Therefore we seek more suitable antenna structures.

## 3.2 Slot antenna

The slot antenna is closely related to the dipole antenna and in its most basic form consists of a ground plane with a rectangular cut-out. The slot and dipole antennas are considered complementary structures as shown in Figure 3.2. By swapping free-space with metal, and metal with free-space, the complementary slot antenna can be constructed from the dipole antenna and vice-versa. Given the geometric duality of the two antennas it is not surprising

(a)                                                              (b)
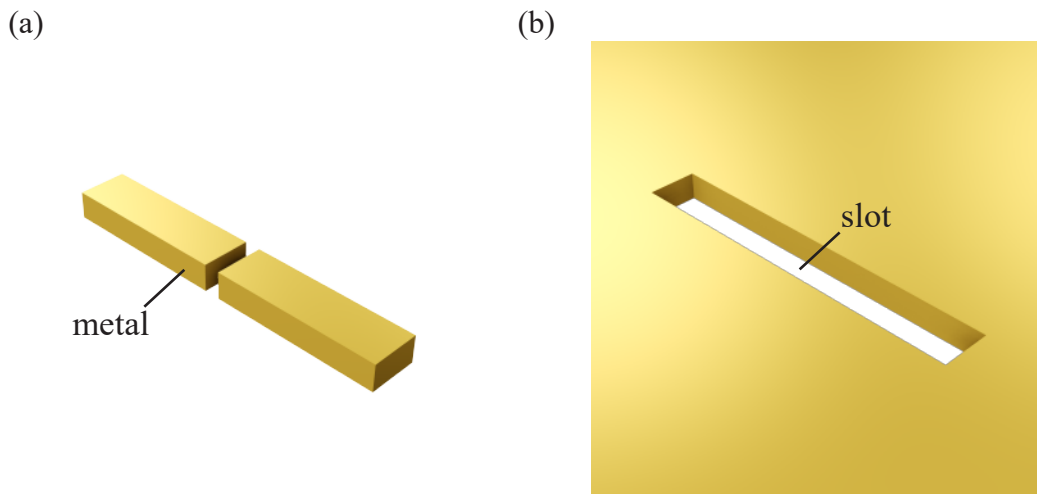


Figure 3.2: Drawing of (a) dipole antenna; and (b) complementary slot antenna

to find the same duality in the electromagnetic properties of the two antennas. Indeed, as
will be shown, the far-field radiation of the two antennas are identical if the electric and
magnetic fields are swapped.

## Radiation properties of the slot antenna

Consider a slot antenna with length $L$ and width $w$ with slot filled with dielectric of refractive
index $n = \sqrt{\epsilon}$ (Figure 3.3a). A dipole emitter with angular frequency $\omega_0$ placed at the center
of the slot will excite an antenna mode if the length of the slot is $L \approx \lambda_0/2$. Current will be
induced to flow in a loop around both ends of the slot as shown in Figure 3.3b. A closed-
form expression for the current distribution is not possible since the current is not physically
bounded and forced to flow in a linear fashion as is the case for the dipole antenna. Instead,
it is useful to look at the electric-field distribution within the slot. The slot can be thought
of as a slotline transmission line that is shorted at either end. The voltage at the shorted
load of the transmission line necessarily goes to zero and therefore the voltage will also go
to zero at either end of the slot[1]. On resonance, a standing voltage wave will exist within
the slot as illustrated in Figure 3.3c. The voltage as a function of position along the slot is
then given by

$$V(z) = V_0 \cos\left(\frac{\pi}{L}z\right) \tag{3.1}$$

The voltage in the slot antenna has the same form as the current in the dipole antenna thus
hinting that the radiation of the slot antenna will behave in a complementary manner to the
dipole antenna.

---

[1]Equivalently stated: the tangential electric field at the end of the slot must go to zero according to the
boundary conditions to Maxwell's equations
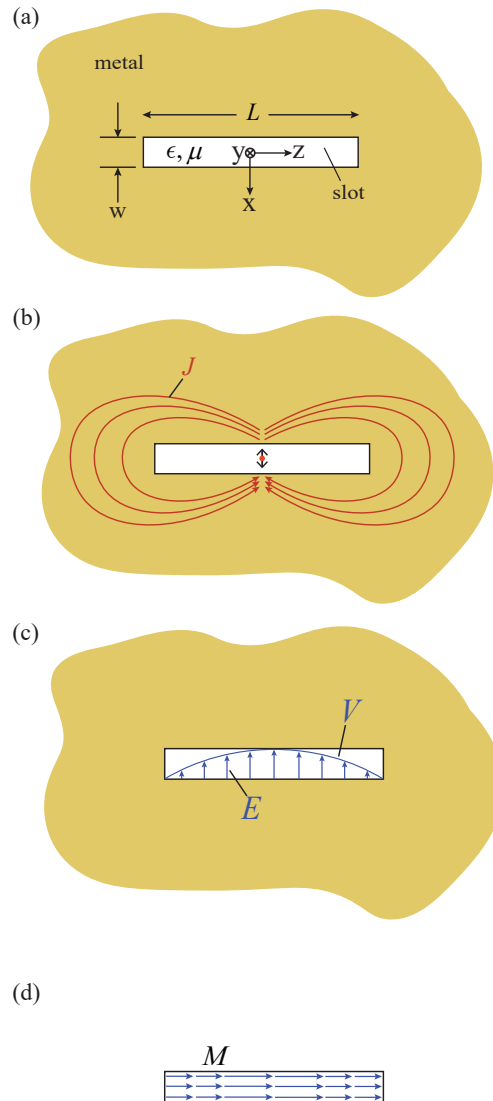
Figure 3.3: (a) Top-view diagram of the slot antenna; (b) illustration of the current density and (c) voltage standing wave when the slot is excited by a dipole emitter; and (d) equivalent magnetic source representation of the slot antenna

The electric-field within the slot is transverse to the long-axis of the slot and tangential to the xz-plane. The tangential electric-field at the xz-plane outside of the slot is zero because of the metal ground plane (assuming the metal is a very good conductor). With complete knowledge of the tangential electrical field at the boundary between the upper and lower half space at the xz-plane, it is possible to reformulate the problem using the surface equivalence principle and model the slot as a magnetic current source radiating into free space (Figure

3.3d). The magnetic current source is given by

$$\mathbf{M}(z) = 2\mathbf{E} \times \hat{n} = \pm 2\frac{V_m}{w}\cos\left(\frac{\pi}{L}z\right) \tag{3.2}$$

where $\mathbf{E}$ is the tangential electric-field in the slot [74]. The slot antenna produces semi-circular electric-field lines that point in one direction in the upper half-space and the opposite direction in the lower half-space (the electric field terminates at the positive charge built up on one side of the slot and the negative charge built up on the other side). Therefore, the direction of the equivalent magnetic current source is dependent upon which half-space is being analyzed (hence the $\pm$ in (3.2)). This subtle point is not often mentioned in the electromagnetic textbooks.

Equation (3.2) has identical form to the electric current in the dipole antenna, except, for the slot there is a radiating magnetic current. Therefore, the fields radiated by the slot antenna can be obtained from the far-field of the dipole antenna after swapping the electric and magnetic field and rotating the polarization by 90°.

Despite the similarity with the dipole antenna, there have only been a handful of reports using the slot antenna to enhance spontaneous emission [42], [75]–[78]. This may be because of the difficulty in fabricating a nanoscale cut-out in a metal sheet. It is much easier to deposit metals then remove metals at the nanoscale. Later in this chapter, the cavity-backed slot antenna will be introduced which solves the fabrication difficulties associated with the slot antenna.

## Far-field radiation resistance of the slot antenna

Booker showed that the impedance of the dipole and slot antennas (and indeed any complementary antenna) can be related by the expression [79]

$$Z^{slot}Z^{dipole} = \frac{\eta^2}{4} \tag{3.3}$$

On resonance, the impedance of the antenna is simply equal to the radiation resistance (neglecting loss for the moment) and therefore the radiation resistance of the slot antenna can simply be calculated from the radiation resistance of the dipole antenna as

$$R_{rad}^{slot} = \frac{Z_0^2}{4R_{rad}^{dipole}}. \tag{3.4}$$

For this reason, for the slot antenna, we will employ parallel resonant circuits in this chapter, with reciprocal radiation resistance, as opposed to the normal radiation resistance in Chapter 2. The radiation resistance of the dipole antenna with sinusoidal current distribution and length $L \approx \lambda_0/2$ is well-known and can be solved numerically as $R_{rad}^{dipole} \approx 73\Omega$. However, at optical frequencies, the antenna length may be significantly shorter than $\lambda_0/2$ and we seek a closed-form expression for $R_{rad}^{dipole}$ for arbitrary $L$. Unfortunately, this is not possible;

an approximation is used instead. Following [80], the dipole current is modeled as being constant such that $I(z) = I_0$. An effective dipole length ($L_{eff}$) is then introduced which is a weighted average of the true dipole current distribution over the length of the antenna such that

$$L_{eff} = \frac{\int\limits_{-L/2}^{L/2} I(z)dz}{I_0}. \tag{3.5}$$

For a sinusoidal current distribution, $L_{eff} = 0.64L$. The radiation resistance is now calculated assuming a dipole length of $L_{eff}$ with constant current $I_0$ and is given by

$$R_{rad,dipole} = \frac{2\pi}{3} Z_0 n \left(\frac{L_{eff}}{\lambda_0}\right)^2. \tag{3.6}$$

The equivalent expression for the radiation resistance of the slot antenna can be quickly found using Booker's expression (3.3) as

$$R_{rad,slot} = \frac{3}{8\pi} \frac{Z_0}{n^3} \left(\frac{\lambda_0}{L_{eff}}\right)^2. \tag{3.7}$$

In this case, $L_{eff}$ is the weighted average of the voltage over the length of the slot.

## Equivalent circuit model for the slot antenna

The slot antenna can be modeled as two $\lambda/4$ shorted stubs of slotline transmission line (Figure 3.4a) [81]. It is well known that a shorted $\lambda/4$ stub has $\infty$ impedance at resonance and will behave like an equivalent parallel RLC circuit therefore we can apply the same equivalent circuit to the slot antenna.

Shown in Figure 3.4b is the simplified equivalent parallel RLC circuit for the slot antenna driven by a dipole emitter with an oscillation frequency of $\omega_0$ where the antenna resistance has been split up into a Ohmic loss resistance ($R_\Omega$) and radiation loss resistance ($R_{rad}$). The inductance comes from the traditional Faraday inductance plus the kinetic inductance. The kinetic inductance is a result of the "plasmonic" effect and will be discussed at the end of the chapter. The capacitance is mostly from the parallel plate capacitance across the narrow slot plus any fringing contribution. Without worrying for a moment about the values of the circuit elements we can derive an expression for the spontaneous emission enhancement[2].

According to the Shockley-Ramo Theorem (see Appendix A), the dipole emitter will induce a current $I_0 = (q\omega_0 x/w)$ into the antenna. On resonance, the impedance of the inductance (L) and capacitance (C) will precisely cancel each other out and we are left with the simplified equivalent circuit in Figure 3.4c.

---

[2]Here we have ignored second order effects such as spreading resistance and the anomalous skin effect. The former will tend to reduce the antenna efficiency and the latter will become important when the slot width is $< 10$ nm [40]

(a)



(b)



(c)
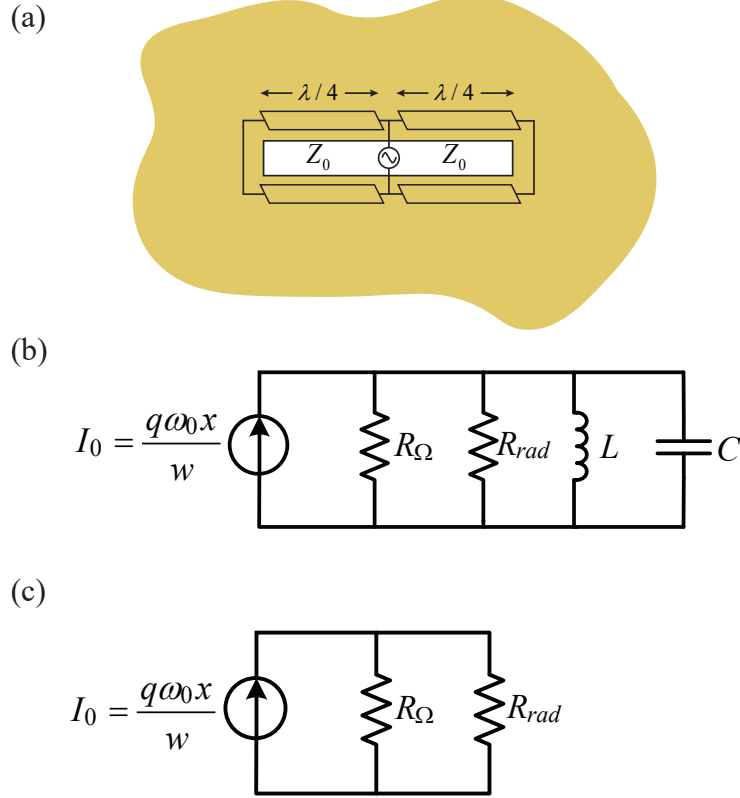


Figure 3.4: (a) Slot antenna modeled as two shorted $\lambda/4$ stubs of slotline transmission line; (b) equivalent RLC circuit for the slot antenna; and (c) equivalent circuit for the slot antenna on-resonance. These are parallel resonant circuits unlike the series resonant circuits in Chapter 2.

## Spontaneous emission enhancement factor of the slot antenna

The power radiated ($P_{rad}$) by the slot antenna is derived as

$$
\begin{aligned}
P_{rad} &= \frac{1}{2}I_0^2 R_{rad} \\
&= \frac{1}{2}\left(\frac{R_\Omega}{R_\Omega + R_{rad}}\right)^2 \left(\frac{q\omega_0 x}{w}\right)^2 R_{rad} \\
&= \frac{1}{2}\eta_{ant}^2 \left(\frac{q\omega_0 x}{w}\right)^2 R_{rad}
\end{aligned}
\tag{3.8}
$$

where $\eta_{ant} = R_\Omega/(R_\Omega + R_{rad})$ is the antenna efficiency.

Using the radiation resistance of the slot antenna from (3.7), the spontaneous emission

enhancement is given by

$$F = \frac{P_{rad}}{P_0} = \frac{\frac{1}{2}\eta_{ant}^2 \left(\frac{q\omega_0 x}{w}\right)^2 \frac{3}{8\pi} \frac{Z_0}{n^3} \left(\frac{\lambda_0}{L_{eff}}\right)^2}{\frac{1}{2}(q\omega_0)^2 \frac{2\pi}{3} Z_0 n \left(\frac{x_0}{\lambda_0}\right)^2}$$

$$= \frac{9}{16\pi^2} \eta_{ant}^2 \frac{1}{n^4} \frac{\lambda_0^4}{w^2 L_{eff}^2} \tag{3.9}$$

Assuming high antenna efficiency ($\eta_{ant} \approx 1$) and $L \approx \lambda_0/2n$ on resonance, we can simplify (3.9) as

$$F = \frac{9}{\pi^2} \left(\frac{L_{eff}}{w}\right)^2 \tag{3.10}$$

which is identical in form to the radiation resistance derived for the dipole antenna given in (2.30).

## Limitations of the slot antenna

It does not seem as though much is gained by using the slot antenna for an electrically-injected device. We now have the problem of needing to precisely fill the slot with a semiconductor and make electrical contact without perturbing the antenna mode. It is not obvious how this can be achieved. Furthermore, the slot antenna radiates on both of sides of the slot. This is less than ideal for an optical communication device where it is generally desired to send light in one direction only. Next, it will be shown that all of those problems can be solved by "backing" the slot with a cavity.

# 3.3 Cavity-backed slot antenna

If one side of the slot is backed with an appropriately sized cavity (Figure 3.5), the radiation will be restricted to propagate into only one of the half spaces. Such an antenna is called a cavity-backed slot antenna.

## Resonance frequency of the cavity-backed slot antenna

The behavior of the cavity-backed slot antenna is well-described by modeling the cavity as a metallic rectangular waveguide that is opened to free space at one end and shorted at the other end where the waveguide cross-sectional dimensions are given by the slot width ($w$) and length ($L$) [82].
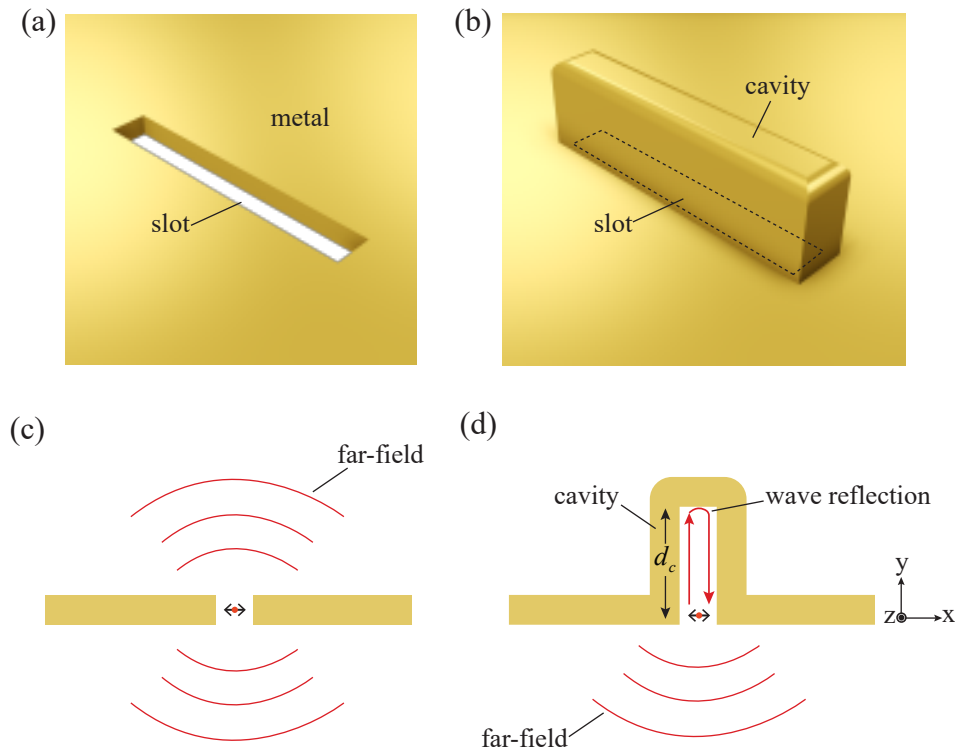
Figure 3.5: Comparison of the slot antenna and cavity-backed slot antenna. (a) Drawing of the slot antenna; and (b) slot antenna backed with a cavity; (c) illustration showing far-field radiation on both sides of the slot antenna; and (d) far-field radiation only on one side of the cavity-backed slot antenna

Consider a small dipole emitter driving the cavity-backed slot antenna at the center of the slot[3]. This source will excite a waveguide mode that propagates into the cavity in the $+y$-direction while also radiating into free space in the $-y$-direction. The wave that propagates in the $+y$-direction will eventually reach the shorted end of the cavity and undergo a reflection and phase shift of $\pi$ radians. If the depth of the cavity is designed such that the reflected wave returns to the source with an overall phase shift consisting of a multiple of $2\pi$ radians then the reflected wave will add up constructively with the radiation that is emitted from the dipole in the $-y$-direction. In this manner, the radiation that would normally emit into the upper half space ($y > 0$) is now re-directed into the lower half-space ($y < 0$) (Figure 3.5c-d).

If the cavity depth is given by $d_c$ and the wave constant of the guided mode in the cavity

---

[3]The distinction between the slot and the cavity is somewhat ambiguous in the cavity-backed slot antenna. Here, the slot is the opening of the cavity at the plane $y = 0$ whereas the cavity is the region $y > 0$.

is given by $k_y$, the resonance condition of the cavity-backed slot antenna can be written as

$$\Delta\phi = 2k_yd_c + \pi = 2\pi \tag{3.11}$$

$$k_yd_c = \frac{\pi}{2}. \tag{3.12}$$

The propagation constant $(k_y)$ for the fundamental TE mode of a rectangular waveguide is given by

$$k_y = \sqrt{\omega^2\mu\epsilon - \left(\frac{\pi}{L}\right)^2}. \tag{3.13}$$

The resonance frequency is determined by inserting (3.13) into (3.12) and solving for $\omega_0$; doing so gives

$$\omega_0 = \frac{\pi c}{n}\sqrt{(2d_c)^{-2} + L^{-2}}. \tag{3.14}$$

As will be shown later, (3.14) predicts the resonance behavior of the cavity-backed slot antenna remarkably well despite this simple model. Shown in Figure 3.6 is a contour plot of the resonance frequency as a function of slot length $(L)$ and cavity depth $(d_c)$ for a cavity filled with a semiconductor (n=3.4) and radiating into the same medium.
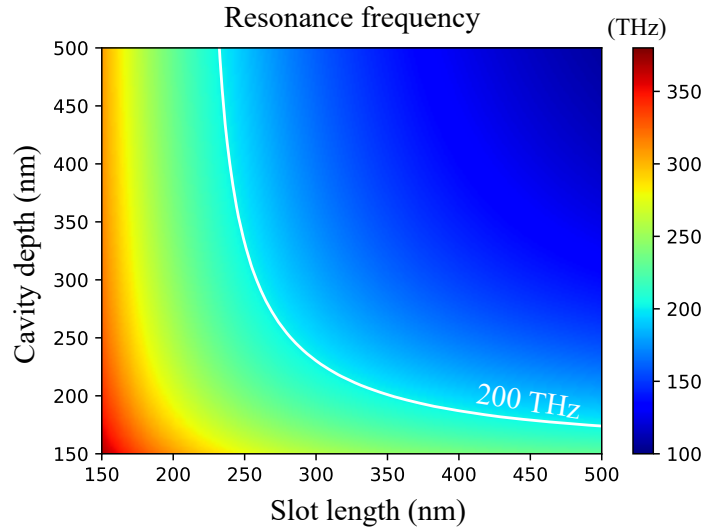


Figure 3.6: Contour plot of the resonance frequency of the cavity-backed slot as a function of slot length $(d_c)$ and cavity depth $(d_c)$. Cavity is filled with semiconductor medium $(n = 3.4)$ and is radiating into the same medium. Perfect metals are assumed. The solid white contour line denotes the combinations of slot length and cavity depth that achieve antenna resonance at 200 THz

Many different combinations of $d_c$ and $L$ result in the same resonance frequency $(\omega_0)$. This gives additional flexibility to the antenna designer. As will be shown later, the choices for $d_c$ and $L$ are not completely arbitrary. The optimal values for the antenna-LED are chosen to maximize the radiated power and therefore spontaneous emission enhancement.

## Radiation resistance of the cavity-backed slot antenna
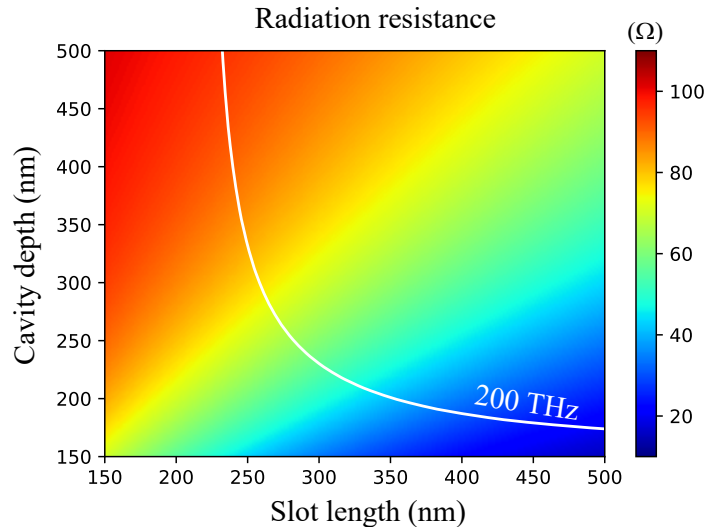


Figure 3.7: Contour plot of the radiation resistance ($R_{rad}$) of the cavity-backed slot as a function of slot length ($d_c$) and cavity depth ($d_c$). Same conditions as in Figure 3.6. The solid white contour line denotes the combinations of slot length and cavity depth that achieve antenna resonance at 200 THz

Since the cavity-backed slot antenna re-redirects all the radiation into the lower half-space ($y < 0$), the magnitude of the electric field is doubled with respect to the slot antenna without a cavity. Doubling of the electric field yields a power density that is four times as high. However, the cavity-backed slot antenna radiates into half as much volume as the slot antenna and therefore the overall radiated power is increased only by a factor of two. Therefore, the radiation resistance of the cavity-backed slot antenna is simply twice that of the slot antenna given by (3.7) or

$$R_{rad} = \frac{3}{4\pi} \frac{Z_0}{n^3} \left( \frac{\lambda_0}{L_{eff}} \right)^2 \tag{3.15}$$

Plotted in Figure 3.7 is a contour plot for the radiation resistance as a function of slot length and cavity depth. Again it is assumed that the cavity is filled with a dielectric medium (n=3.4) and radiating into the same dielectric medium and all metals are perfect electrical conductors. Overlayed on the same plot is a contour denoting where the antenna is resonant at 200 THz. Thus, the radiation resistance of the cavity-backed slot antenna can be tuned to the desired value while maintaining the same resonance frequency.

## Spontaneous emission enhancement factor of the cavity-backed slot antenna

Similar to the slot antenna, the cavity-backed slot antenna is also modeled as a short-circuit $\lambda/4$ transmission line stub and thus also has the equivalent RLC circuit shown in Figure 3.4. The power radiated ($P_{rad}$) by the cavity-backed slot antenna is derived in the same manner as the slot antenna as

$$
\begin{aligned}
P_{rad} &= \frac{1}{2} I_0^2 R_{rad} \\
&= \frac{1}{2} \left( \frac{R_\Omega}{R_\Omega + R_{rad}} \right)^2 \left( \frac{q\omega_0 x}{w} \right)^2 R_{rad} \\
&= \frac{1}{2} \eta_{ant}^2 \left( \frac{q\omega_0 x}{w} \right)^2 R_{rad}.
\end{aligned} \tag{3.16}
$$

Since the radiation resistance of the cavity-backed slot antenna is twice that of the slot antenna, the spontaneous emission enhancement is simply twice (3.9) or

$$
F = \frac{9}{8\pi^2} \eta_{ant}^2 \frac{1}{n^4} \frac{\lambda_0^4}{w^2 L_{eff}^2} \tag{3.17}
$$

An advantage of the cavity-backed slot antenna is now evident: we have the flexibility to choose the slot length that maximizes the spontaneous emission enhancement factor while maintaining the desired resonance frequency. Equation (3.17) implies that the slot length should be scaled as small as possible to increase the radiation resistance and achieve the highest spontaneous emission enhancement. This should be carefully balanced with the antenna efficiency as the loss also increases as the slot length is reduced.

### Comparison with the conventional slot antenna

To compare the performance of the cavity-backed slot antena with the conventional slot antenna we choose $L = \lambda_0/2n$ and assume $\eta_{ant} \approx 1$ such that (3.17) is simplified as

$$
F = \frac{18}{\pi^2} \left( \frac{L_{eff}}{w} \right)^2 \quad \text{for } L = \lambda_0/2n \text{ and } \eta_{ant} = 1 \tag{3.18}
$$

The spontaneous emission enhancement factor is then twice that of the conventional slot antenna as a consequence of higher radiation resistance of the cavity-backed slot antenna.

## The "plasmonic" effect

Before continuing it is worth discussing the behavior of metals at optical frequencies and how it affects the characteristics of the cavity-backed slot antenna and optical antennas in general. At low frequencies (e.g. microwave frequencies) metals behave as near-perfect

mirrors. Electrons in metals respond in lock-step with an impinging electromagnetic wave, oscillating at the same frequency, and thus re-radiating and reflecting the impinging wave

At optical frequencies, the electric-field is oscillating so rapidly that electrons have difficulty responding and will lag behind an applied electric field. It is shown in Appendix B that this lag in the response of electrons at optical frequencies can be modeled as an equivalent inductance with value given by

$$L_K = \frac{\text{Im}\,\rho}{\omega} \frac{\text{length}}{\text{area}} \tag{3.19}$$

where $\rho$ is the complex resistivity of the metal at optical frequencies. $L_K$ is referred to as the "kinetic inductance" since the energy of the inductance is not stored not in the magnetic field, but rather in the kinetic energy of the electrons.

In a "plasmonic" device, the kinetic inductance is larger than the conventional Faraday inductance ($L_F$). In other words, more energy is stored in the kinetic energy of electrons than in the magnetic field. Plasmonics enables sub-wavelength optical structures because the optical mode sloshes back and forth between electrical energy and the kinetic energy of electrons, thus bypassing the magnetic field and breaking the diffraction limit.

However, the language of "plasmonics" is largely not needed to explain the behavior of optical antennas; after all, antennas work at microwave frequencies where the kinetic energy of electrons is negligible. Indeed, for an optical antenna we generally like to stay away from the plasmonic regime. Since $\omega_0 = ((L_K + L_F)C)^{-\frac{1}{2}}$, the primary plasmonic effect in optical antennas is to red-shift the resonance frequency thereby resulting in a reduction in the resonant length of the antenna, increasing $Q_{rad}$ and decreasing the antenna efficiency.

## 3.4 Electrically-injected antenna-LED cavity-backed slot antenna

Perhaps the primary advantage of the cavity-backed slot antenna for use in the antenna-LED is that electrical-injection is trivial [83]–[85]. Shown in Figure 3.8 is the basic approach. A pn junction ridge is be fabricated using dry etching (Figure 3.8a) and then metal is conformally deposited on top of the ridge (Figure 3.8b). This naturally forms the cavity-backed slot antenna where the slot length is defined by the ridge length ($L$) and the cavity depth is defined by the ridge height ($d_c$). The antenna is completely self-aligned to the ridge without the need for precise lithographical alignment. The ridge fully fills the cavity providing excellent coupling between the active region and antenna mode. Electrons are electrically-injected into the active region through the antenna and holes are injected through the p-type substrate. A thin insulator can be used to electrically isolate the antenna from the active region and underlying substrate.

There are several advantages to the antenna-LED coupled to a cavity backed slot antenna:

1. **Simple electrical injection.** The antenna also serves as the electrical contact and therefore a separate electrode does not need to be patterned.

2. **Self-alignment of the active region to the antenna.** It is not necessary to align the antenna feedgap to the active region.

3. **Large contact area for reduced contact resistance.** Electrical contact can be made to the entire top of the pn junction instead of a localized area as was the case for the electrically-injected dipole antenna shown earlier in the chapter.

4. **Directional light emission.** Light is emitted only downward into the substrate. Coupling the light into a waveguide with high coupling efficiency should be straightforward [41].

5. **Large thermal heat sink from antenna metal.** This will allow for much larger current density than typically allowed in normal LED structures. As shown later, this will allow for $\approx \mu$W output power.
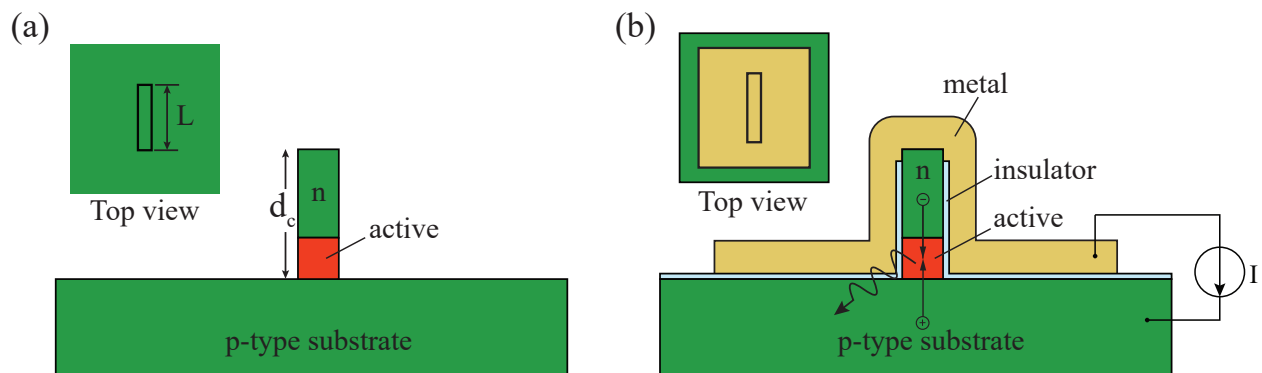


Figure 3.8: (a) Bare semiconductor pn junction ridge; and (b) bare ridge encapsulated with metal naturally forming the cavity-backed slot antenna.

# Chapter 4

# Electrically-injected III–V antenna-LED coupled to a cavity-backed slot antenna

In the previous chapter, the cavity-backed slot antenna was identified as an ideal choice for the electrically-injected antenna-LED. At the end of the chapter, a simplified electrically-injected antenna-LED design consisting of a cavity-backed slot antenna was proposed. In this chapter, a realistic antenna-LED design consisting of a nanoscale III–V pn junction ridge coupled to a cavity-backed is introduced. Building on the general design principles covered in the last chapter, the optimization of the III–V antenna-LED will be discussed. The fabrication of the antenna-LED and the measurement of the antenna-enhanced electroluminescence will then be shown.

## 4.1   Electrically-injected III–V antenna-LED

A III–V antenna-LED with a cavity-backed slot antenna is shown in Figure 4.1. The antenna-LED consists of a nanoscale double heterostructure InP/InGaAsP pn junction ridge covered with silver (Ag) metal. This geometry naturally forms a cavity-backed slot antenna where the cavity is filled with the pn junction ridge. Electrons are injected from the antenna into the InGaAsP active region through the top of the ridge whereas holes are injected into the active layer through a highly doped p-type InGaAsP layer. A thin 3 nm $Al_2O_3$ layer electrically isolates the sidewall of the active region from the antenna and a thick 150 nm spin-on-glass layer electrically isolates the antenna from the underlying p-type substrate.

The resonance wavelength of the cavity-backed slot antenna is tuned by changing the dimensions of the slot length ($L$) and the cavity depth ($d_c$), which in the antenna-LED is tantamount to changing length of the semiconductor ridge and thickness of the spin-on-glass spacer layer between the antenna metal and p-type substrate. The antenna resonance is designed to overlap the peak emission wavelength of the InGaAsP active region near
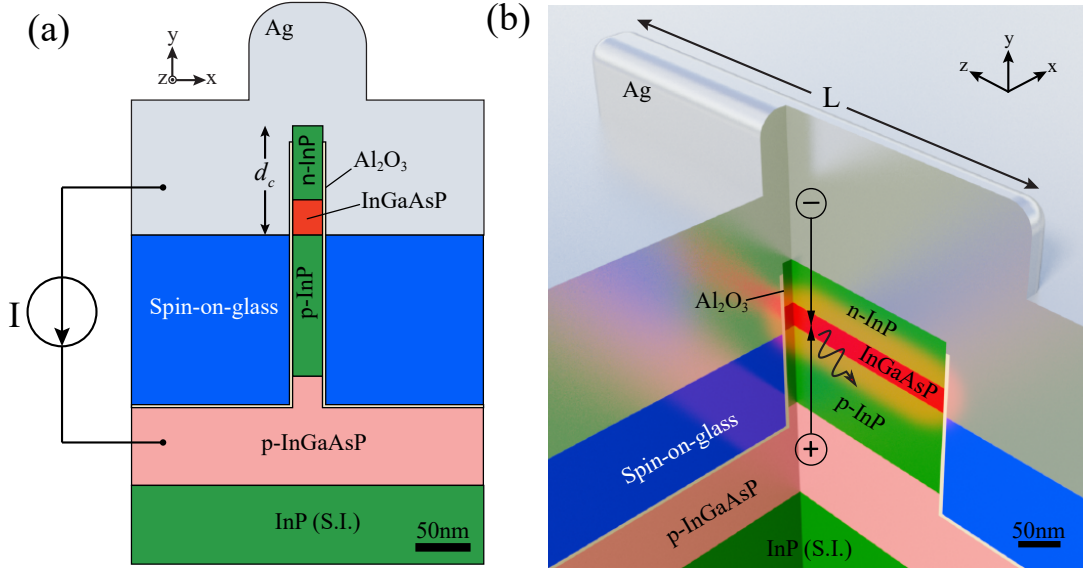
Figure 4.1: Illustrations of electrically-injected III–V antenna-LED coupled to a cavity-backed slot antenna. (a) Cross-sectional view showing details of the device layers; and (b) Cutaway view of the antenna-LED. The active region consists of double heterostructure InP/InGaAsP layers.

$\lambda_0 = 1.45~\mu m$ (corresponding to an emission frequency of 200 THz).

The InP is mostly transparent at a wavelength of 1.45 $\mu m$ therefore the emitted light from the antenna-LED can either be collected through the backside of the InP substrate or integrated with an on-chip waveguide similar to the waveguide coupled device reported in [41].

## 4.2   Optimizing the design for high spontaneous emission enhancement and antenna efficiency

### Choosing the slot length and cavity depth

Plotted in Figure 4.2a-c is a contour plot of the simulated antenna resonance wavelength, spontaneous emission enhancement, antenna efficiency and Q as a function of the slot length and cavity depth. Spontaneous emission enhancement was calculated as the ratio of the radiated power with antenna to the radiated power from the bare ridge without metal. Antenna efficiency was calculated as the radiated power divided by total power including loss. The quality factor was calculated by analyzing the ring-down of the energy in the simulation domain as a function of time.
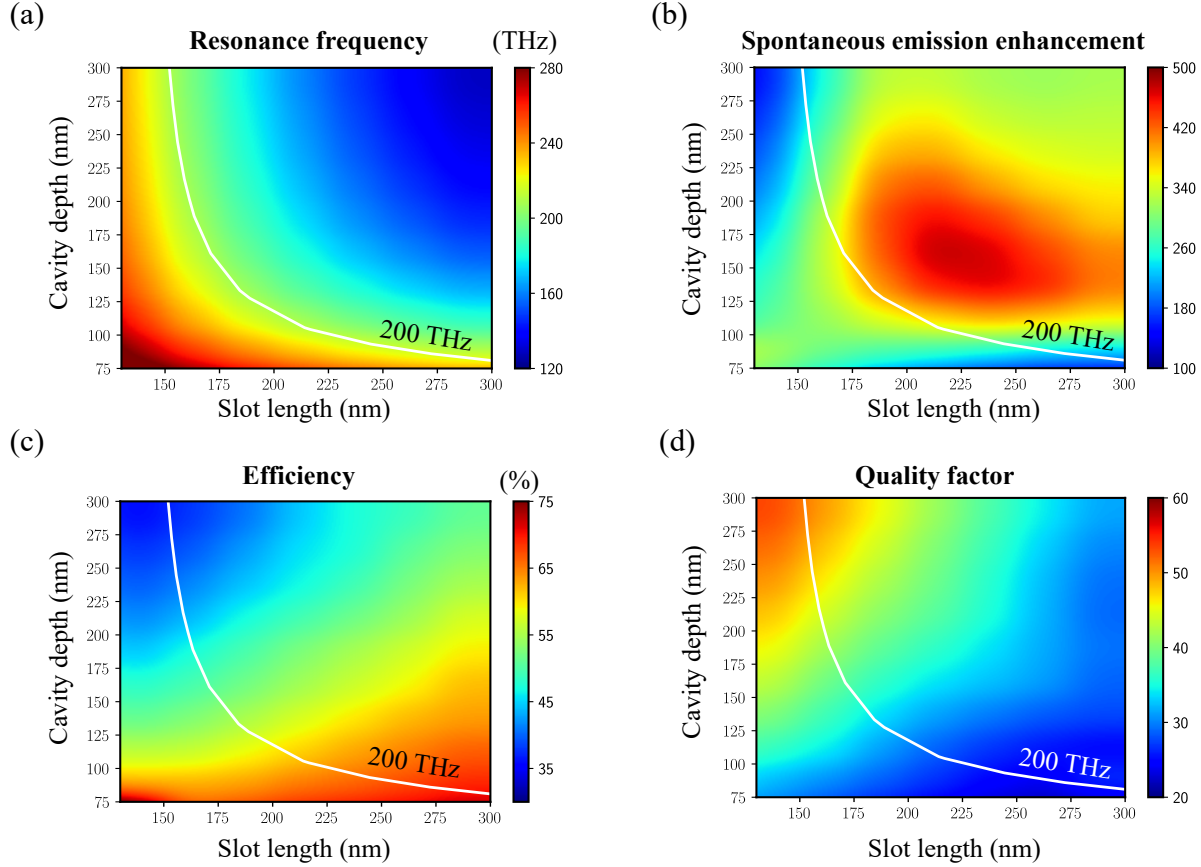
Figure 4.2: Contour plots of the (a) resonance frequency; (b) spontaneous emission enhancement; (c) antenna efficiency; and (d) quality factor of the III–V antenna-LED. The solid white contour line denotes the combinations of slot length and cavity depth that achieve antenna resonance at 200 THz.

In each plot in Figure 4.2, a solid white contour line denotes the values of slot length and cavity depth that can provide the desired antenna resonance frequency at 200 THz. As discussed in the previous chapter, the desired antenna resonance frequency can be met at many different combinations of slot length and cavity depth. However, not all combinations are equably favorable in terms of performance. The maximum spontaneous emission enhancement of about 380-fold occurs with a slot length of 175 nm and cavity depth of 150 nm and occurs when the antenna efficiency is about 50%. The antenna efficiency can be increased by increasing the slot length but at the expense of spontaneous emission enhancement.

There are also a number of other practical considerations in choosing the dimensions of the antenna. First, the cavity depth needs to be large enough to accommodate the pn junction device layers. Second, although it is not a fundamental issue, it is more desirable to choose a cavity depth where the antenna resonance is sensitive to the slot length. By

patterning many antenna-LEDs with varying slot length on an experimental chip, there will
then be a good chance to find a device with good overlap between the antenna resonance
and active region emission wavelength.

With all of these considerations in mind, a target cavity depth of 100 nm and slot length
of 220 nm was chosen.

## Improved performance with spacer oxide
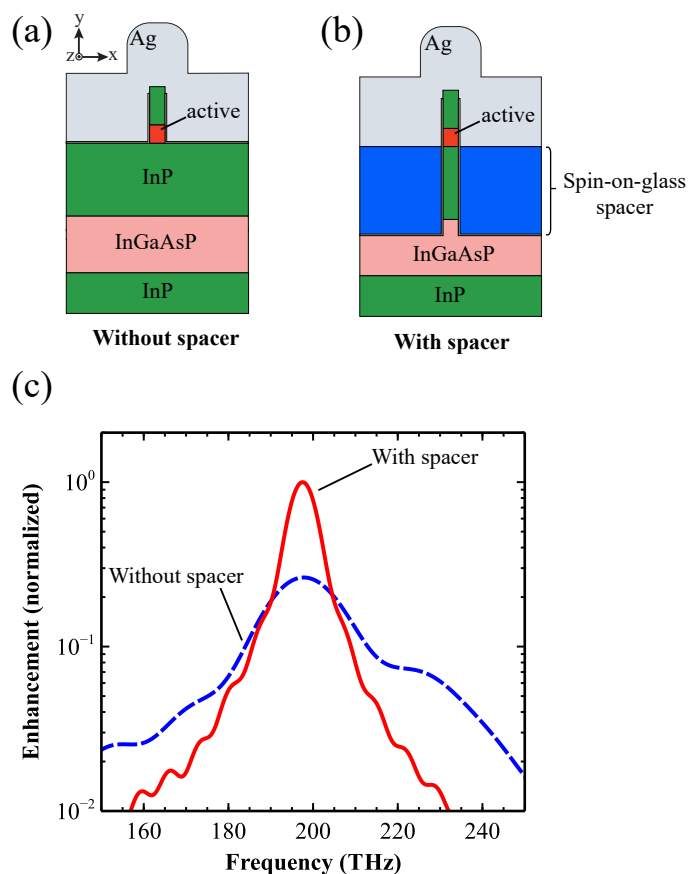


Figure 4.3: Comparison of antenna-LED with and without a spacer dielectric between the
substrate and antenna. Illustration of antenna-LED (a) without a spacer; and (b) with a
spacer. (c) Simulated spontaneous emission enhancement showing significant increase in the
enhancement with spacer.

The spontaneous emission enhancement of the cavity-backed slot antenna is inversely
proportional $n^2$ where $n$ is the refractive index of both the material filling the slot and the
substrate on which the antenna sits. Although we have no choice in this case but to fill the
cavity with a high-index semiconductor, we can engineer the effective index of the substrate.

Consider first the naive approach in which the cavity-backed slot antenna is filled with III–V semiconductor and also sits directly on the III–V substrate (Figure 4.3a). This design will suffer from the complete $n^2 \approx 10$-fold reduction in the spontaneous emission enhancement.

An improved approach and the one that is adopted here is to insert a low-index spacer between the antenna and the underlying substrate (Figure 4.3b). The low-index spacer reduces the effective index of the substrate therefore reducing the $n^2$ penalty.

Shown in Figure 4.3c is a plot of the normalized spontaneous emission enhancement for an antenna-LED with and without the spacer. The spontaneous emission enhancement is increased by about a factor of four when the spacer is inserted between the antenna and substrate thus reducing the effective index by roughly a factor of two.

The low-index spacer also serves to provide electrical isolation between the antenna and underlying substrate. Furthermore, at high modulation frequencies, the spacer will also be useful to reduce the capacitance and thus RC parasitic time constant of the antenna-LED.

## Spatial overlap of the mode with the active region
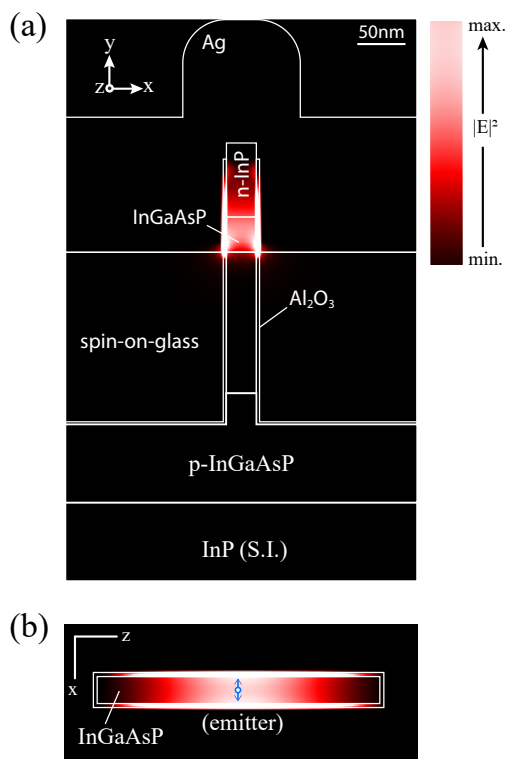


Figure 4.4: Simulated plots of $|E|^2$ for the antenna mode as viewed on the (a) $xy$-plane; and (b) $xz$ plane

Ideally, the active region of the antenna-LED is placed precisely at the maximum of the "hotspot" of the mode within the feedgap of the antenna. In practice, this is difficult to achieve and the entire active region will not see the maximum enhancement predicted in Figure 4.2b.

The antenna mode of the cavity-backed slot antenna resides primarily toward the bottom of the cavity and center of the slot region. This can be seen in the cross-sectional plots of the simulated electromagnetic energy density in Figure 4.4. The 35 nm thick InGaAsP active region is placed at the bottom of the cavity where spatial overlap with the antenna mode is highest (Figure 4.4a).

As viewed in the $xz$-plane (Figure 4.4b), the antenna mode is maximum in the center and falls off toward the ends of the slot. This is precisely what was predicted in the previous chapter. Therefore an emitter placed at $z = 0$ will see the highest enhancement.

Because of the spatial variation in the mode, the overall spontaneous emission enhancement seen by the active region is the maximum spontaneous emission observed at the center of the mode multiplied by some volume factor $\Gamma_V$. Several simulations were run by placing dipole emitters throughout the active region and measuring the total radiated power. $\Gamma_V$ was then calculated as this total radiated power divided by the total radiated power if all the dipoles were placed at the maximum of the antenna mode. In this manner, $\Gamma_V$ was found to be $\approx 0.5$.

## Penalty from electrically insulating the active region

As can be seen in Figure 4.4a, much of the antenna mode resides in the lower index $Al_2O_3$ that electrically isolates the active layer from the antenna. This is undesirable as it reduces the spontaneous emission enhancement that would otherwise be possible if the insulator was not present. It is shown in Appendix A that the $Al_2O_3$ effectively increases the width of the slot ($w$); making the electrical width of the slot appear larger than the physical width. This reduces the amount of current that is coupled into the antenna from a dipole emitter in the active region. An effective slot width ($w_{eff}$) can be defined as

$$w_{eff} = w + \frac{\epsilon_s}{\epsilon_{ox}} t_{ox} \tag{4.1}$$

where $\epsilon_s$ and $\epsilon_{ox}$ are the relative permittivity values of the InGaAsP and $Al_2O_3$ and $t_{ox}$ is the total $Al_2O_3$ thickness. The effective width ($w_{eff}$) in this case is $30 + \frac{3.17}{1.63}6 = 42$ nm. Recalling that the spontaneous emission enhancement goes as $w^{-2}$, the enhancement is reduced by a factor of $\left(\frac{30}{42}\right)^2 = 0.5$ when the ridge is cladded with $Al_2O_3$. This is a significant penalty to pay therefore the $Al_2O_3$ thickness must be reduced as thin as possible without resulting in high electrical leakage.
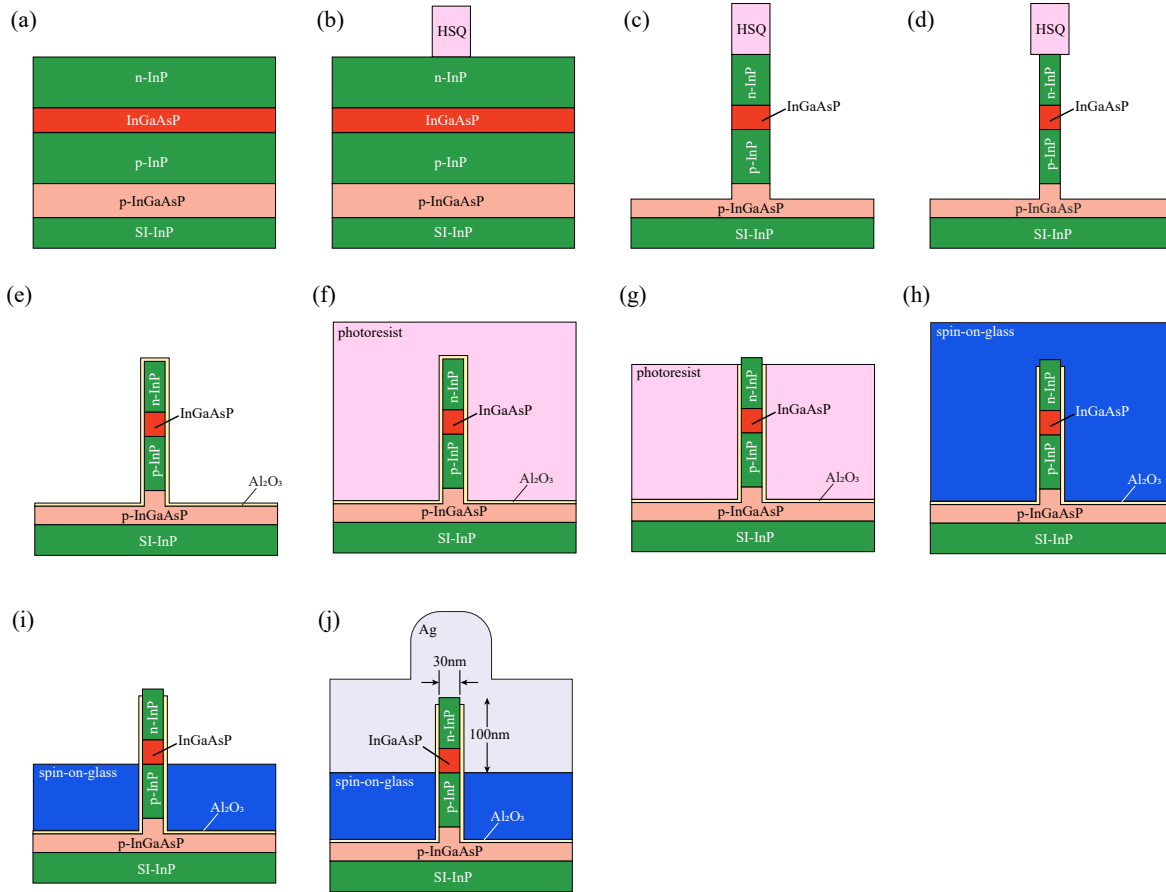
Figure 4.5: Simplified drawing of the fabrication process flow. (a) Start with epitaxial wafer; (b) pattern HSQ hard mask; (c) dry etch InP/InGaAsP ridge with ICP; (d) reduce the width of the ridge with digital etch; (e) deposit $Al_2O_3$ with ALD; (f) spin on photoresist; (g) etch back photoresist to expose top of ridge; (h) wet etch $Al_2O_3$ from top of ridge; (h) spin on spin-on-glass and cure; (i) etch back spin-on-glass; (j) pattern and deposit Ag antenna.

## 4.3 Fabrication of electrically-injected antenna-LED

The fabrication process of the electrically-injected antenna-LED began with a InP/InGaAsP double heterostructure light emitting diode (LED) structure epitaxially grown on a semi-insulating InP substrate (Figure 4.5a). The device layers consisted of a 35 nm thick nominally undoped InGaAsP active region sandwiched between higher bandgap p-type ($p_0 = 5 \times 10^{18}$ cm$^{-3}$) and n-type ($n_0 > 10^{19}$ cm$^{-3}$) InP layers. Detailed information on the thickness and doping concentration of the epitaxially grown layers can be found in Appendix E.

Next, electron beam lithography (EBL) was used to pattern the negative resist hydrogen silsesquioxane (HSQ) into narrow ridges to serve as a dry etch hard mask (Figure 4.5b).

Nanoscale InP/InGaAsP ridges were then etched using an inductively-coupled plasma (ICP) dry etch system with $Ar/H_2/CH_4/Cl_2$ gas at room temperature (Figure 4.5c).
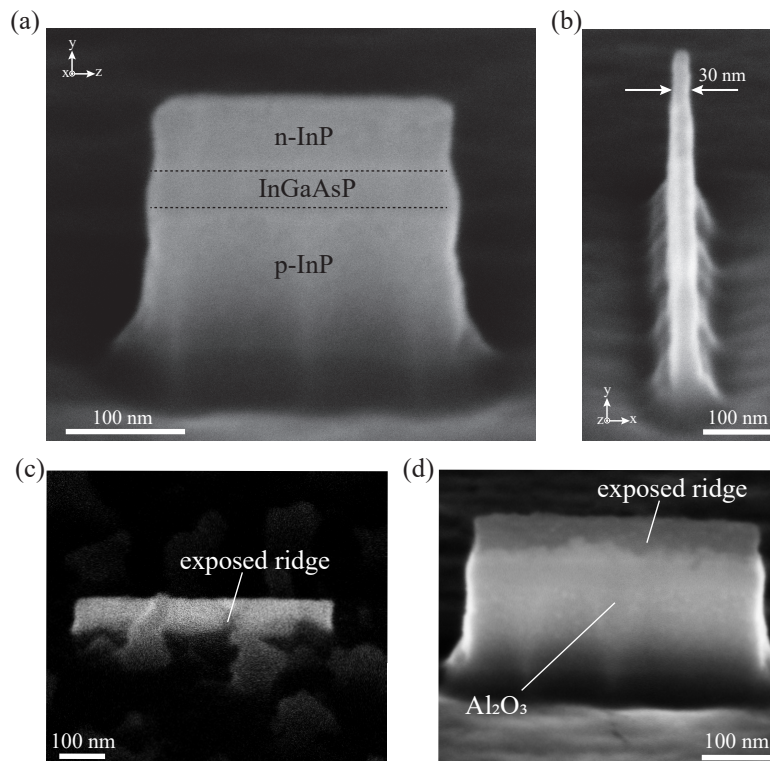


Figure 4.6: SEM images of the InP/InGaAsP ridge after several different process steps: (a-b) after dry etching; (c) after photoresist etch back; (d) after removal of $Al_2O_3$ from the top of the ridge

Several cycles of a digital etch were then used to further reduce the width of the ridge by approximately 20 nm (Figure 4.5d). The digital etch consisted of an $O_2$ plasma to oxidize the surface of the ridge followed by a dilute sulfuric acid etch to remove the oxide [86], [87]. This reduced the ridge width by 2 nm per digital etch cycle. The advantage of using the digital etch is that very narrow ridges can be fabricated using much wider hard mask thereby easing the lithography requirements. However, the digital etch was found to dramatically increase the surface recombination velocity; opposite to what was reported in [87]. The observed increase in surface recombination velocity will be discussed further in Chapter 5.

After dry etching, the HSQ hard mask was removed with a dip in hydrofluoric acid. Shown in Figure 4.6a-b are tilt-angle SEM images of a InP/InGaASP ridge after the dry etch process showing the steep sidewall and high-aspect ratio of the ridge.

The ridge was electrically insulated using a thin 3 nm $Al_2O_3$ deposited by atomic layer deposition at 200°C using trimethylaluminum (TMA) and water ($H_2O$) for aluminum and oxygen precursors respectively (Figure 4.5e). The $Al_2O_3$ on the top of the ridge was then
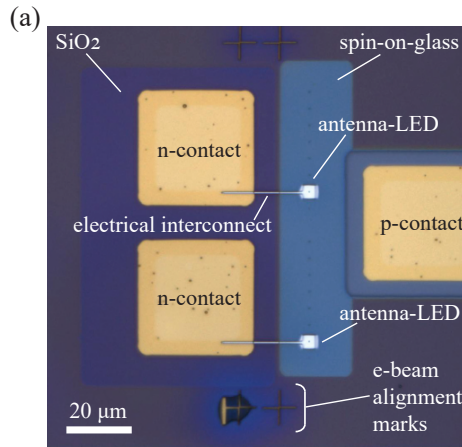
Figure 4.7: Front-side optical image of antenna-LED devices after fabrication.

removed to allow for electrical contact by first spinning on UV photoresist (PR) and etching back the PR with an $O_2$ until the top of the ridge was exposed (Figure 4.5f-g). An tilt-angle SEM image of a ridge after the PR etchback process is shown in Figure 4.6c. Then, the $Al_2O_3$ on the exposed portion of the ridge was removed with buffered hydrofluoric acid. The PR was then stripped off the sample using a standard solvent clean. The end result after removal of the $Al_2O_3$ on top of the ridge is shown in Figure 4.6d.

The surface was planarized by spinning on HSQ followed by high temperature curing to cross-link the HSQ and form spin-on-glass (Figure 4.5h). Next, the spin-on-glass was etched back with a $SF_6$/He plasma until the top of the spin-on-glass corresponded with the bottom of the InGaAsP active region (Figure 4.5i). Finally, the silver (Ag) antenna was patterned using EBL and the Ag (with a 5 nm thick germanium wetting layer) was deposited using e-beam evaporation (Figure 4.5j). Angled evaporation with an in-situ tilt stage was employed during evaporation to ensure good metal coverage on the sidewall of the ridge. More details on the tilt-evaporation can be found in Appendix D.

After evaporation and lift-off of Ag antenna metal, a 10 nm $Al_2O_3$ layer was deposited by ALD on top of the sample to act as a barrier to corrosion of the Ag. Finally standard UV-lithography and e-beam evaporation with liftoff was used to pattern and deposit the gold (Au) n and p-type probe pads for testing.

An optical image of two processed device is shown Figure 4.7. The devices share a common ohmic p-contact probe pad to the highly doped p-InGaAsP layer whereas each antenna-LED has its own n-contact probe pad. The n-contact probe pad is placed on a e-beam evaporated $SiO_2$ layer to ensure electrical isolation between the n-contact and underlying p-type layer. An electrical interconnect is routed between the antenna-LED and n-contact probe pad for biasing. The field area is covered with spin-on-glass which appears dark purple in Figure 4.7. The light blue band running vertically in the image is the etched back spin-on-glass layer which serves to isolate the antenna from the underlying substrate.

Finally, several e-beam alignment marks can be observed; these were used to align the antenna to the semiconductor ridge.
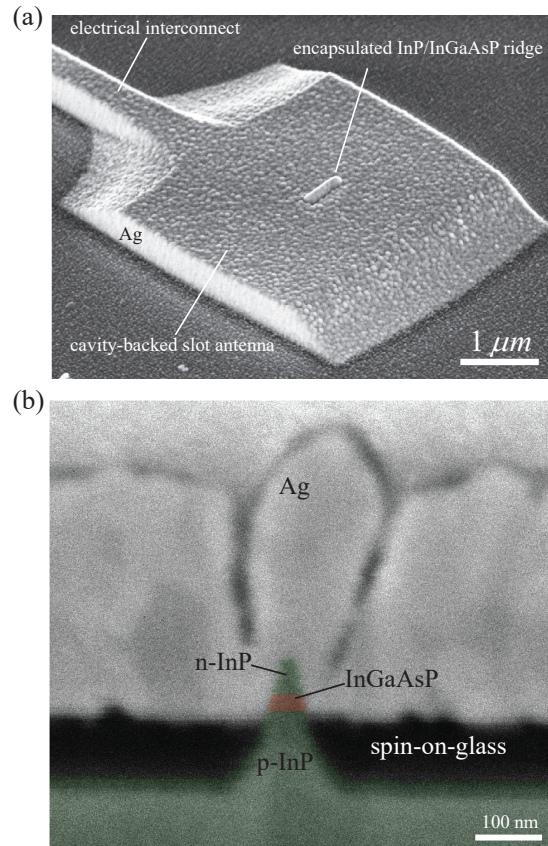


Figure 4.8: (a) Scanning electron microscope (SEM) tilt-view image of an antenna-LED; and (b) focused ion beam (FIB) cross-section of an antenna-LED device.

Shown in Figure 4.8a is a scanning electron microscope (SEM) image of the antena-LED. The InP/InGaAsP ridge is fully encapsulated with Ag metallization after the tilted metal evaporation. The sidewalls of the antenna that run parallel with the long axis of the ridge have a very shallow angle owing to the tilted evaporation. The electrical interconnect that routes from the antenna to the probe pad can be seen in the upper-left corner of Figure 4.8b.

The focused ion beam (FIB) cross-section of an antenna-LED can be seen in Figure 4.8b showing clear detail of the device layers. False color is used to help improve the visibility of the materials. Excellent coverage of the Ag antenna and spin-on-glass layer is observed along the sidewall of the InP/InGaAsP ridge. It should be noted that the FIB image shown in Figure 4.8b was taken of a device that was fabricated with an unoptimized dry etch process that lead to shallower etch angle than what is observed in Figure 4.6b.

## 4.4 Measurement of the antenna resonance
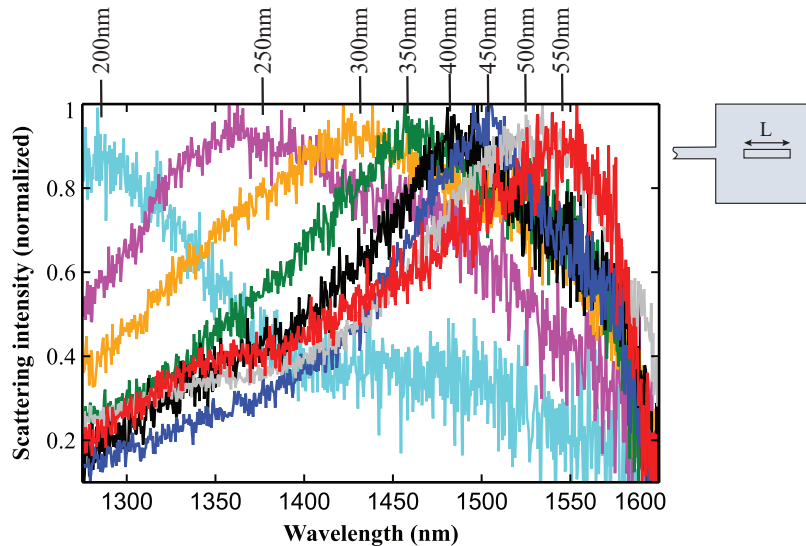


Figure 4.9: Normalized scattering intensity for several slot lengths showing clear blue-shift in the resonance peak as the slot length is scaled down. Each colored plot refers to the scattering spectrum for antenna-LED devices with different ridge length (L).

Dark-field spectroscopy was used to probe the resonance behavior of the antenna-LEDs to confirm overlap of the antenna resonance with active region emission. Several test arrays consisting of antenna-LED devices with varying slot length were illuminated obliquely through the backside of the substrate with a broadband lamp. Light that was scattered off the antennas was captured by the objective and focused onto the input slit of a spectrograph with liquid nitrogen cooled InGaAs CCD for spectral measurement. In that manner, the scattered light spectrum as a function of slot length was measured. To increase the signal-to-noise ratio, $\approx 20$ antenna-LED devices was measured for each slot length and a polarizer was placed in front of the spectrometer and aligned parallel with the polarization of the antenna mode.

The p-InGaAsP layer absorbs light with $\lambda > 1.2 \ \mu m$ and therefore was removed prior to the dark-field measurement. This was done by flip-chip mounting the sample on a glass side using optical epoxy. The InP substrate and p-InGaAsP layer was then removed through mechanical lapping and wet etch. Although the data are presented here first, the actual dark-field measurement was performed last because of the destructive sample preparation. More details of the dark-field spectroscopy experimental setup can be found in Appendix C.

The scattered light spectra of antenna-LED devices with varying slot length are plotted in Figure 4.9. A clear blue shift is observed in the resonance peak as the slot length is reduced. The blue-shift becomes more pronounced as the slot length is reduced below 400 nm. These observations are consistent with the simulated resonance plot of the cavity-

backed slot antenna discussed previously. Given the active region emits at a wavelength of
$\lambda_0 = 1.45$ $\mu$m, the antenna-LEDs with slot length between 300 and 500 nm long provide
the best overlap with the antenna resonance; this is slightly longer than what was predicted
with simulation.

## 4.5   Electroluminescence (EL) measurement

### Measuring the antenna effect
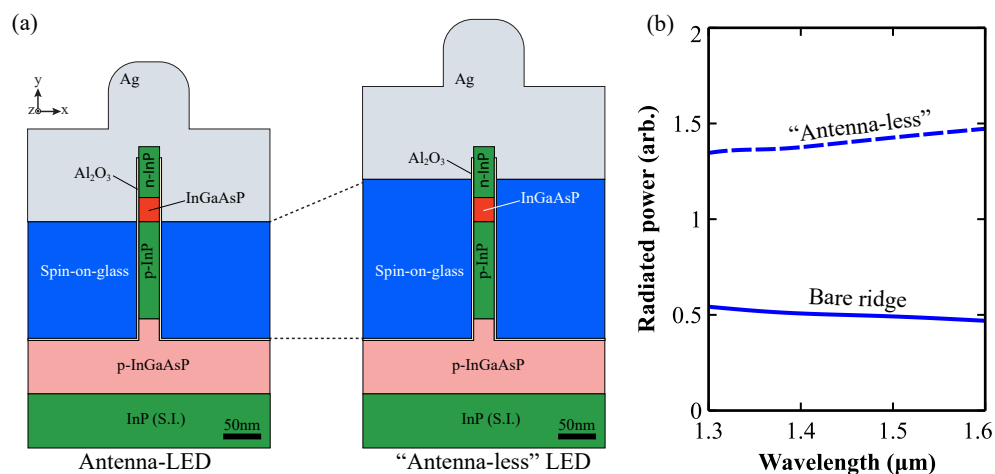


Figure 4.10: (a) Schematic of the antenna-*less* LED used as a reference device to quantify
the effect of the antenna. The antenna-*less* LED was fabricated by locally increasing the
thickness of the spin-on-glass spacer layer (blue) between the substrate and antenna. (b)
Simulated radiated power of the antenna-*less* LED compared to the bare ridge showing that
the antenna-*less* LED is a reasonably good proxy for the bare ridge.

Quantifying the effect of the antenna on the light emission of the antenna-LED requires
the measurement of an identical device without antenna. For an optically pumped device
this is trivial: one device is fabricated with an antenna and another without an antenna.
Both devices are optically pumped and the photoluminescence intensity or time-resolved
photoluminescence results are compared. For the electrically-injected antenna-LED this is
not as straightforward because the antenna serves as both an antenna as well as an electrical
contact. Ideally, we would like to compare the light emission from the antenna-LED and
the bare III–V ridge without any metal. However, if the antenna is removed, it is no longer
possible to electrically-inject the the device.

To circumvent this problem, an antenna-*less* LED was fabricated by locally increasing
the thickness of the insulator region between the antenna and underlying substrate as shown
in Figure 4.10a. In this manner, the antenna-*less* LED can still be electrically-injected

while the active region no longer couples to the antenna and should behave similarly as if radiating into free-space. This was confirmed by simulating the average radiated power from $\hat{x}$, $\hat{y}$, and $\hat{z}$-dipoles in the active region of the antenna-*less* LED and comparing with the average radiated power from the same dipoles placed in bare ridge without metal. The radiated power as a function of wavelength is shown for both of these scenarios in Figure 4.10c. It can be seen that the spontaneous emission rate enhancement of the antenna-*less* LED is similar as the bare ridge without metal. The radiated power of the antenna-*less* LED is slightly higher, therefore we may expect that any measured spontaneous emission enhancement will be a lower bound to the actual spontaneous emission enhancement; more on this later in the chapter.

The electroluminescence (EL) from both antenna-LED and antenna-*less* devices was measured by forward-biasing individual devices with constant current and collecting the emitted light through the backside of the InP substrate. Antenna-LED devices with varying slot length were fabricated and measured on the same chip. For each antenna-LED measured, an antenna-*less* device with otherwise identical device dimensions was also measured. For all measurements, the current density was kept constant at $J = 6$ kA/cm$^2$. More details of the experimental setup of the EL measurement are discussed in Appendix C.

## Electroluminescence from antenna-*less* LEDs

Shown in Figure 4.12a are EL spectra from the measured antenna-*less* LEDs with varying ridge length ($L$). The light emission from the antenna-*less* devices is weak with a peak intensity near $\lambda = 1.45$ $\mu$m consistent with the bandgap of the active region material. The shape of the EL spectra is independent of the ridge length as expected. Several different antenna-*less* devices were measured for each ridge length; only the brightest devices are plotted in Figure 4.12a.

## Electroluminescence from antenna-LEDs

The dark-field image of two unbiased antenna-LEDs as viewed through the polished InP substrate is shown in Figure 4.11. The dark-field image was captured by collecting and focusing the scattered light onto a thermoelectric-cooled 2D InGaAs CCD camera. Strong light emission is observed after the topmost antenna-LED is forward biased with $J = 6$ kA/cm$^2$ of forward current (the bottom-most antenna-LED remains unbiased and therefore no light is emitted).

Plotted in Figure 4.12b is the measured EL from the antenna-LED devices showing two clear indications of antenna-enhanced spontaneous emission:

1. **Increased EL intensity**. The intensity of the EL emission from the antenna-LED devices is significantly brighter than the emission from the antenna-*less* devices indicating the quantum efficiency of the antenna-LED devices increased from enhanced spontaneous emission.
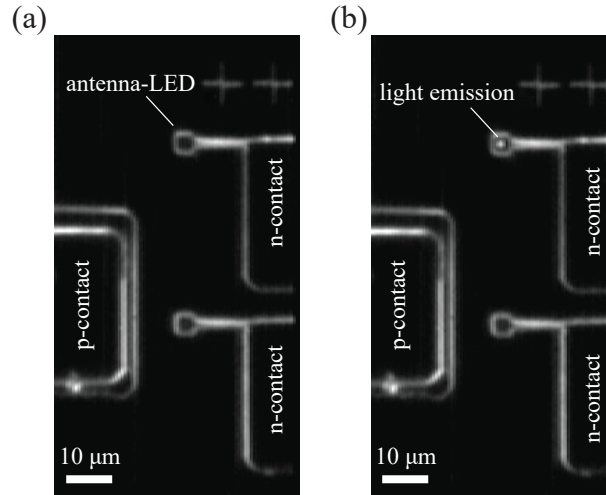
Figure 4.11: (a) Dark-field image of an unbiased antenna-LED device as viewed through the InP substrate; and (b) Dark-field and electroluminescence image after the top-most antenna-LED is forward biased. Bright emission is observed.

2. **Blue-shift of emission wavelength as ridge length is decreased**. The peak wavelength of the emission spectra blue-shifts as the ridge length is decreased. This is consistent with the expected behavior of the cavity-backed slot antenna and consistent with the direct measurement of the antenna resonance behavior with dark-field scattering.

The resonance wavelengths observed in the EL data correspond roughly to the scattering measurements discussed previously. The resonance measured from the dark-field measurement is somewhat red-shifted compared to the EL data. Because of the removal of the substrate prior to the dark-field measurement, the antenna-LEDs were effectively emitting into a slightly lower index which can explain the slight discrepancy between the dark-field and EL data. Full-wave simulations predict an $\approx 20$ THz red-shift in the antenna resonance frequency after removal of the substrate; consistent with the data observed here.

## Electroluminescence enhancement

The EL enhancement is plotted in Figure 4.12c by taking the ratio of each antenna-LED spectrum in Figure 4.12b with the its respective antenna-*less* spectrum in Figure 4.12a. This effectively extracts the spectrum of the antenna resonance from the overall emission spectrum of each antenna-LED. The EL enhancement is proportional to the slot length with the largest EL enhancement of $\approx 25$-fold occurring for a ridge length of 550 nm. The antenna-LED with a slot length of 450 nm had an EL enhancement of $\approx 20$-fold and was found to provide the
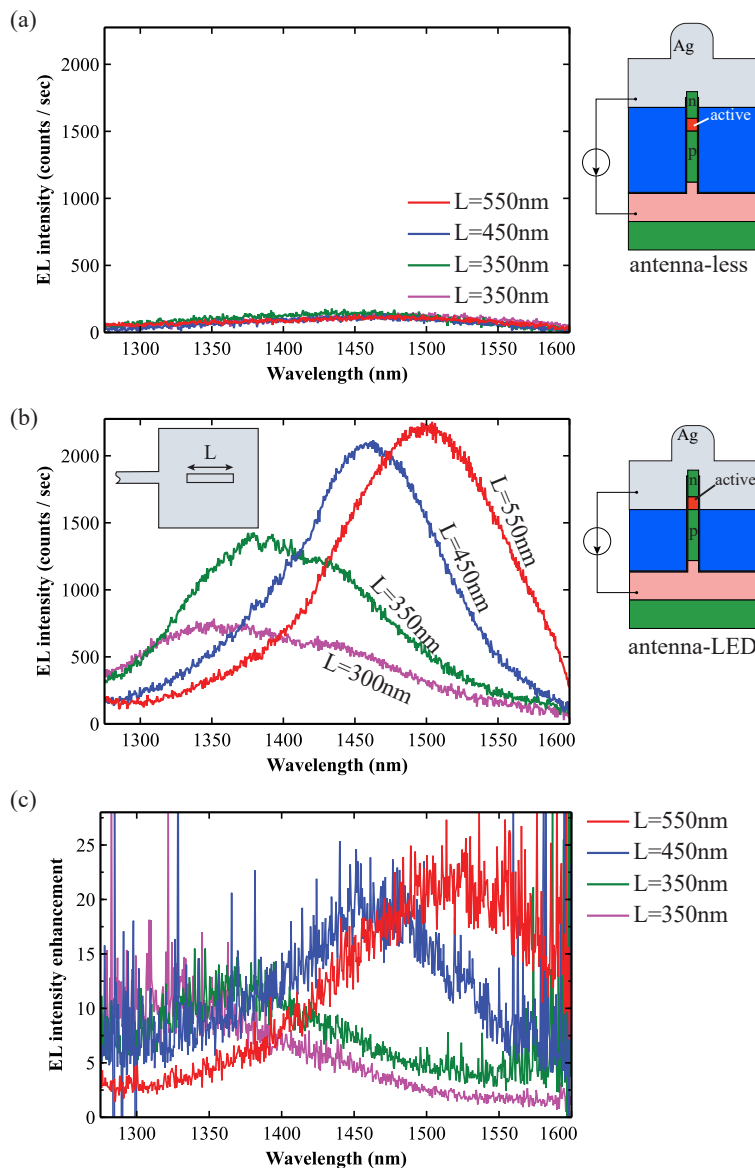
Figure 4.12: Electroluminescence measurement of (a) antenna-*less*; and (b) antenna-LED devices for various slot lengths. (c) Plot of the EL enhancement which is the ratio of the antenna-LED EL spectrum in (a) to the antenna-*less* EL spectrum in (b).

antenna resonance wavelength with the best overlap of the intrinsic emission wavelength of the active region.

The observation that the EL enhancement increases with slot length suggests that the antenna efficiency is lower than expected. This is likely a result of higher than expected Ohmic losses which can be improved through optimized metal deposition [88].

## Polarization of the light emission
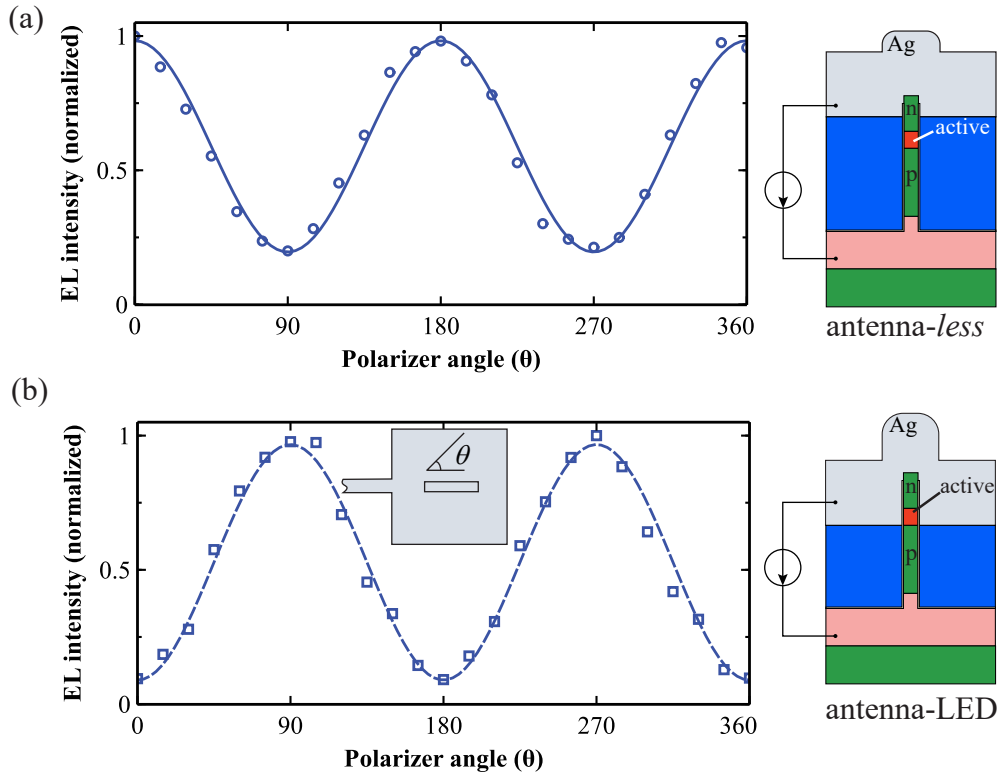


Figure 4.13: Normalized EL intensity plotted as a function of polarizer angle ($\theta$) for the (a) antenna-*less* LED; and (b) antenna-LED. The inset in (b) shows the orientation of $\theta$ with respect to the slot.

In Figure 4.13a-b, the polarization preference of the emitted light from the antenna-LED and antenna-*less* LED is shown by plotting the spectrally integrated EL intensity as a function of polarizer angle ($\theta$) for a device with ridge length of 450 nm. The angle $\theta$ is measured with respect to the orientation of the ridge such that $\theta = 0°$ refers to the polarizer aligned along the long axis of the ridge.

The emitted light of the antenna-LED was predominantly polarized with electric field along the short-axis of the slot ($\hat{x}$-direction) consistent with the expected behavior of the cavity-backed slot antenna. In contrast, the emitted light of antenna-*less* LED was polarized along the long axis of the ridge ($\hat{y}$-direction). This can be attributed to the strong index anisotropy observed by a dipole emitter in the bare semiconductor ridge. Similar behavior has been observed in other nanoscale semiconductor ridge structures and nanowires [89].

## 4.6   Measurement of spontaneous emission enhancement

**Time-resolved photoluminescence**
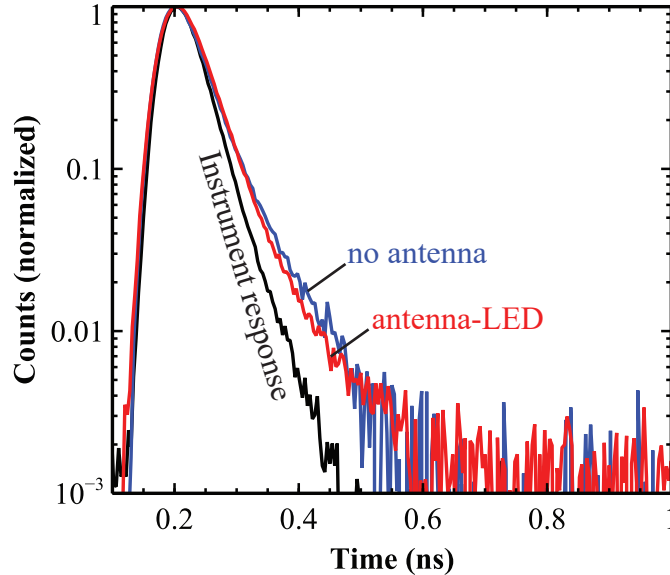


Figure 4.14: Time-resolved photoluminescence measurement of the antenna-*less* LED (blue), antenna-LED (red), and instrument response function (black).

Time-resolved photoluminescence (PL) was measured by exciting the InGaAsP active region with a short laser pulse from a Ti:Sapphire femtosecond laser ($\lambda = 1000$ nm and pulse width $< 200$ fs). The light emission from the active region region was then monitored as a function of time and a decay rate was extracted using time-correlated single photon counting (TCSPC). The experimental setup for the TCSPC measurement is described in more details in Appendix F.

Plotted in Figure 4.14 is the time-resolved PL from the antenna-LED (red curve) and antenna-*less* LED (blue curve) with ridge length of 450 nm along with the instrument response function (black curve). The decay time ($\tau$) of the antenna-LED and antenna-*less* LED are nearly indistinguishable and measured to be $\tau \approx 20$ ps. The data suggest then that non-radiative recombination is the dominant recombination pathway in the antenna-LED and therefore the decay time extracted from the curves in Figure 4.14 is simply the non-radiative lifetime.

III–V semiconductors are known to have relatively high surface recombination velocity which can significantly reduce the efficiency of nanoscale III–V light emitting devices. In-GaAsP typically has surface recombination velocity of about $10^4$ cm/s; however, the surface

recombination velocity ($v_s$) was separately measured and found to be $v_s > 10^5$ cm/s significantly higher than expected. This is attributed to process induced surface damage and will be discussed in greater detail in Chapter 5. The non-radiative lifetime ($\tau_{nr}$) can then be approximated as $\tau_{nr} \approx w/(2v_s) = 30 \times 10^{-9}/(2 \times 10^5) = 15$ ps consistent with the measured decay time.

## Efficiency as a gauge for spontaneous emission enhancement

Since the spontaneous emission enhancement is inaccessible from the time-resolved PL, an alternative approach is needed.

In the limit of dominant non-radiative rate, the quantum efficiency (QE) for the antenna-LED can be written as

$$\text{QE} = \frac{F\tau_{rad}^{-1}}{F\tau_{rad}^{-1} + \tau_{nr}^{-1}} \approx F\frac{\tau_{nr}}{\tau_{rad}} \tag{4.2}$$

where $\tau_{nr}$ is the non-radiative lifetime, $\tau_{rad}$ is the bulk radiative lifetime (without antenna), and $F$ is the spontaneous emission enhancement. Therefore, the spontaneous emission enhancement can be measured directly from the increase in the quantum efficiency of the device. Low quantum efficiency is obviously not desirable for a practical device but we can take advantage of it here to extract the spontaneous emission rate enhancement in a reasonably straightforward manner. Strategies on increasing the quantum efficiency will be discussed later in Chapter 5.

In (4.2), $F$ should be considered the overall spontaneous emission enhancement averaged over all dipole orientations and weighted by the emission spectrum of the active region. However, we are mostly interested in the peak enhancement ($F_{peak}$) for a dipole with identical angular frequency and polarization of the antenna mode. The cavity-backed slot antenna is a linearly polarizing antenna and will only enhance dipoles that are oriented transverse to the long axis of the slot ($\hat{x}$-direction). Therefore, the peak spontaneous emission enhancement ($F_{peak}$) is written

$$F_{peak} = \left.\frac{I_{x,ant}}{I_{x,0}}\right|_{maximum} \tag{4.3}$$

where $I_{x,ant}$ and $I_{x,0}$ is the intensity of light emitted by an $\hat{x}$-dipole when exciting an antenna-LED and antenna-*less* LED respectively.

The $\hat{x}$-dipole will have an electric-field component only in the $\hat{x}$-direction when the light is collected directly underneath the device (i.e. the microscope objective is placed at $x = z = 0$ using the coordinate system defined Figure 4.1). Similarly, the $\hat{y}$-dipole and $\hat{z}$-dipole will only have $\hat{y}$ and $\hat{z}$ components in the far-field. Therefore, the intensity of light emitted by the $\hat{x}$-dipoles can be resolved from the other polarization directions by inserting a polarizer aligned in the $\hat{x}$-direction. The emission spectra of the antenna-LED and antenna-*less* LED can then be measured and $F_{peak}$ extracted by applying (4.3). However, the spectrum of $\hat{x}$-polarized light emitted by the antenna-less LED ($I_{x,0}$) was too weak to be reliably measured.

Instead, it was recognized that $I_{x,0} = \alpha I_{y,0}$ where $\alpha = I_{x,0}/I_{y,0} = 0.2$ is the polarization ratio extracted from Figure 4.13.

Given the light from the antenna-LED was almost completely $\hat{x}$-polarized and the light from the antenna-*less* LED was almost completely $\hat{y}$-polarized, $F_{peak}$ was extracted by dividing the EL enhancement in Figure 4.12c by $\alpha$. After doing so, we found a peak spontaneous emission enhancement of $\approx$100-fold for the antenna-LED with slot length of 450 nm.

**Taking into account light extraction efficiency**

The above analysis assumed that the light extraction efficiency of the antenna-LED and antenna-*less* LED were similar; however, in general, this is not necessarily the case. The light extraction will depend upon the numerical aperture of collection optics, radiation pattern of the LEDs, and metal loss. Furthermore, some collection of light from $\hat{y}$ and $\hat{z}$-dipoles is inevitable and cannot be completely avoided since the light is not collected from a singular point in the far-field but rather a finite collection area related to the NA of the collection optics. Differences between the light extraction efficiency between the two devices will lead to an under-prediction or over-prediction of the calculated spontaneous emission enhancement from the ratio of measured light intensity. Full-wave simulation was used to account for the extraction efficiency and put a bound on the measured 100-fold spontaneous emission enhancement.
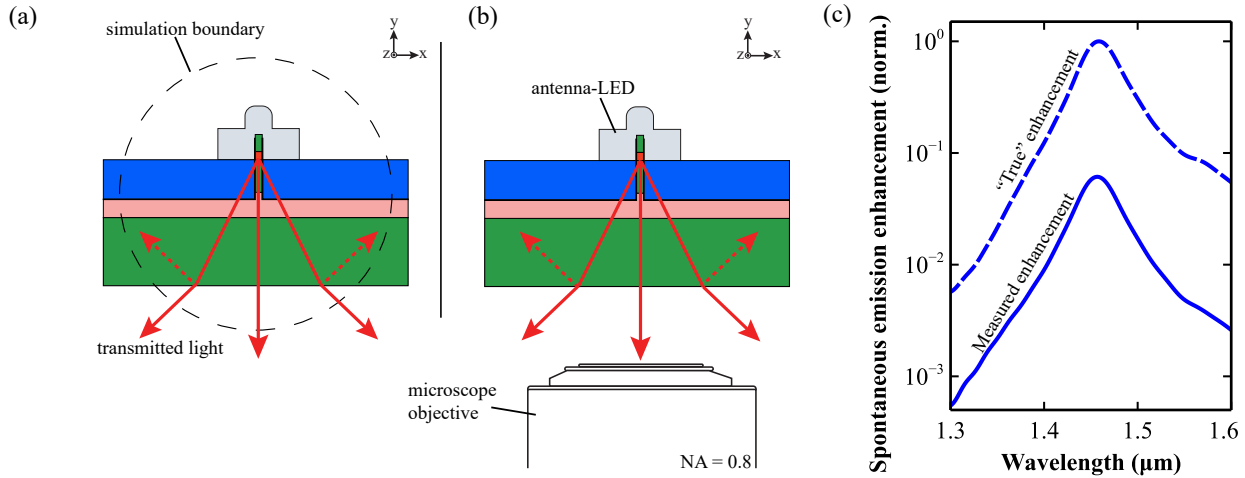


Figure 4.15: Simulation to calculate the effect of extraction efficiency on spontaneous emission enhancement measurement. (a) "True" spontaneous emission enhancement measured by exciting the antenna-LED with a dipole and measure the total radiated power leaving the computational domain; (b) experimentally measured spontaneous emission enhancement. Only the power collected by the microscope objective is measured; and (c) comparison of the spontaneous emission enhancement measured using the two different methods.

To understand the effect of light extraction efficiency on the measured spontaneous emission enhancement, two simulations were run:

1. **"True" spontaneous emission enhancement** (Figure 4.15a). The true spontaneous emission enhancement was simulated by taking the ratio of the total radiated power of the antenna-LED and antenna-*less* LED when excited by an $\hat{x}$-dipole only. The simulated radiated power was integrated from an ideal far-field sphere that surrounds the entire device.

2. **Experimentally measured spontaneous emission enhancement** (Figure 4.15b). The experimentally measured spontaneous emission enhancement was simulated by taking the ratio of the total radiated power of $\hat{x}$-polarized light from the antenna-LED and antenna-*less* LED when excited by $\hat{x}$, $\hat{y}$ and $\hat{z}$-dipoles. The simulated radiated power was integrated only along the the effective aperture opening of a microscope objective with NA = 0.8. Fresnel reflections including the effect of Snell's Law were fully taken into account.

Plotted in Figure 4.15c are the results of both simulations showing that the experimentally measured spontaneous emission enhanced is expected to be lower than the actual spontaneous emission enhancement by about an order of magnitude. The reason for the discrepancy is a result of the large contribution to the intensity of measured light from $\hat{z}$-dipoles in the antenna-*less* device. It is concluded then that the measured 100-fold spontaneous emission enhancement is a lower bound on the actual spontaneous emission enhancement.

## 4.7 Increasing the enhancement with a quantum well antenna-LED

The antenna-LED presented in the previous sections consists of a double heterostructure bulk active region with isotropic dipole emission. Because the cavity-backed slot antenna is linearly polarizing, only a third of the dipoles will be enhanced by the antenna. This dipole averaging will limit the overall increase in the spontaneous emission rate enhancement.

An improved active region design shown in Figure 4.16a consists of a multiple quantum well (MQW) active region with 6 nm thick InGaAs quantum wells cladded by InGaAsP. Quantum confinement in one-direction leads to an in-plane ($xz$-plane) polarization preference for dipole emission for the dominant conduction band to heavy-hole transition. Therefore, the effect of dipole averaging is reduced since now half of the dipoles will observe antenna-enhanced spontaneous emission. The dipole averaging is described in much greater detail in Chapter 6.

Antenna-LED devices were fabricated in much the same manner as described in the previous section for the double heterostructure antenna-LED. In addition to the improved active region, the thickness of the $Al_2O_3$ layer was also reduced from 3 to 1 nm to improve the emitter-antenna coupling. To accommodate the multiple quantum well device layers, the
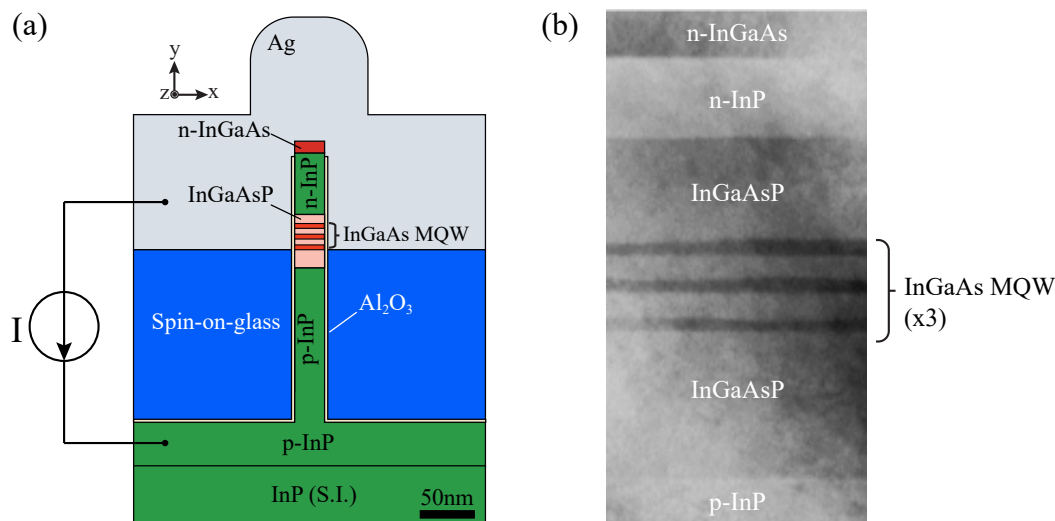
Figure 4.16: (a) Antenna-LED with multiple quantum well active region; and (b) transmission electron microscope image of the multiple quantum well active region [90]

cavity-depth was increased to 150 nm (compared to 100 nm for the double heterostructure antenna-LED).

## Electroluminescence of quantum well antenna-LED
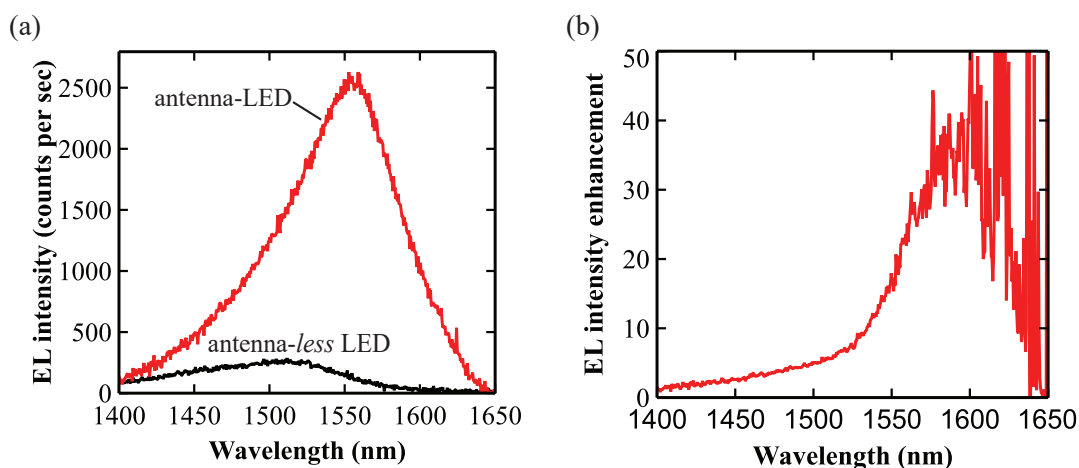


Figure 4.17: (a) Electroluminescence spectra of the quantum well antenna-LED and antenna-*less* LED; and (b) EL enhancement spectrum of the devices in (a).

Electroluminescence (EL) was measured in the same manner as the double heterostructure device. Both MQW antenna-LED and antenna-*less* devices were patterned with varying

slot length. Evidently because of the deep cavity-depth, the resonance was very sensitive to slot length and only antenna-LEDs with slot length of 250 nm provided reasonably good overlap of the antenna resonance with the active region wavelength near $\lambda_0 \approx 1.5$ $\mu$m. Shown in the Figure 4.17a are the EL spectra of the antenna-LED and identically sized antenna-*less* LED forward-biased with $J = 12$ kA/cm$^2$ of current. Bright light emission from the antenna-LED with respect to the antenna-*less* LED was observed. Plotted in Figure 4.17b is the EL enhancement spectrum which was calculated by taking the ratio of the two spectra in Figure 4.17a. A large 40-fold increase in the EL intensity is observed with the antenna-LED device. The peak of the EL enhancement is centered near $\lambda_0 = 1600$ nm which is red-shifted slightly with respect to the intrinsic active region emission wavelength near $\lambda_0 = 1500$ nm. A spontaneous emission enhancement of $\approx 200$-fold was extracted from the EL enhancement in Figure 4.17b using the same methodology reported in the previous section. This is a factor of two higher than the spontaneous emission enhancement of the double heterostructure antenna-LED thus suggesting the usefulness of the quantum well active region and reduced Al$_2$O$_3$ thickness.

## Quantum efficiency of the quantum well antenna-LED

The quantum efficiency (QE) of the quantum well antenna-LED can be estimated as

$$
\begin{aligned}
&= \frac{q(\text{photon counts per sec})}{(\text{collection efficiency}) \times (\text{microscope throughput}) \times (\text{current})} \\
&= \frac{q(20 \times 10^4)}{(0.1) \times (0.1) \times (10^{-6})} \\
&= 10^{-5}
\end{aligned}
\tag{4.4}
$$

where the photon counts per second was measured by spectrally integrating the light in Figure 4.17a, the microscope throughput is estimated through separate calibration measurement, and the collection efficiency is estimated through full-wave simulation. The calculated quantum efficiency is rather low at $10^{-5}$ which is not large enough for an efficient on-chip optical link. What is the expected quantum efficiency?

The injected carrier density can be estimated as

$$
\frac{J}{q d_{QW}} \cong \frac{n}{\tau_{nr}}
\tag{4.5}
$$

where $\tau_{nr}$ is the non-radiative lifetime from surface recombination at the active region surface and is given approximately by

$$
\tau_{nr} \cong \frac{1}{v_s} \frac{\text{Vol.}}{\text{Area}} \cong \frac{w}{2v_s} = \frac{30 \times 10^{-7}}{2 \times 10^4} = 120 \text{ps}
\tag{4.6}
$$

where $v_s$ is the surface recombination velocity and we have initially assumed $v_s = 10^4$ cm/s. Therefore, from (4.5) the carrier density is calculated as $n \approx 5 \times 10^{18}$. Finally, the expected

quantum efficiency is calculated as

$$QE \cong \frac{B_0 n^2}{n/\tau_{nr}} = B_0 n \tau_{nr} = (10^{-10})(5 \times 10^{18})(120 \times 10^{-12}) = 0.06 \tag{4.7}$$

where $B_0$ is the radiative coefficient and for simplicity antenna-enhanced spontaneous emission rate has been ignored. Therefore, the expected quantum efficiency is at least three orders of magnitude higher than the actual quantum efficiency.

Why is there a discrepancy and what can be done to increase the quantum efficiency? This will be the topic of the next chapter. It will be shown that the actual value of surface recombination velocity $(v_s)$ is more than an order of magnitude higher than the assumed value of $10^4$ cm/s. An order of magnitude increase in $v_s$ will decrease both $n$ and $\tau_{nr}$ by an order of magnitude resulting in a two orders of magnitude lower quantum efficiency than what was calculated in (4.4) thus explaining the bulk of the discrepancy. A strategy to significantly reduce the surface recombination velocity and increase the quantum efficiency will discussed in the next chapter.

# Chapter 5

# Overcoming non-radiative recombination

In the previous chapter, experimental results of an electrically-injected antenna-LED were presented. Despite reasonably high spontaneous emission enhancement from the antenna, the quantum efficiency was lower than what is desired for a practical device. Bare III–V surfaces are known to have large surface recombination which has placed a severe restriction on the scalability of traditional III–V light emitting devices. This begs the question: Can the nanoscale III–V antenna-LED ever be efficient?

In this chapter, it will be shown that, yes, the III–V antenna-LED can be efficient. Through only a modest antenna enhancement, the spontaneous emission rate can indeed surpass the non-radiative rate. Remarkably, this can be done without specially preparing the surface beyond maintaining the natural surface condition of the active region. However, because of the large surface-to-volume ratio of the antenna-LED, maintaining the surface condition of the active region throughout the fabrication process flow is not trivial. It will be shown that process induced surface damage causes a dramatic increase in the surface recombination velocity and explains the low quantum efficiency of the device reported in the previous chapter. A new method of cleaning and protecting the surface during fabrication has been developed which gives low surface recombination velocity ($< 10^4$ cm/s) and is expected to enable high efficiency operation of the antenna-LED.

## 5.1 Can the nanoscale III–V antenna-LED ever be efficient?

Carriers injected into the antenna-LED have two primary recombination pathways as shown in Figure 5.1. Either the carriers recombine radiatively and emit light, or the carriers recombine non-radiatively at the surface and do not emit light. Other recombination mechanisms are of course present in the antenna-LED but are almost always small enough relative to
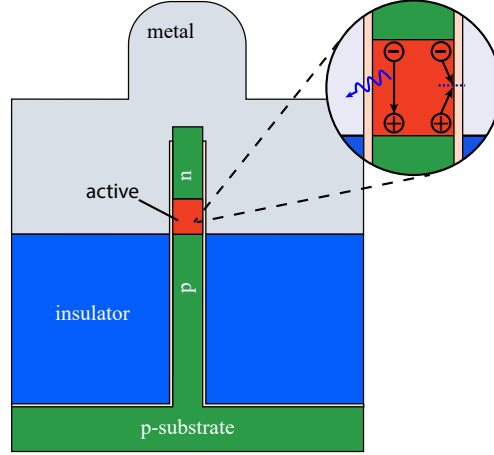
Figure 5.1: Cross-section schematic of the antenna-LED showing a close-up of the dominant radiative and non-radiative surface recombination pathways in the active region.

spontaneous emission and surface recombination to be ignored[1]. The total current in an antenna-LED under forward-bias can be written as a sum of the radiative current ($I_{rad}$) and non-radiative current ($I_{nr}$) [91]

$$I_{total} = I_{nr} + I_{rad} = qV(R_{nr} + R_{rad}) = qV(An + Bnp) \tag{5.1}$$

where $R_{rad}$ and $R_{nr}$ are the radiative and non-radiative recombination rates and $V$ is the active region volume. Under the conditions of non-degenerate carrier population, an expression for $n^2$ is straightforward to derive

$$n^2 = np = n_i^2 e^{qV_f/kT} \tag{5.2}$$

where $n_i$ is the intrinsic carrier concentration. Therefore,

$$n = n_i e^{qV_f/2kT} \tag{5.3}$$

The non-radiative coefficient ($A$) can be written as $A = v_s A_s/V$ where $A_s$ is the surface area of the active region. The radiative coefficient ($B$) can be written as $B = FB_0$ where $F$ is the overall antenna spontaneous emission enhancement factor and $B_0 \approx 10^{-10}$ cm$^6$s$^{-1}$ for most III–V semiconductors. An expression for the non-radiative current and radiative current in the antenna-LED can now be written as

$$I_{nr} = qA_s v_s n_i e^{qV_f/2kT} \tag{5.4}$$

$$I_{rad} = qVFB_0 n_i^2 e^{qV_f/kT} \tag{5.5}$$

---

[1]This is true except at very high carrier density. Auger recombination and other effects related to high carrier density will be considered in detail in Chapter 6

where $A_s$ is the surface area of the active region. Equation (5.4) assumes the non-radiative recombination is uniformly distributed in the active region and thus somewhat overestimates the non-radiative current [92]. Equations (5.4) to (5.5) are sometimes called the $kT$ and $2kT$ currents respectively because of the dependence on the thermal voltage in the denominator of the exponential function. It can be seen that $I_{rad}$ can be made larger than $I_{nr}$ by:

1. Minimizing the surface recombination velocity ($v_s$).

2. Maximizing the injected carrier density (i.e. apply a large forward bias).

3. Maximizing the antenna enhancement ($F$).

4. Minimizing the surface-to-volume ratio ($A_s/V$).

Strategies to meet each of these requirements will be briefly summarized here but, where mentioned, are covered in more detail elsewhere in this dissertation.

## Minimizing the surface recombination velocity ($v_s$)

Table 5.1 summarizes the typical experimentally observed values of $v_s$ for several candidate semiconductors for the antenna-LED [93]–[97] . The measured $v_s$ is sensitive to sample preparation, cleanliness, and measurement technique which has led to a large spread in the reported values; therefore only the order of magnitudes of $v_s$ are shown here.

As mentioned, silicon has low $v_s$ but is not suitable for the antenna-LED given the indirect bandgap. InP has one of the lowest values of $v_s$ but has a large bandgap ($E_g = 1.34$ eV) which limits the choice of compatible waveguide materials that are transparent to light emitted by an InP-based antenna-LED. In particular, silicon photonics has recently become an important platform for on-chip optical communication but silicon photonic waveguides are absorbing for photon energy $\hbar\omega > 1$ eV. GaN, GaAs, and other large bandgap semiconductor materials are also undesirable for this same reason. GaAs also has one of the highest values of $v_s$ of all III–V semiconductors and thus should be completely avoided. Alloys of InP and GaAs, can be tuned to emit light deep into the near-IR and thus compatible with silicon photonic waveguides. Furthermore, the $v_s$ is reasonably low and falls somewhere the value for InP and GaAs.

| Semiconductor | Surface recombination velocity (cm/s) |
|---|---|
| Silicon | $1 - 10$ |
| GaAs | $10^6$ |
| InP | $10^2$ |
| InGaAs(P) | $10^3 - 10^4$ |
| GaN | $10^3 - 10^4$ |

Table 5.1: Typical surface recombination velocity observed for several important semiconductor materials.

There have been many reports of reducing the III–V surface recombination velocity below the values reported in Table 5.1 with solution-based (particularly sulfides) chemical passivation [96]. Longevity and repeatability of solution-based passivation is difficult to obtain without resorting to cladding the III-V surface with a thick oxide [98]. Other approaches to improving III-V surface quality include regrowth of a high-bandgap material [99] or slight wet etching of the III-V surface [93]. Regrowth is challenging given the tendency for a nanoscale structure to minimize surface energy by changing shape during regrowth and timed wet etching is not easily controlled. For these reasons, significant reduction of $v_s$ through traditional means of passivation may not be accessible for the antenna-LED.

## Maximizing the injected carrier density

Because of the dependency on the thermal voltage ($kT/q$) in the exponential function, the radiative current ($I_{rad}$) will increase by a decade for each 60 mV increase in the forward voltage ($V_f$) whereas twice as much increase in $V_f$ is needed to increase the non-radiative current ($_{nr}$) by the same factor. Therefore, operation with a high forward voltage (or equivalently, a high carrier density) is desired. In practice, the upper limit of $V_f$ is approximately the bandgap of the active region material. For $V_f > Eg/q$, the current increases rapidly leading to a number of non-ideal effects such as Auger recombination, carrier overflow into cladding layers, and thermal issues.

Alternatively, the active region can be doped to ensure a high carrier density without requiring a large $V_f$. This will be addressed in Chapter 6

## Maximizing the antenna enhancement and minimizing the surface-to-volume ratio

For a given antenna design, the antenna enhancement ($F$) is maximized by scaling the ridge width as small as possible since $F \propto w^{-2}$. Doing so would also increase the surface-to-volume ratio and therefore it seems at first glance that this conflicts with the requirement of *minimizing* the surface-to-volume ($A_s/V$) ratio. However, $A_s/V \propto w^{-1}$ therefore it is always desirable to scale the ridge width to maximize antenna enhancement[2]. That being said, if two antenna designs have the same antenna enhancement factor but the second design requires a smaller surface-to-volume ratio, the first design should be chosen.

The above requirements can be visualized by plotting $I_{rad}$ and $I_{nr}$ as function of applied voltage bias for several different antenna enhancement factors ($F$) as shown in Figure 5.2 for an antenna-LED with an active region consisting of three 5nm thick InGaAs quantum wells. The ridge dimensions are assumed to be 20 nm wide by 100 nm long. In plotting the non-radiative current ($I_{nr}$) the surface recombination velocity is set to $v_s = 10^4$ cm/s. This choice of $v_s$ is a relatively optimistic value compared to reported $v_s$ values for InGaAs

---

[2]Assuming the contact resistivity does not become too large. This is discussed in Chapter 6

(a)



(b)
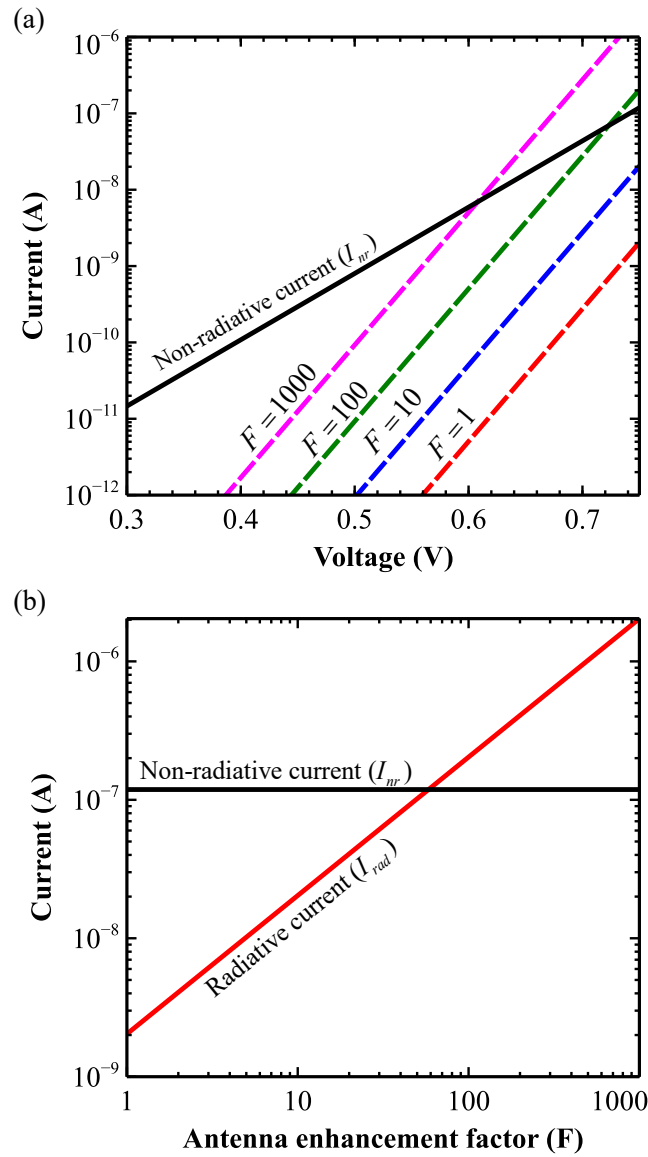
Figure 5.2: (a) The non-radiative current (black) and radiative current (colored) for several different antenna enhancement values plotted as a function of voltage; and (b) non-radiative current (black) and radiative current (red) plotted as a function of antenna enhancement factor with an applied voltage of $E_g/q$.

between $10^4$ and $10^5$ cm/s; this will be justified later. The upper limit of the x-axis is set to correspond to the bandgap of InGaAs, which as discussed earlier sets the upper limit for the forward voltage. The region in which the $I_{rad}$ (colored) curves exceeds the $I_{nr}$ (black) curve in Figure 5.2 can be considered a region in which the antenna-LED is operating efficiently.

It can be seen that without any antenna enhancement ($F = 1$), $I_{rad}$ is unable to compete

with $I_{nr}$ and, not surprisingly, the nanoscale LED without antenna will be inefficient. With increasing antenna enhancement, the $I_{rad}$ curve shifts to the left and $I_{rad}$ will surpass $I_{nr}$ with enough forward bias. This can be more clearly seen by plotting $I_{rad}$ and $I_{nr}$ as a function of antenna enhancement at the maximum allowed forward voltage $V_f = E_g/q$. For a modest enhancement of $F \geq 60$, the $I_{rad}$ exceeds $I_{nr}$ and the antenna-LED will operate efficiently. Based on this analysis, it is concluded that efficient operation of the III–V antenna-LED is indeed possible.

## 5.2 Measurement of surface recombination velocity

Following [100], the surface recombination is written as

$$R_{surf} = \left(\frac{A_s}{V}\right) \frac{np - n_i^2}{\frac{n}{v_h} + \frac{p}{v_e}} \tag{5.6}$$

where $A_s$ is the active region surface area, $V$ is the active region volume, $v_h$ is the capture velocity of the hole at the surface, and $v_e$ is the capture velocity of the electron at the surface. Under the strong injection regime $np \gg n_i^2$ and 5.6 is reduced to

$$R_{surf} = \frac{A_s}{V} v_s n \tag{5.7}$$

where $v_s$ is called the surface recombination velocity and is equal to $v_s^{-1} = v_h^{-1} + v_e^{-1}$. For a semiconductor ridge of width $w$ and length $L$, the surface-to-volume ratio is written $A_s/V = 2/w + 2/L$ which for $L \gg w$ simplifies to $A_s/v \approx 2/w$ and therefore

$$R_{surf} \approx 2 v_s w^{-1} n \tag{5.8}$$

Finally, the non-radiative lifetime from surface recombination is then given by

$$\tau_{surf}^{-1} = \frac{R_{surf}}{n} = 2 v_s w^{-1} \tag{5.9}$$

For sub-micron widths, the overall lifetime ($\tau$) is dominated by $\tau_{surf}$ and thus $\tau_{surf} \approx \tau$ for typical $v_s$ values $\approx 10^4$ cm/s. Therefore, $v_s$ can simply be extracted from the linear slope of $\tau^{-1}$ plotted as a function of $w^{-1}$.

For all measurements in this Chapter, test samples consisting of arrays of ridges with varying widths were used for extraction of $v_s$. The active region of the test ridges consisted of three InGaAs quantum wells cladded by InGaAsP/InP (more details of this structure can be found in the previous chapter). Measurement of the overall lifetime ($\tau$) from the semiconductor ridges was performed with time-resolved photoluminescence (TRPL). Because the recombination was dominated by the non-radiative pathways, the lifetime is independent of carrier density and therefore the decay was well represented by a single exponential fit.

# 5.3 Characterization of process induced surface damage

As discussed in the previous section, high efficiency operation of the antenna-LED can be achieved with the "natural" surface recombination velocity of the bare InGaAs active region surface ($v_s \approx 10^4$ cm/s). Any reduction in the surface recombination velocity through passivation is of course ideal, but not necessary. However, it is necessary to achieve and maintain this surface recombination velocity through the entire fabrication process described in Chapter 4. Several critical processing steps in which the active region surface is possibly subject to surface damage have been identified:

1. **Dry etching of ridges**: The InGaAs active region is exposed to a high density ICP-RIE plasma. It is well-known that dry etching of III–V materials can introduce defects at the surface which may increase the surface recombination velocity beyond the "natural" surface recombination velocity of the bare InGaAs surface.

2. **Digital etching of ridges**: The ridge is oxidized with direct exposure to $O_2$ plasma an then dipped in acid to remove the oxide. This is repeated several times to slowly reduce the width. Damage to the surface is possible with physical sputtering or incorporation of oxygen.

3. **$O_2$ descum**: $O_2$ plasma is used to clean and remove organic residue after several process steps. During these steps, only a thin ($< 5$ nm) $Al_2O_3$ protects the surface from direct exposure to plasma.

The surface recombination velocity after each of these steps was measured to characterize the extent of surface damage.

## Surface recombination velocity after dry etching

The surface recombination velocity was measured for three different samples after dry etching with $Ar/H_2/CH_4/Cl_2$ gas in an ICP/RIE chamber with 490 W of ICP power and 100 W of forward power (Figure 5.3a-b). Plotted in Figure 5.3 is the plot of inverse lifetime ($\tau^{-1}$) as a function of inverse width of the semiconductor ridge ($w^{-1}$) for the three different samples. The extracted surface recombination velocity varied between $1.2 \times 10^4$ cm/s for the sample and $6.1 \times 10^4$ cm/s for the worst sample with an average of $2.0 \times 10^4$ cm/s for all samples combined. These surface recombination velocities are within the range reported by others therefore it is concluded that dry etching is not significantly damaging the active region surface (at least beyond what is typically observed). Nonetheless, the large range of surface recombination velocity indicates a run-to-run variation which is not well-controlled. The best sample (blue curve in Figure 5.3c) is suitable for processing into antenna-LED devices whereas the worst sample (red curve in Figure 5.3c) is probably not suitable. A strategy to reduce the variability will be discussed later.
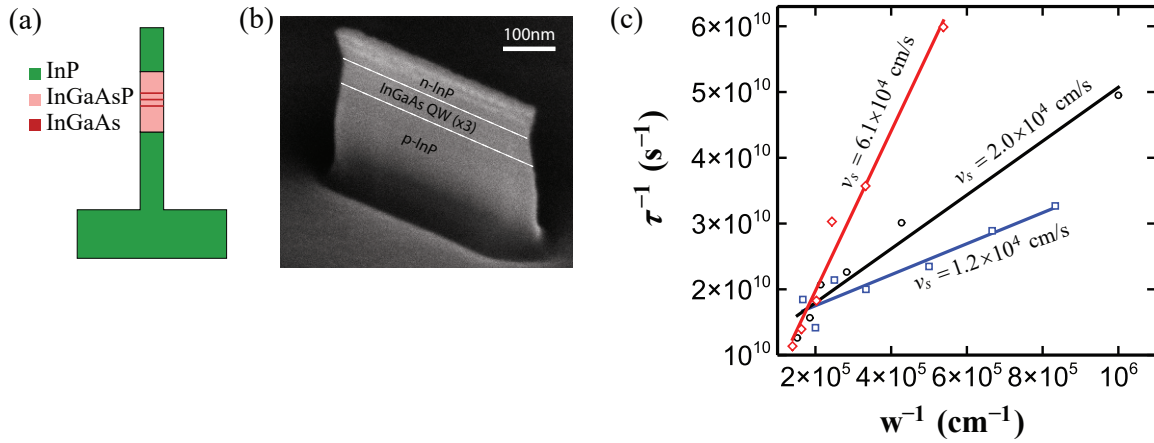
Figure 5.3: (a) Drawing of the multiple quantum well test ridge after dry etch; (b) SEM image of the dry etched ridge; and (c) plot of the inverse decay time $\tau^{-1}$ as a function of $w^{-1}$ for three different dry etch runs.

## Surface recombination velocity after digital etching
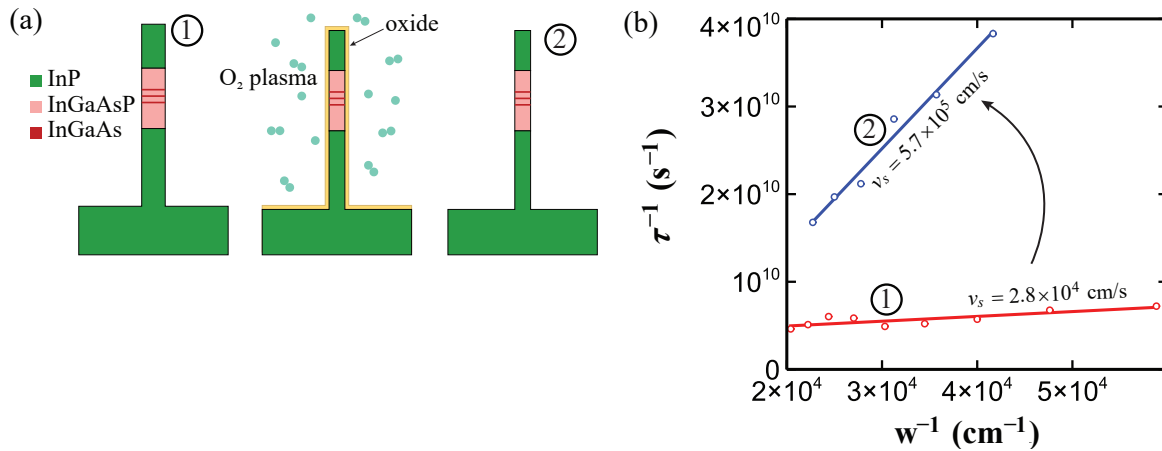


Figure 5.4: (a) Schematic of the digital etch process flow; and (b) plot of the inverse decay time $\tau^{-1}$ as a function of $w^{-1}$ for ridges before and after a single digital etch cycle.

A fresh sample was prepared by first dry etching ridges (Figure 5.4a). After dry etching, the surface recombination velocity was measured to be $2.8 \times 10^4$ cm/s. Next, the ridges were exposed to an $O_2$ plasma in a parallel plate etcher at 100 W of forward power for 2 minutes to oxidize $\approx 2$ nm of the ridge surface. The oxide was removed with a 30 s dip in $H_2SO_4$ acid. After one cycle of digital etching, the surface recombination velocity increased dramatically by more than an order of magnitude to $5.7 \times 10^5$ cm/s (Figure 5.4b). Clearly, the digital etch process has significantly damaged the surface. The digital etch process described here

has been used by others without any report of damage to the III–V surface. The discrepancy between those results in the data reported here is not understood but may be related to the nature of the plasma exposure to the sample (forward power, time, etc.).

## Surface recombination velocity after $O_2$ descum
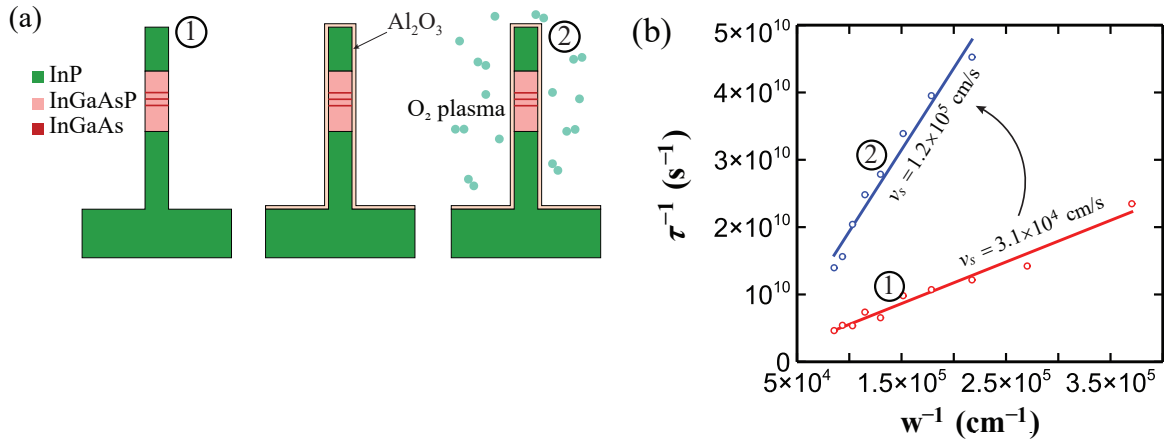


Figure 5.5: (a) Schematic of the $O_2$ descum process flow; and (b) plot of the inverse decay time $\tau^{-1}$ as a function of $w^{-1}$ for ridges before and after $O_2$ descum.

Freshly prepared samples were again dry etched and had a measured surface recombination velocity of $3.1 \times 10^4$ cm/s. After dry etching, a thin 1 nm of $Al_2O_3$ was deposited using atomic layer deposition. The sample was then exposed to an $O_2$ plasma for 2 min at 100 W of forward power to emulate a $O_2$ descum (Figure 5.5a). The surface recombination velocity was observed to again increase dramatically to $1.2 \times 10^5$ cm/s. The very thin $Al_2O_3$ is evidently not able to protect the active region surface from damage by the $O_2$ plasma (Figure 5.5b).

## 5.4 Improved process without process induced surface damage

The results in the previous section demonstrate that the surface recombination velocity is reasonably low ($1 - 6 \times 10^4$ cm/s) after dry etching but is dramatically increased by greater than an order of magnitude while processing the ridge into an antenna-LED. This dramatic increase in the surface recombination velocity can explain the low quantum efficiency reported for the antenna-LED device reported in the previous chapter.

Clearly, an improved fabrication process is needed to protect the surface of the active region. In this section it will be shown that a high-quality InGaAs surface can be achieved
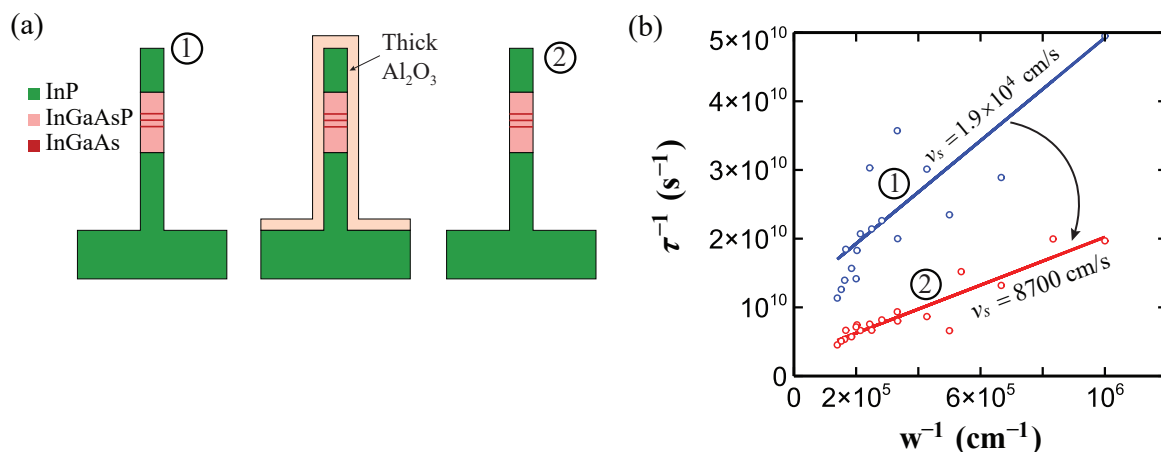
Figure 5.6: (a) Schematic drawings showing deposition and removal of sacrificial $Al_2O_3$; and (b) plot of the inverse decay time $\tau^{-1}$ as a function of $w^{-1}$ for ridges before and after removal of sacrificial $Al_2O_3$.

through the use of a "thick" 15 nm sacrificial $Al_2O_3$ layer deposited by ALD. $Al_2O_3$ was found to protect the active region surface during device processing. Remarkably, upon removal of the sacrificial $Al_2O_3$, a reduction of the surface recombination velocity to $< 9000$ cm/s is observed suggesting a cleaning effect of the sacrificial $Al_2O_3$.

## Cleaning effect of sacrificial $Al_2O_3$

First, the cleaning effect of the sacrificial $Al_2O_3$ is shown. Ridges were dry etched and found to have a surface recombination velocity of $1.9 \times 10^4$ cm/s. Next, 15 nm of $Al_2O_3$ was deposited at 270°C using ALD. The $Al_2O_3$ was then stripped off using either TMAH (3% in commercial developer) or buffered oxide etch (1:10) as shown in Figure 5.6a. A significant decrease in the surface recombination velocity to 8700 cm/s was observed as shown in Figure 5.6b. The data in Figure 5.6b is composed of multiple samples from several different runs showing the repeatability of this process. The origin of the reduction of the surface recombination velocity is not known. On a separate sample, the deposition and stripping of $Al_2O_3$ was repeated several times. A slight reduction in ridge width was observed suggesting this procedure could be removing dry etch damage or surface contamination and thus leaving behind a cleaner surface. The low surface recombination velocity was found to be stable for at least 3 days when the sample was stored in a nitrogen purged container.

## Protecting active region with sacrificial $Al_2O_3$

On a separate fresh sample, the robustness of the sacrificial $Al_2O_3$ was determined by running a short-loop of the entire fabrication flow of the antenna-LED as shown in Table 5.4. After each step, the surface recombination velocity was measured and plotted in Figure 5.7. After
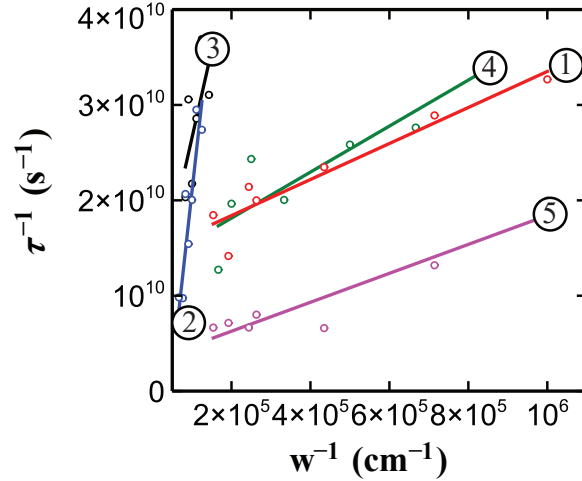
Figure 5.7: Plot of the inverse decay time $\tau^{-1}$ as a function of $w^{-1}$ for ridges throughout the antenna-LED process. The circled numbers correspond to a process step listed in Table 5.4

| Curve | Process step | $v_s$ (cm/s) |
|:---:|---|:---:|
| 1 | Dry etch | $1.0 \times 10^4$ |
| 2 | Deposit sacrificial $Al_2O_3$ | $1.9 \times 10^5$ |
| 3 | 1 hr. bake at 350C | $9.2 \times 10^4$ |
| 4 | Expose sample to $SF_6$/He plasma (100W, 3min.) | $1.2 \times 10^4$ |
| 5 | Remove sacrificial $Al_2O_3$ (TMAH or BOE) | $7.6 \times 10^3$ |

Table 5.2: Measured surface recombination velocity ($v_s$) after each process step. The curve number refers to the curve plotted in Figure 5.7

dry etching of the ridges and deposition of the sacrificial $Al_2O_3$, the surface recombination velocity was measured at $1.0 \times 10^4$ cm/s and $1.9 \times 10^5$ cm/s respectively. The $Al_2O_3$ large increase after deposition is possibly due to the presence of fixed charge in the $Al_2O_3$ which may cause deleterious band bending at the surface of the ridge [101]. It was observed (not shown here) that the surface recombination increased with the thickness of the sacrificial $Al_2O_3$ layer. The surface recombination velocity remained stable after a long bake in an ambient environment suggesting the $Al_2O_3$ serves as a good barrier against oxygen penetration. Interestingly, the $Al_2O_3$ recovered after exposing the sample to a SF6/He plasma. Passivation of traps through fluorination of $Al_2O_3$ has been reported and may explain the results here [102]. Finally, the sacrificial $Al_2O_3$ was then stripped off revealing a low surface recombination velocity of 7600 cm/s for this sample. Despite the large variation of surface recombination velocity throughout the process, an overall reduction of the surface recombination velocity was observed at the end of the process. Therefore, the sacrificial $Al_2O_3$ both protected and cleaned the surface.

Summarizing the results, a method to protect and clean the active region surface using a sacrificial $Al_2O_3$ was shown. The process resulted in an ultra-clean InGaAs surface with surface recombination velocity $< 10^4$ cm/s. With minimal antenna-enhancement, high efficiency operation of the antenna-LED is feasible.

# Chapter 6

# Toward 100 GHz direct modulation rate at high efficiency

In this chapter, a model to predict the small-frequency response and efficiency of the antenna-LED is derived. Using this model it is shown that greater than 100 GHz direct modulation rate at high efficiency is possible with an optimized device.

## 6.1 Recombination pathways in the antenna-LED

Following the approach used in [100], it is useful to consider a simple carrier reservoir model for the active region to visualize the flow of carriers in the antenna-LED as shown in Figure 6.1. Under forward-bias, carriers are injected into the carrier reservoir with a rate equal to $\eta_{inj}J/qd$ where $d$ is the active region thickness and $\eta_{inj}$ is the carrier injection efficiency (the physical mechanism for $\eta_{inj} < 1$ will be discussed in detail later). In an attempt to maintain equilibrium, the carriers will then recombine or otherwise leave the carrier reservoir via various radiative and non-radiative mechanisms. Radiative recombination ($\eta_{ant}R_{rad}$) through electron-hole recombination and emission of light by the antenna is of course the desired recombination mechanism in the antenna-LED. Because of resistive loss in the antenna metal, the overall radiative recombination is reduced by the antenna efficiency ($\eta_{ant}$).

There are many possible non-radiative pathways for carriers to leave the carrier reservoir. Loss in the antenna metal can be considered a non-radiative recombination whose rate is given by $(1 - \eta_{ant})R_{rad}$. Other important non-radiative pathways that are considered are surface recombination ($R_{surf}$) and Auger recombination ($R_{auger}$). Surface recombination can be very high in the antenna-LED because of the large surface-to-volume ratio of the device. Auger recombination is known to be an issue in III–V materials at high carrier densities. Both will be discussed in more detail later. For brevity in this section, they are lumped into a single non-radiative rate of $R_{nr}$.

The ratio of the radiative rate to the total rate of all recombination events is called the
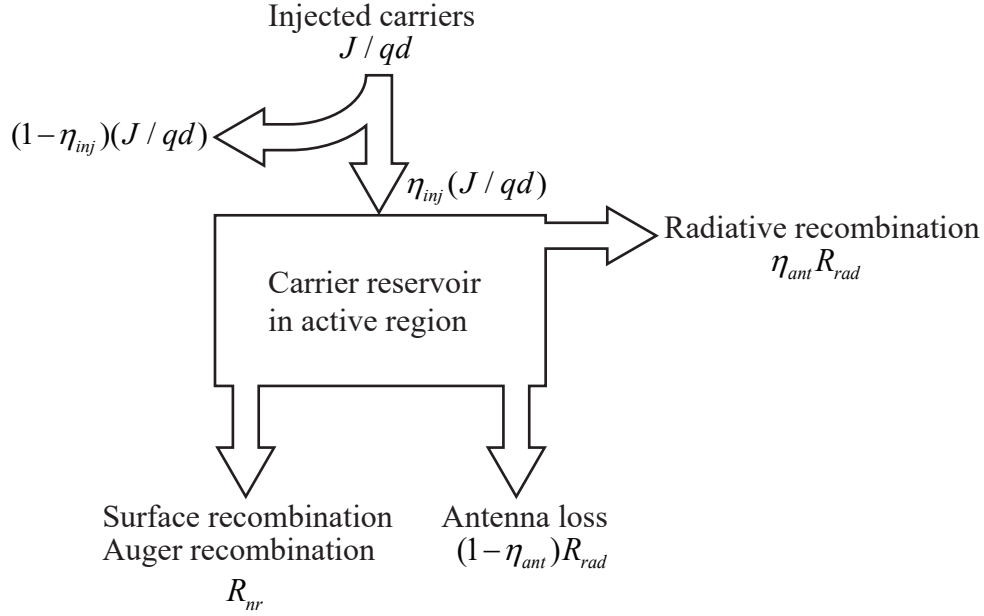
Figure 6.1: Carrier reservoir model for visualizing carrier flow in the antenna-LED

internal quantum efficiency and is given by

$$\eta_{IQE} = \frac{\eta_{ant} R_{rad}}{\eta_{ant} R_{rad} + (1 - \eta_{ant}) R_{rad} + R_{nr}}. \tag{6.1}$$

The ratio of the radiative rate to the total injection rate of carriers into the device will be referred to here as the quantum efficiency and is given by

$$\eta_{QE} = \frac{\eta_{ant} R_{rad}}{J/qd}. \tag{6.2}$$

## 6.2   Rate equation analysis

Under a static (DC) forward-bias condition the rate of carriers leaving the carrier reservoir will precisely equal the rate of carriers entering the carrier reservoir thus leading to a quasi-equilibrium. The same will be true if the forward-bias is slowly changed. As the rate of change of forward-bias is slowly increased, there will be some point at which the carriers in the reservoir will not be able to respond fast enough to maintain this quasi-equilibrium. The rate of forward-bias change at which this occurs effectively defines the upper limit to the direct modulation speed of the antenna-LED.

Rate equation analysis can be used to model the dynamic behavior of the antenna-LED to determine the maximum modulation speed. This is done by first writing an expression

for the rate of change of electrons as

$$\frac{dn}{dt} = \eta_{inj}\frac{J}{qd} - R_{rad} - R_{nr}. \tag{6.3}$$

Unlike the laser, the quality factor of the antenna-LED is low such that coupling between the emitted photons and carrier density (i.e. stimulated emission) can be safely ignored. Therefore an expression for the power emitted by the antenna-LED can be directly written as

$$P = \hbar\omega R_{rad}V \tag{6.4}$$

where $V$ is the total injected current into the device, and $\hbar\omega$ is the energy of the photon at the peak emission wavelength. Strictly speaking, $R_{rad}$ should be replaced by the integration of the spontaneous emission spectrum to represent the broad emission spectrum of the antenna-LED. This will be the approach when the results of the analysis are shown later in the Chapter. However, (6.4) is retained without loss of generality.

Next, small-signal analysis is applied by supposing a small modulation is applied to the current density and analyzing the corresponding modulation in the power emitted from the antenna-LED. This is done by assuming the following form for the current density, carrier density, and power

$$\begin{aligned} J(t) &= J_0 + \Delta J(t) \\ n(t) &= n_0 + \Delta n(t) \\ P(t) &= P_0 + \Delta P(t) \end{aligned} \tag{6.5}$$

where the first term in each expression corresponds to an average value with the second term representing a small-signal modulation about the average value. Plugging (6.5) into (6.3) gives

$$\frac{d\Delta n}{dt} = \eta_{inj}\frac{\Delta J}{qd} - \Delta n\left.\frac{d\Delta R_{rad}}{dn}\right|_{n=n_0} - \Delta n\left.\frac{d\Delta R_{nr}}{dn}\right|_{n=n_0} \tag{6.6}$$

$$\Delta P = V\hbar\omega\Delta n\left.\frac{dR_{rad}}{dn}\right|_{n=n_0} \tag{6.7}$$

where a Taylor expansion was used to linearize $R_{rad}$ and $R_{nr}$ about a carrier density of $n = n_0$. The small-signal modulation about the average value is then assumed to be AC in nature such that

$$\begin{aligned} \Delta J(t) &= \Delta J(\omega)e^{j\omega t} \\ \Delta n(t) &= \Delta n(\omega)e^{j\omega t} \\ \Delta P(t) &= \Delta P(\omega)e^{j\omega t} \end{aligned} \tag{6.8}$$

where phasor notation is used. Equation (6.8) is then be inserted into (6.6) and solved for the complex amplitude $\Delta n(\omega)$

$$\Delta n = \eta_i \frac{\Delta J}{qd} \left( \frac{dR_{rad}}{dn} \bigg|_{n=n_0} + j\omega \right)^{-1} \tag{6.9}$$

Finally, (6.9) is inserted into (6.7) and after some rearranging a complicated yet complete form for the transfer function $\Delta P / \Delta J$ can be written as

$$\frac{\Delta P}{\Delta J} = \frac{\eta_i V \hbar \omega}{qd} \frac{\frac{dR_{rad}}{dn}\big|_{n=n_0}}{\frac{dR_{rad}}{dn}\big|_{n=n_0} + \frac{dR_{nr}}{dn}\big|_{n=n_0}} \frac{1}{\left( \frac{dR_{rad}}{dn}\big|_{n=n_0} + \frac{dR_{nr}}{dn}\big|_{n=n_0} \right)^{-1} + j\omega} \tag{6.10}$$

It can be immediately seen that (6.10) is written in the form of a single-pole transfer function whose 3dB-frequency is given by

$$f_{3dB} = \frac{1}{2\pi} \left( \frac{dR_{rad}}{dn} \bigg|_{n=n_0} + \frac{dR_{nr}}{dn} \bigg|_{n=n_0} \right). \tag{6.11}$$

Therefore, at a given bias point, the antenna-LED will be fast when a small increase in the carrier density leads to a large rate of change of the radiative rate or non-radiative rate. With the general expression for the 3dB frequency now derived we are ready to calculate the radiative ($R_{rad}$) and non-radiative ($R_{nr}$) rate.

## 6.3 Radiative recombination in the antenna-LED

### Antenna-enhanced transition matrix element

The radiative transition rate for a band-to-band transition in the active region of the antenna-LED is given by Fermi's Golden Rule. As described in Chapter 2, the transition rate is proportional to the transition matrix element $|H_{fi}|^2$. The transition matrix element in a semiconductor describes the strength of the interaction between the vacuum-field and electron-hole pair. The antenna acts on the semiconductor by effectively increasing $|H_{fi}|^2$ and thus enhancing the transition rate.

The spontaneous emission rate enhancement ($F(\omega)$) from an antenna can be approximated by a Lorentzian function

$$F(\omega) = F_{peak} \frac{(\omega_0/2Q)^2}{(\omega - \omega_0)^2 + (\omega_0/2Q)^2} \tag{6.12}$$

where

$$F_{peak} = \text{peak enhancement factor at } \omega = \omega_0$$
$$\omega_0 = \text{antenna resonance frequency}$$
$$Q = \text{quality factor of antenna resonance}$$

and $F(\omega)$ is evaluated at the center of the antenna hotspot where the spontaneous emission enhancement is largest. Generally speaking, the entire active region will not observe an enhancement factor equal to $F(\omega)$ everywhere. Most antennas have some polarization preference therefore not all dipoles in the semiconductor will be equally enhanced by the antenna, if at all. Even without antenna enhancement, the interaction between the vacuum-field and electron-hole transition can be polarization dependent. This may be used to our advantage if the antenna polarization is aligned with the orientation of the dominant dipole transition. $F(\omega)$ may be position-dependent and only a fraction of the active region volume may overlap with the antenna mode.

The polarization and volume effects are taken into by defining an effective antenna-enhancement $(F_{eff}(\omega))$ which is calculated by averaging $F(\omega)$ over all dipole orientations and multiplying by a volume factor $\Gamma_V = V^{-1} \int_V F(\omega, x, y, z)dV$ where $V$ is the active region volume. The effective enhancement can then be multiplied by the transition matrix element and the spontaneous emission spectrum derived in the usual manner.

In this chapter, the analysis will be restricted to the cavity-backed slot antenna but a similar analysis can be applied for other antenna structures. The cavity-backed slot antenna is linearly polarizing and will only enhance dipoles that have orientation transverse to the long axis of the slot. The position-dependent enhancement is well-described by $F(\omega)\cos^2\left(\frac{\pi z}{L}\right)$ from $x = -L/2$ to $x = L/2$ where $L$ is the slot length. Ignoring the dependency of the antenna enhancement in the y or z-direction, the volume factor of the cavity-backed slot antenna is then given simply by $\Gamma_V = \frac{1}{2}$

The effective antenna-enhancement $(F_{eff}(\omega))$ will now be derived for an antenna-LED consisting of a bulk active region or quantum well active region.

**Bulk active region**
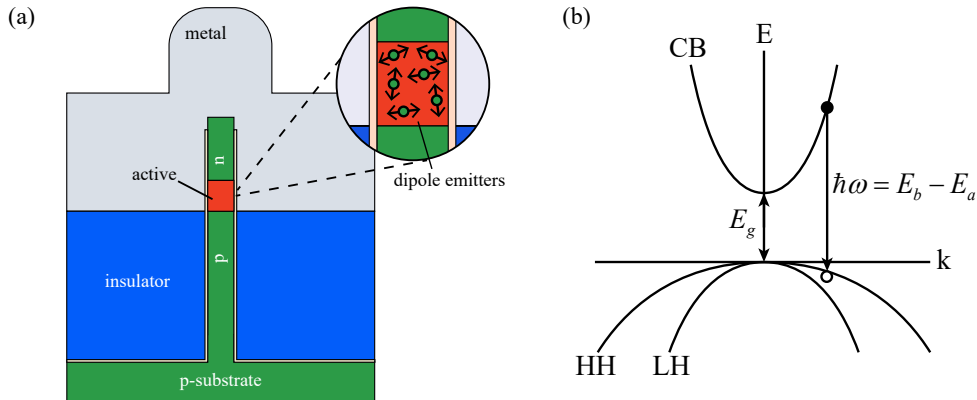


Figure 6.2: (a) Antenna-LED with bulk active region; and (b) simplified $E$ vs. $k$ diagram

Consider the antenna-LED with bulk active region coupled to cavity-backed slot antenna. Emission in a bulk semiconductor is isotropic as illustrated in Figure 6.2a therefore the an-

tenna will enhance only one of the three dipole orientations. The strength of transitions
between the conduction band and heavy hole or light hole bands (Figure 6.2b) can be de-
scribed by the matrix element $|H_{fi}|^2$. If we define $|H_{fi,0}|^2$ as the un-enhanced bulk matrix
element then the averaged matrix element ($|\bar{H}_{fi}|$) for transitions between the conduction
band and heavy/light hole bands in a bulk semiconductor enhanced by a cavity-backed slot
antenna is

$$
\begin{aligned}
\left|\bar{H}_{fi}\right| &= \frac{1}{3}\left(\Gamma_V F(\omega)\left|H_{fi,0}\right|^2 + \left|H_{fi,0}\right|^2 + \left|H_{fi,0}\right|^2\right) \\
&= \frac{\left|H_{fi,0}\right|^2}{3}\left(\frac{1}{2}F(\omega) + 2\right) \\
&\approx \frac{\left|H_{fi,0}\right|^2}{6}F(\omega) \rightarrow F_{eff}(\omega) = \frac{F(\omega)}{6}
\end{aligned}
\tag{6.13}
$$

where the approximation holds if $F(\omega) \gg 1$. The effect of dipole averaging and spatial
dependence on the antenna mode is a significant reduction of the peak antenna enhancement
by a factor of six.

**Quantum well active region**
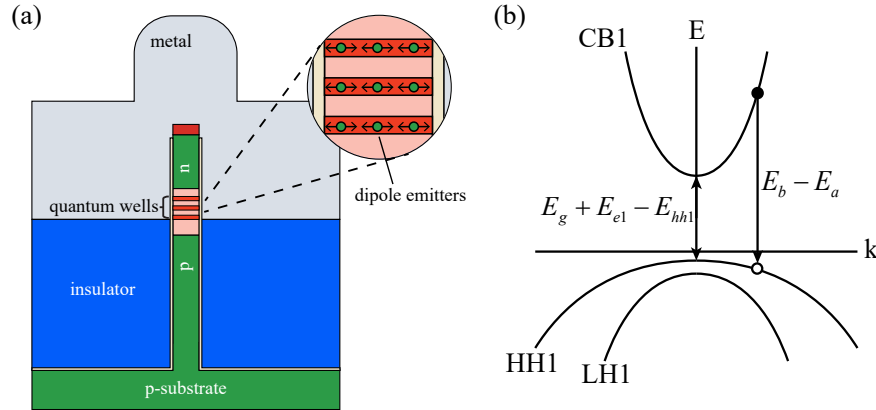


Figure 6.3: (a) Antenna-LED with quantum well active region; and (b) simplified $E$ vs. $k$
diagram. Only the first conduction and valence sub-bands are shown.

The effect of dipole averaging is reduced by using a quantum well instead of a bulk
active region. As schematically shown in Figure 6.3, the dipole orientation is restricted to
be oriented along either the $\hat{x}$ or $\hat{z}$ directions for the conduction subband to heavy hole band
transition in quantum well. The averaged matrix element for the conduction band to heavy

hole transition can be written

$$\text{(CB-HH)} \ |\bar{H}_{fi}| = \frac{1}{3}\left(\frac{3}{2}\Gamma_V F(\omega)|H_{fi,0}|^2 + \frac{3}{2}|H_{fi,0}|^2\right)$$

$$= \frac{|H_{fi,0}|^2}{3}\left(\frac{3}{4}F(\omega) + \frac{3}{2}\right)$$

$$\approx \frac{|H_{fi,0}|^2}{4}F(\omega) \to F_{eff}(\omega) = \frac{F(\omega)}{4} \tag{6.14}$$

an improvement of a factor of $\frac{3}{2}$ compared with the bulk active region. For high carrier density, a significant fraction of holes may occupy the first light hole subband (LH1) and therefore transitions between the CB1 and LH1 bands may become non-negligible. The averaged matrix element for the CB-LH bands for the antenna-LED is written

$$\text{(CB-LH)} \ |\bar{H}_{fi}| = \frac{1}{3}\left(\frac{1}{2}\Gamma_V(\omega)|H_{fi,0}|^2 + \frac{1}{2}|H_{fi,0}|^2 + 2|H_{fi,0}|^2\right)$$

$$= \frac{|H_{fi,0}|^2}{3}\left(\frac{1}{4}F(\omega) + \frac{5}{2}\right)$$

$$\approx \frac{|H_{fi,0}|^2}{12}F(\omega) \to F_{eff}(\omega) = \frac{F(\omega)}{12} \tag{6.15}$$

Thus the averaged matrix element is four times weaker for the CB-LH transition compared with the CB-HH transition.

For narrow ridges ($< 20$ nm) it is desirable to have thin quantum wells to ensure that quantum confinement along the $\hat{x}$ direction does not become significant such that ridge appears more like a quantum well wire with 1D-like density of states. [103]. A quantum well wire is not a desirable active region since the light-emitter interaction in the polarization of the antenna mode is reduced. The quantum well thickness needs to be less than half the width of the ridge to ensure the active region remains quantum well-like [100], [104].

The above results have been summarized in Table 6.1.

| Active region | Transition | $\hat{x}$ | $\hat{y}$ | $\hat{z}$ | $F_{eff}(\omega)$ |
|---|---|---|---|---|---|
| Bulk | CB-HH / CB-LH | $\frac{1}{2}F(\omega)$ | 1 | 1 | $\frac{1}{6}F(\omega)$ |
| Quantum well | CB-HH | $\frac{3}{4}F(\omega)$ | $\frac{3}{2}$ | 0 | $\frac{1}{4}F(\omega)$ |
| | CB-LH | $\frac{1}{4}F(\omega)$ | $\frac{1}{2}$ | 2 | $\frac{1}{12}F(\omega)$ |

Table 6.1: Summary of the effective antenna enhancement ($F_{eff}$) for bulk and quantum well antenna-LED. $F(\omega)$ is the antenna enhancement for dipole aligned parallel with antenna mode. $F_{eff}$ is the overall enhancement which full takes into account volume averaging and dipole averaging

## Quantum dot active region

An active region composed of a few quantum dots could be an interesting option for the antenna-LED. The atomic-like density of states could provide efficient enhancement when coupled to the broadband optical antenna resonance.

For a cubic quantum dot, the dipole transition strength will again be isotropic as was the case for the bulk active region; suggesting that no advantage is gained moving to the quantum dot in this respect [60]. In practice, quantum dots are somewhat immune to generalization because the energy levels and wavefunctions are strongly dependent upon the shape of the quantum dot which can vary between materials systems.

The most popular and successful method of creating quantum dots are self-assembled through the Stranski-Krastanow growth method. Quantum dots grown in this manner are randomly deposited on the substrate surface with dot densities of $\approx 10^{11}$ $cm^{-2}$ [105]. An antenna-LED with an active region consisting of randomly deposited Stranski-Krastanow grown dots would be composed of an average of $\approx 10$ quantum dots. Ideally, a single quantum dot would be placed deterministically in the center of the antenna hotspot. This is not currently possible with self-assembled Stranski-Krastanow and would require top-down fabrication with a complicated process including regrowth [106], [107].

An undertaking of the emission properties of an quantum dot antenna-LED is beyond the scope of this dissertation but is an area worthy of future study.

## Spontaneous emission rate ($R_{rad}$)

The spontaneous emission spectrum $(\mathrm{cm^{-3}eV^{-1}s^{-1}})$ for the antenna-LED can now be written in the usual manner [100] except now multiplied the by effective antenna enhancement $(F_{eff}(\hbar\omega))$ such that

$$r^{spon}(\hbar\omega) = \frac{4n\pi q^2}{\epsilon_0 h^2 c^3 m_0 2}\hbar\omega \sum_{hh,lh} F_{eff}(\hbar\omega)|M_T(E_{21})|^2 \rho_r(E_{21})f_2(1-f_1) \tag{6.16}$$

where

$$f_2 = \text{probability for state in conduction band to be occupied}$$
$$f_1 = \text{probability for state in valence band to be occupied}$$
$$\rho_r = \text{reduced density of states}$$
$$\sum_{hh,lh} = \text{summation over heavy hole and light hole bands.}$$

The total radiative rate ($R_{rad}$) from spontaneous emission is then

$$R_{rad} = \int r^{spon}(E_{21})dE_{21} \tag{6.17}$$

which is used in (6.11) to derive the 3db-frequency. The radiative rate should not be confused with the radiation resistance although the same variable is used for both.

## 6.4 Non-radiative recombination in the antenna-LED

### Surface recombination ($R_{nr}$)

Non-radiative recombination at the surface of the exposed active region is the dominant non-radiative recombination in the antenna-LED for all but the highest carrier densities. The non-radiative rate from surface recombination ($R_{nr}$) was discussed in Chapter 5 and found to be

$$R_{nr} = v_s \frac{A_s}{V} \approx v_s \frac{2}{w} \tag{6.18}$$

where

$$v_s = \text{surface recombination velocity} \tag{6.19}$$
$$A_s = \text{surface area of exposed active region} \tag{6.20}$$
$$w = \text{width of active region (i.e. slot width)} \tag{6.21}$$

and the approximation holds for $w \gg L$ where $L$ is the ridge length.

### Auger recombination ($R_{auger}$)

Instead of emitting light, it is possible for an electron-hole recombination to conserve energy by exciting another carrier in the conduction or valence band. The excited carrier will then eventually relax to the band edge and in the process heat the lattice. This is known as Auger recombination. It can be shown that Auger recombination rate is $\propto e^{-E_g/kT}$ and therefore can be an important non-radiative recombination mechanism for semiconductors with small bandgap such as InGaAs [108], [109].

The total Auger rate ($R_{auger}$) for the III–V semiconductor is given by

$$R_{auger} = C_n n^2 p + C_p n p^2 \tag{6.22}$$

$C_n$ is the rate coefficient associated with the recombination of an electron and hole resulting in another electron in the conduction band. Similarly, $C_p$ is is the rate coefficient associated with the recombination of an electron and hole resulting in an excitation of a heavy hole to the split-off or light hole band. Although theoretical calculations for $C_n$ and $C_p$ are possible they tend to be accurate within at best an order of magnitude. Experimental measurements of the individual Auger coefficients is difficult an instead usually a lumped Auger coefficient ($C_A$) is measured that takes into account all Auger-related transitions. Thus, as a simplification, it is assumed here that $C_A = C_n = C_p$.

### Ohmic loss ($J_{ohmic}$)

Some energy that is coupled into the antenna from an electron-hole recombination may get lost as heat instead of light as a result of Ohmic loss in the metal. The device current that

contributes to the Ohmic loss can be written

$$J_{ohmic} = (1 - \eta_{ant})R_{rad}qd \tag{6.23}$$

where $\eta_{ant}$ is the antenna efficiency and $d$ is the active region thickness.

# 6.5  Carrier leakage at high current density

At high current density, the electron density may become so high that carriers can spill out of the active region. These electrons may then recombine elsewhere or become collected at the contact and therefore will become lost and not contribute to the radiative recombination. This results in an effective leakage current flow that bypasses the active region resulting in a decreased injection efficiency. In principle, the same spill out of holes can occur in the valence band. In practice, the density of states is so high that the quasi-Fermi level does not sufficiently get close to the valence band edge for hole leakage to become significant. Therefore, it is suitable to only consider the electrons when modeling the leakage current.

In this section, a model for the leakage current is derived for the case of the antenna-LED with quantum well active region (the analysis is easily extended to include the double heterostructure bulk active region). Central to the models that follow, the quasi-Fermi level is assumed to be the same everywhere in the active region; in other words, all carriers are in equilibrium with each other. This is a reasonable assumption so long as the antenna-enhanced spontaneous emission lifetime is much longer than the scattering time of carriers and slower than the capture time of the carriers into the active region. The latter assumption may become questionable for very high antenna enhancements such that $\tau_{rad} < 1$ ps. Finally, the closed-form expressions for the leakage current shown in the section were derived using Boltzmann statistics. Rigorous Fermi statistics was implemented for the modeling results shown later in this chapter.

## Carrier recombination in the cladding region ($J_{sch}$)

Shown in Figure 6.4 is the band diagram of the antenna-LED consisting of a standard separate confinement heterostructure (SCH) active with a single quantum-well. At high carrier density, the quasi-Fermi level in the conduction band will be pushed close to the conduction band edge of the SCH as shown in Figure 6.4. Therefore a non-negligible amount of carriers will be present in the SCH region and are free to recombine through radiative or non-radiative mechanisms; either way recombination in the SCH is undesirable and will contribute to the non-radiative leakage current of the antenna-LED. Non-radiative recombination at the surface will greatly exceed the spontaneous emission rate in the SCH region since the recombination rate is not enhanced by the antenna. Therefore, the recombination rate ($R_{sch}$) in the SCH region can be estimated as

$$R_{sch} = \frac{n_{sch}}{\tau_{sch}} = n_{sch}v_s\frac{A_s}{V} \approx n_{sch}v_s2w^{-1} \tag{6.24}$$
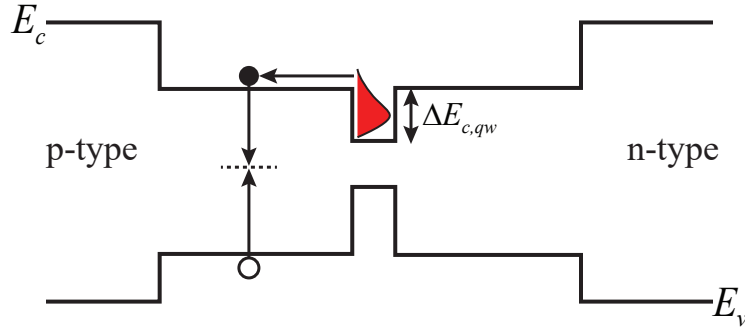
Figure 6.4: Band diagram of a quantum well antenna-LED showing transport of electrons
and holes into the active region.

where $A_s$ and $V$ are the surface area and volume of the SCH region respectively. The carrier
density in the SCH region is given by

$$n_{sch} = N_{c,sch} \exp\left(\frac{F_c - (E_{c,qw} + \Delta E_{c,qw})}{kT}\right) \tag{6.25}$$

where $N_c$ is the effective density of states in the conduction band of the SCH region, $\Delta E_c$ is
the conduction band offset between the quantum well and SCH region and $F_c$ is the quasi-
Fermi level in the conduction band. It is assumed that $F_c$ is flat throughout the quantum
well and SCH region and below the conduction band edge in the SCH region such that the
Boltzmann approximation applies.

The carrier density in the quantum well $(n_{qw})$ is given by

$$n_{qw} = kT\frac{m_e^*}{\pi\hbar^2 L_z}\ln\left(1 + \exp\left[(F_c - E_{e1})/kT\right]\right) \tag{6.26}$$

where $L_z$ is the quantum well thickness and $E_{e1}$ is the energy of the bottom of the first
electron subband. For $F_c \gg E_{e1}$, $F_c$ can be approximated as

$$F_c = \frac{\pi\hbar^2 L_z}{m_e^*}n_{qw} + E_{e1} \tag{6.27}$$

Putting everything together it is now possible to write an expression for $R_{sch}$ in terms of the
carrier density in the quantum well as

$$R_{sch} = \tau_{sch}^{-1} N_{c,sch}\left(\frac{\pi\hbar^2 L_z}{m_e^*}n_{qw}\right)\exp\left(\frac{E_{e1} - E_{c,qw}}{kT}\right)\exp\left(\frac{-\Delta E_c}{kT}\right) \tag{6.28}$$

Finally, the current density associated with the SCH recombination is given by

$$J_{sch} = qd_{sch}R_{sch} \tag{6.29}$$

where $d_{sch}$ is thickness of the SCH region.

Importantly, it is observed that $R_{sch} \propto \exp\left(\frac{-\Delta E_c}{kT}\right)$ therefore it is desirable to have a large conduction band offset between the quantum well and SCH region to minimize the recombination in the SCH region. At high carrier injection, the quasi-Fermi level will push close to the conduction bandedge in the SCH region and therefore $n_{sch}$ in (6.25) will have to be written in terms of the Fermi-Dirac integral. Because of the large surface recombination velocity in the SCH region ($v_s \approx 10^4$ cm/s) and the large volume of the SCH region with respect to the active region, $J_{sch}$ can be a significant fraction of the injected carrier density.

## Carrier overflow $(J_{of})$
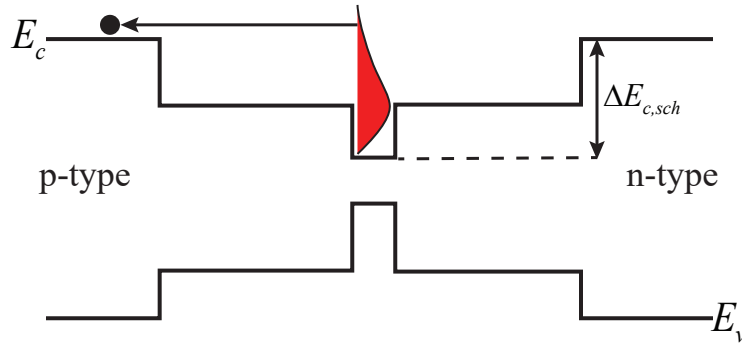


Figure 6.5: Band diagram of a quantum well antenna-LED showing transport of electrons and holes into the active region.

At very high carrier density, some carriers may have enough energy to overcome the conduction band offset between the outer cladding layer and SCH region. These carriers will overflow into the outer cladding layer and diffuse away and contribute to the non-radiative current (Figure 6.5). The cladding carrier density $(n_{clad})$ is defined as

$$n_{clad}(x) = n_{clad}\big|_{x=0} \, e^{-x/L_n} \tag{6.30}$$

$$n_{clad}\big|_{x=0} = N_{c,clad} \exp\left(\frac{F_c - (E_{c,qw} + \Delta E_{c,sch})}{kT}\right) \tag{6.31}$$

where $\Delta E_c$ is the band offset between the quantum well and outer cladding region and $L_n$ is the diffusion length in the outer cladding region. It is assumed that the quasi-Fermi level in the quantum well is equal to the quasi-Fermi level at the edge of the outer cladding region.

The magnitude of the overflow current density is written as

$$
\begin{aligned}
|J_{overflow}| &= qD_n \left. \frac{dn_{clad}}{dx} \right|_{x=0} \\
&= \frac{qD_n N_{c,clad}}{L_n} \left( \frac{\pi \hbar^2 L_z}{m_e^*} n_{qw} \right) \exp\left( \frac{E_{e1} - E_{c,qw}}{kT} \right) \exp\left( \frac{-\Delta E_{c,sch}}{kT} \right)
\end{aligned}
\tag{6.32}
$$

As was the case for recombination in the SCH region, a large $\Delta E_c$ is desired to minimize the overflow current.

## 6.6   Doping the active region

Let us return briefly to the more simple model for the radiative recombination rate given by

$$
R_{rad} = F_{eff} B_0 n p
\tag{6.33}
$$

where $F_{eff}$ is the effect antenna enhancement derived earlier in this chapter. The 3dB frequency (ignoring non-radiative recombination for the moment) is given by (6.11) as

$$
f_{3dB} = (2\pi)^{-1}(2F_{eff}B_0 n)
\tag{6.34}
$$

For a high carrier density of $n = 5 \times 10^{18}$ cm$^{-3}$ the lifetime of the LED without antenna is calculated as $\tau_{rad} = 2$ ns resulting in a 3dB-frequency $f_{3dB} = (2\pi)^{-1} \tau_{rad}^{-1} \approx 200$ MHz. An high 500-fold antenna enhancement of the spontaneous emission rate is needed to increase $f_{3dB}$ to 100 GHz. The required enhancement is a more modest 250-fold enhancement if the injection carrier density is doubled to $10^{19}$ cm$^{-3}$; however, loss mechanisms such as Auger recombination and carrier overflow become large at high carrier densities and the current density required to achieve this carrier density would be impractically large. If the active region is instead doped p-type, the 3dB-frequency is given by

$$
f_{3dB} = (2\pi)^{-1}(F_{eff}B_0 p_0)
\tag{6.35}
$$

such that $f_{3dB}$ is independent of the injected carrier density. A p-type doping level of $p_0 = 2 \times 10^{19}$cm$^{-3}$ results in $f_{3dB} = 100$ GHz with a 250-fold antenna enhancement without requiring high current injection. It is possible to dope the active region to doping levels approaching the solid solubility limit of III–V materials to further reduce the spontaneous emission rate although for $p_0 > 5 \times 10^{19}$ cm$^{-3}$ Auger recombination can become very large and will place an upper limit on the doping level [110]–[112].

In principle, the active region can also be doped n-type. However, this is not desirable because of the small conduction band offset compared to the relatively large valence band offset in the InGaAs / InP materials system. With modest doping levels, the Fermi level will be pushed close to the conduction band edge at equilibrium thus limiting the the carrier density that can be injected at forward bias. This is further exacerbated by the low density of states in the conduction band because of the small effective mass of the electron.

## 6.7   Predicted 3dB-frequency, quantum efficiency, and power in the quantum well antenna-LED

The previous analysis is now applied to the quantum well antenna-LED shown in Figure 6.6a; similar to the device reported in Chapter 4. The antenna-LED consists of three 5 nm thick InGaAs coupled to a Ag cavity-backed slot antenna. The InGaAs quantum wells are cladded by a InGaAsP separate confinement heterostructure (SCH) barrier region which is further cladded by doped p-type and n-type InP regions. A thin 1 nm $Al_2O_3$ layer electrically isolates the antenna from the active region and a thick 150 nm spin-on-glass layer electrically isolates the antenna from the substrate. The semiconductor parameters assumed for the model are given in Table G.1 in Appendix G.

   We wish to study the antenna-LED device performance as a function of slot width. For each slot width, the cavity depth and slot length of the antenna were designed using full-wave simulation such that the spontaneous emission enhancement was maximized and the resonance wavelength overlapped with the emission of the active region ($\lambda_0 = 1500$ nm). During the design optimization, the cavity depth was not allowed to be smaller than 50 nm to ensure a reasonable thickness to encompass all of the device layers.

### Undoped active region
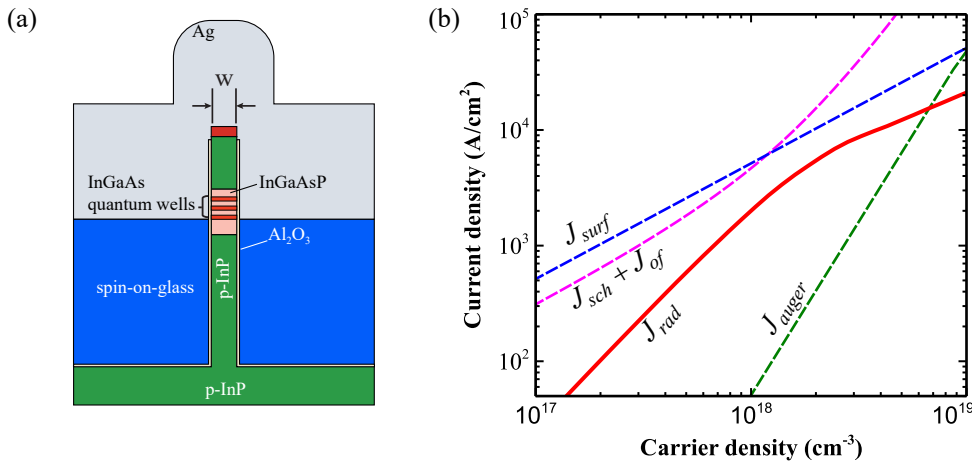


Figure 6.6: (a) Cross-section illustration of quantum well antenna-LED; and (b) current recombination and leakage pathways in the antenna-LED with undoped active region for slot width $w = 10$ nm. $J_{rad}$ (radiative recombination), $J_{surf}$ (surface recombination), $J_{auger}$ (Auger recombination), $J_{sch}$ (recombination in the SCH region), $J_{of}$ (overflow current into the InP cladding).

   We first consider the quantum well antenna-LED with an undoped active region. Plotted in Figure 6.6 are the current densities of the various recombination or leakage pathways that

make up the total current density in the forward biased antenna-LED with a slot width of
10 nm. The thick red line corresponds to the desirable radiative current ($J_{rad}$) whereas all
non-radiative currents are denoted with dashed lines. At low injection, the current density is
dominated by the surface recombination current ($J_{surf}$). As the injection level is increased,
the radiative current increases with the square of the carrier density and nearly overtakes
the surface recombination before saturating. The saturation of $J_{rad}$ is from the mismatch
between electron and hole momentum that becomes pronounced at high carrier density as a
result of the difference in the parabolicity of the conduction and valence bands.
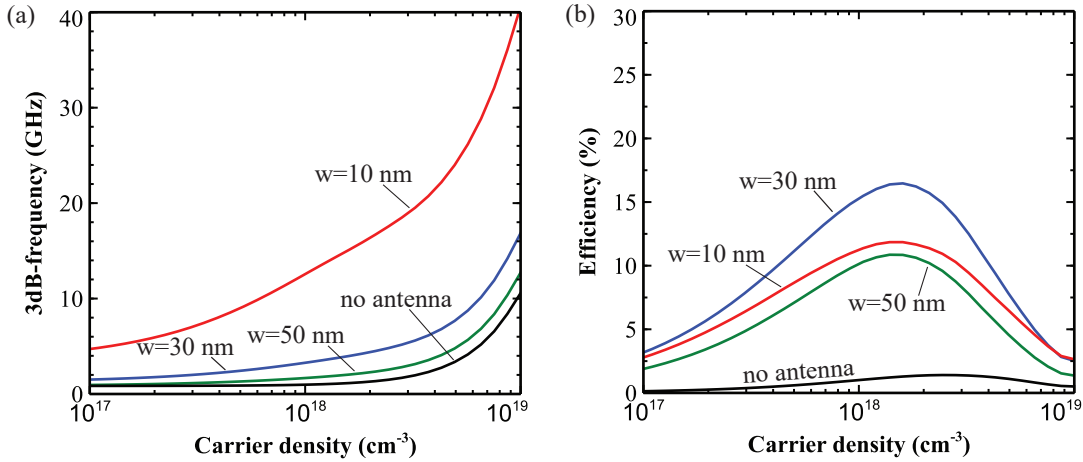


Figure 6.7: (a) 3dB-frequency ($f_{3dB}$) as a function of carrier density for antenna-LED with
different slot widths ($w$); and (b) quantum efficiency as a function of carrier density.

Interestingly, the recombination current in the SCH region ($J_{sch}$) is significant and in-
creases dramatically for carrier density $> 10^{18}$ cm$^{-3}$. The carrier density in the SCH region
is about an order of magnitude lower than the quantum well carrier density. But, because
of the large surface area of the SCH region, the surface recombination can become signifi-
cant, eventually even surpassing the surface recombination in the active region. Clearly, it
is important to ensure the surface recombination in the SCH region is as small as possible
and the surface area is reduced as much as possible.

The 3db-frequency ($f_{3dB}$) and quantum efficiency (QE) are plotted in Figure 6.7 as a
function of carrier density for the undoped antenna-LED and LED without antenna for
comparison. There is a clear trend of increasing $f_{3db}$ as the carrier density is increased. This
is the expected behavior given the radiative rate increases with the square of the carrier
density. For very high carrier density ($n > 5 \times 10^{18}$ cm$^{-3}$), $f_{3dB}$ increases dramatically from
the high radiative and Auger recombination recombination rate. The latter is undesirable
and helps contribute to the drop-off observed in the QE at high carrier density. At the
current density that corresponds to the the peak QE, $f_{3dB}$ is approximately 15, 5 and 2 GHz
for the 10, 30 and 50 nm wide antenna-LED respectively. The peak QE is $> 10\%$ for all
antenna-LEDs. Higher $f_{3dB}$ is possible if the lower QE can be tolerated. As expected, the

LED without antenna (black curve in Figure 6.7a-b) has much lower $f_{3dB}$ and QE compared with the antenna-LEDs.

## Doped active region
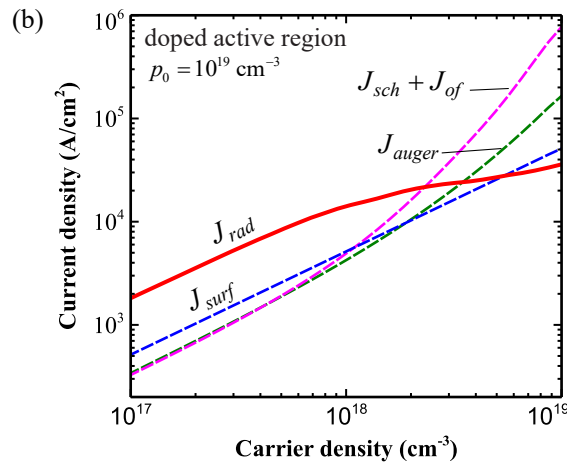


Figure 6.8: Recombination and leakage current pathways in the quantum well antenna-LED with 10 nm wide slot and p-doped active region
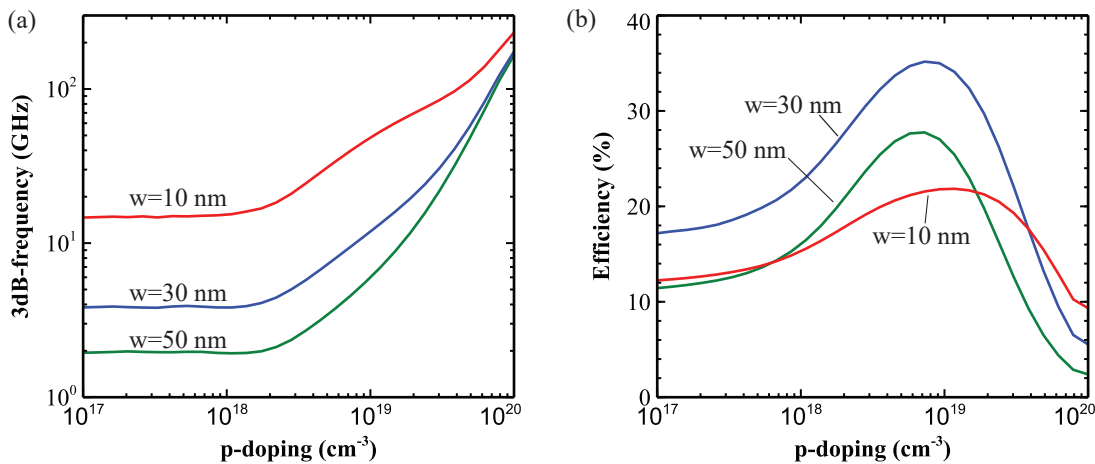


Figure 6.9: (a) 3dB-frequency ($f_{3dB}$) at peak quantum efficiency plotted as a function of p-doping density for antenna-LED with different slot widths ($w$); and (b) peak quantum efficiency plotted as a function of p-doping density.

Despite the presence of antenna-enhanced spontaneous emission, as shown above, a large carrier density is still needed to increase the radiative rate such that it can compete with

the non-radiative rate and produce reasonably high 3dB-frequency. Increasing the carrier
density works only to the extent that carriers remain in the active region and do not spill
out or recombine non-radiatively. As discussed previously, p-doping the active region can
help out in this respect. With high p-doping, it is not necessary to inject high numbers of
carriers into the active region for high efficiency and high speed.

An example of this is shown in Figure 6.9 where the recombination and leakage current
pathways is plotted for an antenna-LED with 10 nm wide slot and active region p-doping
of $p_0 = 10^{19}$ cm$^{-3}$. The radiative current ($J_{rad}$) easily exceeds the surface recombination
current ($J_{surf}$) at low carrier density. The drawback is that the Auger current ($J_{auger}$) has
now increased significantly and will limit the quantum efficiency at higher carrier density
along with the leakage current $J_{sch}$ and $J_{of}$. Plotted in Figure 6.9 is the the $f_{3db}$ of the
antenna-LED devices at peak QE as a function of p-doping in the active region. Plotted in
Figure 6.9b is the peak quantum efficiency at each p-doping level. The benefit of p-doping
above $10^{18}$ cm$^{-3}$ is evident. Modulation rates exceeding 100 GHz are possible in the 10 nm
wide antenna-LED with p-doping of $p_0 \approx 4 \times 10^{19}$ cm$^{-3}$ with quantum efficiency near 10%.
The usual tradeoff can be made between speed and efficiency if desired. At peak quantum
efficiency of 20% with $p_0 \approx 10^{19}$ cm$^{-3}$, $f_{3db}$ is reduced to 40 GHz for the 10 nm wide device.
With a slightly wider device ($w = 30$ nm) peak QE increases to 30% but now $f_{3dB}$ is reduced
to 10 GHz.

## Emitter energy per bit
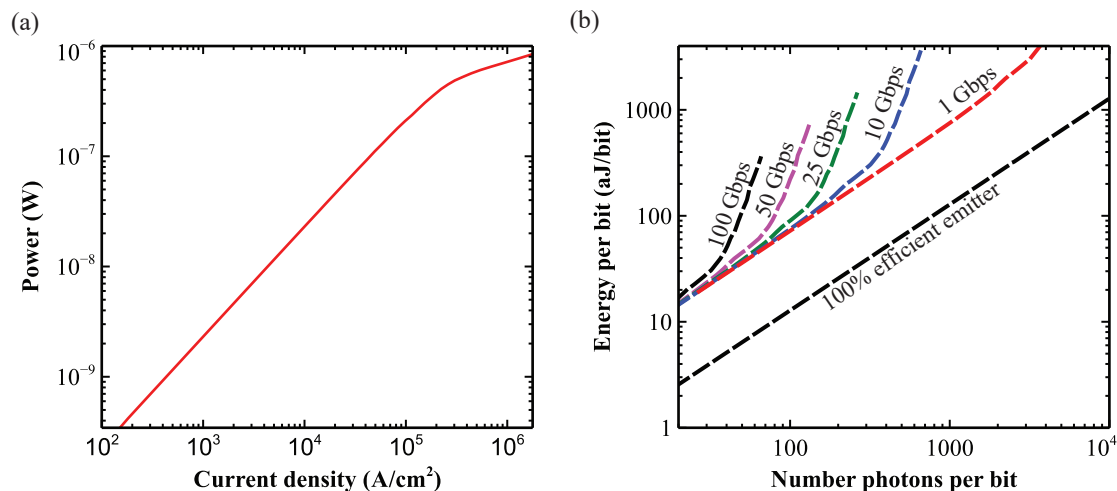


Figure 6.10: (a) Emitted power as a function of carrier density for highly-scaled 10 nm wide
antenna-LED; and (b) energy per bit and number of photons per bit of the emitter *only* for
several different data rates.

High speed modulation is not useful if there are not enough photons emitted from the
antenna-LED for each period of modulation. The power emitted by a single antenna-LED

with the highly-scaled slot width of 10 nm is plotted in Figure 6.10a as a function of current density. The active region is p-doped with $p_0 = 4 \times 10^{19}$ cm$^{-3}$ such that $f_{3dB} = 100$ GHz. Nearly a $\mu$W of output power is achievable before the quantum efficiency significantly decreases and the power saturates. 1 $\mu W$ of optical power at 100 Gbps modulation rate corresponds to about 100 photons/bit therefore a single highly-scaled antenna-LED emitter will produce at most something slightly less than 100 photons/bit at that data rate.

The energy per bit for a single antenna-LED emitter at various data rates is shown in Figure 6.10b. The energy per bit was calculated assuming a contact resistivity of $\rho_c = 10^{-7}$ $\Omega - $cm$^2$ and considers only the emitter energy (effectively assuming the rest of the optical link is 100% efficient). The energy per bit was calculated by first determining the photons per second for each data rate and number of photons per bit. The current density required at that photon emission rate was then calculated. From here, the quantum efficiency and power dissipated in the contact resistance was determined at that particular data point allowing for calculation of the total power dissipated in the antenna-LED and thus the energy per bit.

The choice of data rate and number of photons per bit needs to be carefully considered with the power dissipation in the receiver. In the best case scenario, at the fundamental quantum limit of photodetection[1] (number of photons per bit = 20), the antenna-LED can operate at $\approx$ 20 aJ/bit. In a realistic link, there is always loss and and the sensitivity of photodetector may exceed the quantum limit and therefore the emitter will need to produce more photons per bit and operate at a higher energy per bit. At a given data rate, the number of photons per bit can be increased by increasing the drive current. At some point, the drive current becomes so high that the quantum efficiency drops and the Ohmic loss from the contact resistance increases such that the energy per bit diverges. To avoid this, either additional emitters can be added in parallel or the data rate can be lowered. Depending upon the desired data rate, it may be preferable to use an antenna-LED that is not as highly-scaled and thus has a smaller spontaneous emission enhancement but higher quantum efficiency because of reduced non-radiative recombination.

The current densities in Figure 6.10a at first glance seem exceedingly high compared with a traditional LED. However, because of the proximity to metal and excellent thermal dissipation, the antenna-LED can support surprisingly high current density upwards of $10^6$ A/cm$^2$ without suffering from a large deleterious increase in the temperature[2].

## 6.8 Carrier transport effects

Up to this point it has been assumed that carriers are injected from the p-type and n-type region instantaneously into the active region with any change in the forward bias of the

---

[1]This comes about from the Poissonian photon statistics inherent in light; see for example [10]

[2]This is not necessarily true for poor contact resistance. According to thermal simulation, reasonably low contact resistivity $\rho_c < 10^{-5}$ $\Omega$-cm$^2$ is required to minimize thermal heating from Ohmic loss at the n-contact [113]
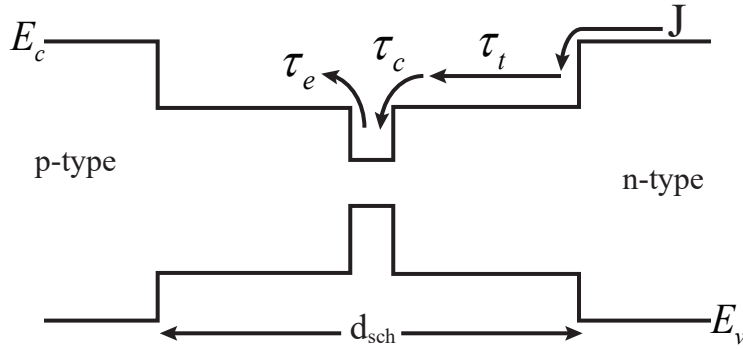
Figure 6.11: Band diagram of a quantum well antenna-LED showing transport of electrons and holes into the active region.

antenna-LED. However, at very high modulation speeds, the transport time may be of the same order as the inverse of the modulation frequency and can no longer be safely neglected. Following [60] and [114], Figure 6.11 shows a simplified view of carrier injection into a quantum well that is cladded by an undoped separate confinement heterostructure region. Electrons are injected into the SCH region with an applied bias from the highly doped n-type region. Electrons are then transported across the SCH via ambipolar diffusion with a transit time of $\tau_t$. Once reaching the quantum well, electrons are not instantaneously captured by the quantum well because of the energy difference between the SCH and quantum well states. It is thought that energy is conserved most likely by an emission of an longitudinal optical phonon by the electron although other scattering events are likely to contribute [115]–[118]. Whatever the case, it is convenient to assign a phenomenological capture time constant $\tau_c$ to represent the average time it takes an electron to be captured by the quantum well. The inverse can also happen: electrons that are captured within the quantum well are also able to escape back into the SCH region after a characteristic escape time $\tau_e$. Usually $\tau_e \gg \tau_c$ and so carrier escape will be ignored here.

Holes in the valence band will transport to the quantum well in the same manner. Holes diffuse to the quantum well with the same ambipolar diffusion coefficient and therefore identical transit time ($\tau_t$) as the electrons (assuming the SCH is symmetric about the quantum well). However the holes (being heavier than the electrons), are more efficiently captured into the quantum well as a result of the higher density of states inside the quantum well [119]. Therefore, it is sufficient to analyze only the electrons to understand the dynamic effects of carrier transport.

## Carrier transport across the SCH

Transit time across the SCH was previously studied for the case of a quantum well laser [114]. It was found in [114] and re-derived in Appendix H that the transit time $\tau_t$ is given

by the expression

$$\tau_t = \frac{(d_{sch}/2)^2}{2D_a} \tag{6.36}$$

where $d_{sch}$ is the width of the SCH region and $D_a$ is the ambipolar diffusion coefficient. Most III-V semiconductors have an ambipolar diffusion coefficient on the order of $\sim 1-10$ cm$^2$s$^{-1}$ therefore a transit time of a few picoseconds across 100 nm of the SCH region can be expected.

The effect of this transport time is to add a pole to the transfer function whose cutoff frequency is given by $(2\pi)^{-1}\tau_t^{-1}$. Therefore it is desirable to keep the SCH region sufficiently thin to ensure $\tau_t \ll \tau_{rad}$ where $\tau_{rad}$ is the radiative lifetime. Alternatively, the SCH region can be doped to minimize the length the carrier needs to diffuse to reach the quantum well. Although not advisable in a laser structure because of free carrier absorption, this can be tolerated in an antenna-LED because of the low antenna quality factor. With proper design of the active region, the transit time across the SCH region will not set the upper limit the maximum speed of the antenna-LED.

## Carrier capture in the quantum well

Carrier capture was theoretically studied by several groups leading to rather unfavorable predictions of carrier capture time $\tau_c > 10$ ps [116], [117], [119]. Fortunately, such long capture times have not been empirically observed; probably owing to the complexity of the electron capture process that was not fully taken into account in the theoretical models. Carrier capture time of $\tau_c < 1$ ps for electrons was empirically observed in an InP/InGaAs multiple quantum well structure [120]. Despite being extremely fast, it was found that the carrier capture time can still contribute to gain saturation and reduction in the relaxation oscillation frequency of the quantum well laser [114]. In the antenna-LED, it is shown in Appendix H that, much like the transit time, the effect of the capture time is to add another pole to the transfer function whose cutoff frequency is given by $(2\pi)^{-1}\tau_c^{-1}$. Therefore, the capture time will become important for modulation frequency exceeding 150 GHz.

## 6.9 Parasitic resistance and capacitance

High speed modulation is not achievable if the parasitic resistance and capacitance of the antenna-LED result in an RC time constant ($\tau_{RC}$) that is larger than the radiative lifetime ($\tau_{rad}$). An equivalent electrical circuit model valid at forward-bias for the antenna-LED is
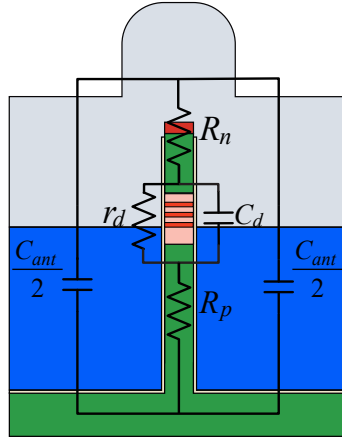
Figure 6.12: (a) Overlay of the equivalent circuit model on the schematic cross section of the antenna-LED with the inclusion of parasitic resistance and capacitance.

shown in Figure 6.12 where:

$$r_d = \text{diffusion resistance} = \frac{V_t}{I}$$

$$C_d = \text{diffusion capacitance} = \frac{I\tau}{V_t}$$

$$R_n = \text{series resistance of the n-type region} = A_{ridge}^{-1}\rho_c$$

$$R_p = \text{series resistance of the p-type region} = A_{ridge}^{-1}\left(\frac{L_p}{qp\mu_p}\right)$$

$$C_{ant} = \text{antenna capacitance} = \frac{\epsilon A_{ant}}{t_{ox}}$$

$$I = \text{forward current}$$

$$V_t = \text{thermal voltage}$$

$$\tau = \text{carrier lifetime}$$

$$\mu_n = \text{mobility of electrons}$$

$$\mu_p = \text{mobility of holes}$$

$$\rho_c = \text{contact resistivity of n-contact}$$

$$L_n = \text{length of n-type region}$$

$$L_p = \text{length of p-type region}$$

$$A_{ridge} = \text{area of semiconductor ridge}$$

$$A_{ant} = \text{area of the antenna}$$

$$\epsilon = \text{permittivity of the insulator between the antenna and underlying substrate}$$

$$t_{ox} = \text{thickness of the insulator between the antenna and underlying substrate}$$

The pn junction is modeled with an intrinsic diffusion resistance ($r_d$) and capacitance ($C_d$); the junction capacitance is generally smaller than $C_d$ at forward bias and thus ignored [92]. Because of small cross sectional area, the series resistance in the n-type ($R_n$) and p-type ($R_p$) regions cannot be neglected. $R_n$ will be dominated by the contact resistance between the antenna and top of the ridge. The p-contact area is assumed to be significantly larger and thus negligible; however owing to the low mobility of the hole, the resistance of the p-type layer can be large. The primary effect of the antenna is to add a capacitance $C_{ant}$. This can simply modeled as a parallel plate capacitance that forms between the antenna metal and underlying substrate.

The RC time constant for the equivalent circuit can be evaluated by deriving the transfer function and determining the dominant pole. Instead, to avoid the lengthy derivation, we recognize that $C_d$ and $C_{ant}$ will each effectively contribute a pole to the transfer function with a break frequency equal to the inverse of the the particular time constant associated with each capacitor when the other is left open. The overall RC time constant will then be dominated by the larger of these two RC time constants. By inspection, the first time constant is given by $\tau_{RC,1} = C_d(r_d + R_n \parallel R_p)$ and the second time constant by $\tau_{RC,2} = C_{ant}(R_n + R_p + r_d)$.

The time constants $\tau_{RC,1}$ and $\tau_{RC,2}$ can be further simplified under certain limiting assumptions. For typical device forward current ($I < 1\mu A$) we can expect $r_d > 25$ k$\Omega$. Assuming $p = 5 \times 10^{18}$ cm$^{-3}$, $\mu_p = 100$ cm$^2$(V$\cdot$s)$^{-1}$, $L_p = 200$ nm, and $A = 4000$ nm$^2$ we can estimate the series resistance of the p-type layer as $R_p = 6.3$ k$\Omega$. The n-type series resistance is estimated as $R_n = 2.5$ k$\Omega$ for an excellent contact resistivity of $\rho_c = 10^{-7}$ $\Omega - $cm$^2$ and $R_n = 2.5$ M$\Omega$ for a poor contact resistivity of $\rho_c = 10^{-4}$ $\Omega - $cm$^2$. $\tau_{RC,1}$ can be simplified by recognizing that $r_d$ is much greater than $R_n \parallel R_p$ such that $\tau_{RC,1} \approx r_d C_d$ which is simply the intrinsic speed of the pn junction without parasitic resistance or capacitance. Therefore, $\tau_{RC,2}$ can be interpreted as the RC time constant from the parasitic resistance and capacitance of the antenna-LED. Ensuring the device is not limited by parasitics is then tantamount to maintaining the inequality $\frac{\tau_{RC,2}}{\tau_{RC,1}} < 1$ which can be rewritten as

$$(R_n + R_p)C_{ant} < \tau \tag{6.37}$$

For a given contact resistivity, this will place a restriction on the antenna capacitance and therefore the antenna geometry. This is summarized in Figure 6.13 where the parasitic RC time is plotted as a function of antenna area for several different values of contact resistivity. In plotting Figure 6.13 it is assumed the antenna capacitance consists of the antenna and underlying substrate separated by a 100 nm oxide with refractive index of 1.5. The smallest possible antenna area is simply the area of the semiconductor ridge ($\approx \rho_c = 10^{-4}$ $\Omega - $cm$^2$) and therefore sets the lower bound of the x-axis of Figure 6.13. The y-intercept can be interpreted as the lowest possible RC time constant for the contact resistivity associated with each curve. Even for a poor contact resistivity of $\rho_c = 10^{-4}$ $\Omega - $cm$^2$, the RC time constant of the parasitic resistance and capacitance can still be as fast as 1 ps thus becoming a limiting factor only when the modulation speed approaches 150 GHz. For an excellent contact resistivity of $\rho_c = 10^{-7}$ $\Omega - $cm$^2$ an RC time constant on the order of femtoseconds can be achieved.
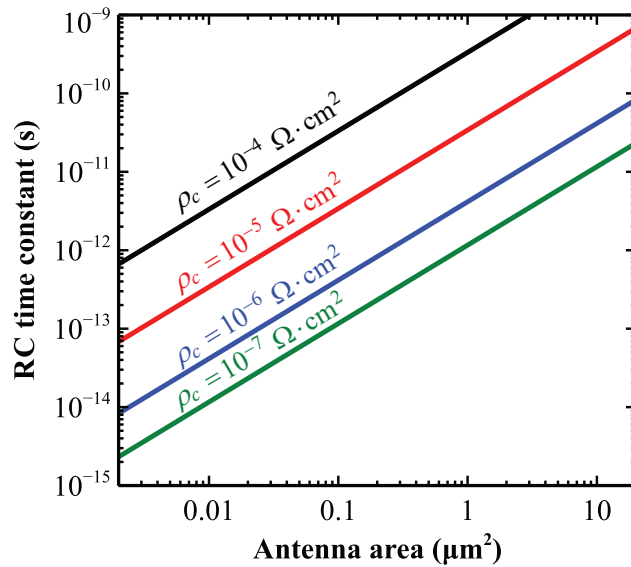
Figure 6.13: Plots of RC time constant of the parasitic resistance and capacitance as a function of antenna area for several different values of contact resistivity.

In practice, it is desirable to have an antenna area with a size $(\lambda/n)^2$ (where $n$ is the refractive of the underlying InP substrate) to ensure the far-field radiation pattern has a single main lobe. This corresponds to an antenna area of 0.25 $\mu$m$^2$. It is then desirable as can be seen from Figure 6.13 to have $\rho_c < 10^{-6}$ $\Omega - $cm$^2$ to achieve 100 GHz direct modulation. Fortunately, $\rho_c < 10^{-6}$ $\Omega - $cm$^2$ is readily achievable for III-V semiconductors. Therefore, with proper design of the antenna size and moderately low contact resistivity, the parasitic resistance and capacitance will not be the limiting factor in aching high antenna-LED modulation speeds.

# Chapter 7

# Conclusion

A practical LED that is faster than the laser is within reach. In this dissertation, I reported an electrically-injected III–V antenna-LED with cavity-backed slot antenna that is capable of achieving this goal and is a suitable candidate for on-chip optical interconnects. I discussed the design, fabrication, and measurement of the electrically-injected antenna-LED including the demonstration of a device with 200-fold increase in the spontaneous emission rate. Strategies for increasing the quantum efficiency including a new novel technique of producing clean III–V surfaces was reported. Using a detailed rate equation model, it was shown that greater than 100 GHz direct modulation rate is ultimately achievable with the antenna-LED.

Recapitulating the results from the last several chapters, the primary advantages of the antenna-LED device reported in this dissertation are summarized below:

1. **Self-alignment of active region to antenna.** The fabrication of the antenna-LED is straightforward. The active region is self-aligned with the antenna without the need for precise lithographical alignment.

2. **Simple electrical injection.** The antenna also serves as one of the electrodes; electrical injection comes for "free".

3. **Directional emission**. Light emission goes into one direction. Integration of the antenna-LED with a waveguide should be trivial.

4. **High spontaneous emission enhancement**. The cavity-backed slot antenna allows for tuning of the radiation resistance to achieve maximum spontaneous emission enhancement.

5. **High speed and high efficiency**. $> 100$ GHz direct modulation rate with 20% efficiency is achievable with a highly-scaled antenna-LED. Spontaneous emission rate can exceed the non-radiative rate despite the presence of large surface recombination typical of III–V semiconductors.

## Future work

Much work remains before implementation of the antenna-LED as a light source for on-chip optical interconnects. I showed that high efficiency operation is possible; however, experimental demonstration of an efficient antenna-LED is still needed. Following the approach I prescribed in Chapter 2, I believe this goal is within reach. High speed operation requires both very narrow ($\approx$ 10 nm wide) high aspect semiconductor ridges and high p-doping ($> 10^{19}$ cm$^{-3}$). Neither are fundamental limitations to achieving high speed but nonetheless will require considerable process development. Measuring the speed of the antenna-LED through direct high-frequency electrical modulation still needs to be demonstrated but will pose experimental challenges because of the inherently low output power of the antenna-LED from its small size.

Integration of an antenna-LED within a full optical link is still largely unexplored. Integration with a waveguide in principle should be straightforward to design given the directionality of light emission but will pose fabrication and system integration challenges from the additional complexity involved. More generally speaking, there are a number of open questions about the implementation of on-chip optical interconnects. For example, what is the required antenna-LED modulation speed, how many photons per bit will be needed by the photodetector, and what kind of circuit is used to electrically drive the antenna-LED? These are among many other challenging questions that need to be addressed and will require the close collaboration of device, circuit, and systems-level experts.

# Appendix A

# Shockley-Ramo Theorem

Schockley and Ramo independently derived an expression for the current induced by an electron moving between two electrodes as

$$i = qEv \tag{A.1}$$

where $v$ is the velocity of an electron and $E$ is the electric-field that would exist if the electron was removed and one of the electrodes was raised to unit potential and the other grounded.
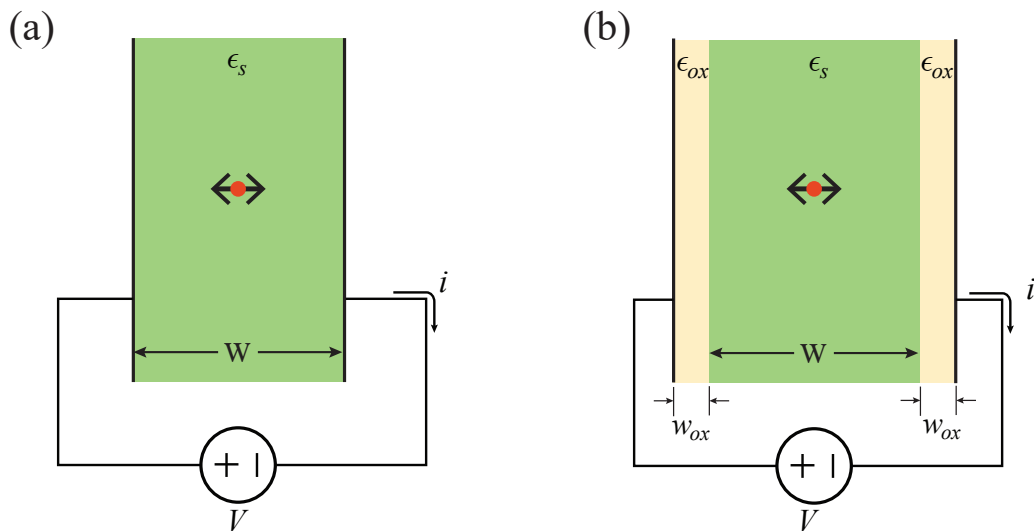


Figure A.1: (a) Drawing of dipole emitter placed in a homogenous dielectric medium between two parallel electrodes; and (b) same dipole placed in an inhomogeneous medium between two parallel electrodes.

## Induced current in an antenna with homogenous material in the feedgap

The Shockeley-Ramo Theorem was originally derived to calculate the electrode in vacuum tubes but is used in this dissertation to derive the current induced in the antenna feedgap of the dipole and slot antenna. The antenna feedgap is modeled as a parallel plate capacitor with plate separation $w$ as shown in Figure A.1. We first assume the antenna feedgap is filled with a dielectric with permittivity $\epsilon_s$. Consider a small oscillating dipole moment placed in the feedgap and consisting of a fixed positive charge with time-harmonic oscillating negative charge with velocity $v = j\omega_0 x_0 \exp(j\omega_0 t)$

The electric-field without the presence of the charge and one electrode raised to unit potential is simply given by $E = 1/w$. Assuming the current is time-harmonic, then by Shockley-Ramo Theorem

$$i = i_0 \exp(j\omega_0 t) = qEv = \frac{q}{w} j\omega_0 x_0 \exp(j\omega_0 t) \tag{A.2}$$

$$|i| = \frac{q\omega_0 x_0}{w} \tag{A.3}$$

Notice that the induced current does not depend on the permittivity of the dielectric medium filling the antenna gap.

## Induced current in an antenna with inhomogeneous material in the feedgap

Consider now the antenna gap filled with inhomogeneous dielectric such as Figure A.1b. The dielectric with permittivity $\epsilon_s$ is now cladded on either side with another dielectric with permittivity $\epsilon_{ox}$. This is precisely the situation for the III–V antenna-LED in which the III–V semiconductor is cladded on either side by a low-index oxide. The electric-field at the dipole is now no longer given by $1/w$ when one of the electrodes is brought to unit potential. If we define $E_s$ as the electric-field in the inner dielectric and $E_{ox}$ as the electric-field in the cladding dielectric then an expression can be written to relate $E_s$ and $E_{ox}$ as

$$1 = E_s w + 2E_{ox} w_{ox} \tag{A.4}$$

Applying the boundary condition across the interface

$$E_{ox} = \frac{\epsilon_s}{\epsilon_{ox}} E_s \tag{A.5}$$

Then, plugging (A.5) into (A.4)

$$E_s = \frac{1}{w + 2\frac{\epsilon_s}{\epsilon_{ox}} w_{ox}} = \frac{1}{w_{eff}} \tag{A.6}$$

where $w_{eff}$ is the effective width. For $\epsilon_s = \epsilon_{ox}$, $w_{eff}$ is simply the physical width $w + w_{ox}$. However, if $\epsilon_{ox} < \epsilon_s$, then $w_{eff} > w$ and the effective width is larger than the physical width. By the Shockley-Ramo Theorem

$$
\begin{aligned}
|i| &= \frac{q\omega_0 x_0}{w + 2\frac{\epsilon_s}{\epsilon_{ox}} w_{ox}} \\
&= \frac{q\omega_0 x_0}{w_{eff}}.
\end{aligned}
\tag{A.7}
$$

The radiated power in an antenna is proportional to the induced current squared. Therefore, the spontaneous emission enhancement in an antenna with cladding layer is $\alpha F$ where F is the spontaneous emission enhancement in the case without cladding layer and $\alpha$ is the enhancement penalty factor given by

$$
\alpha = \left( 1 + \frac{\epsilon_s}{\epsilon_{ox}} \frac{2w_{ox}}{w} \right)^{-2}
\tag{A.8}
$$

# Appendix B

# Metals at optical frequencies: the kinetic inductance

At optical frequencies ($f \approx 100$ - $800$ THz) metals no longer behave as perfect electrical conductors and a more realistic model of metals needs to be considered.

## B.1 Equation of motion for free electrons

Noble metals can be described well using the Drude-Lorentz which assumes that a "sea of electrons" exist in a metal that are not bound to any atomic ion. A one-dimensional equation of motion for free electrons can be written as

$$m_0 \frac{dv}{dt} = -\frac{m_0}{\tau}v - qE \tag{B.1}$$

where

$$v = \text{electron velocity}$$
$$m_0 = \text{electron mass}$$
$$\tau = \text{relaxation time}$$
$$E = \text{applied electric field}$$

The relaxation time is the average time between scattering events for an electron in a metal and can be related to the relaxation frequency ($\gamma$) by $\gamma = \tau^{-1}$. Under time-harmonic analysis, the electric field is given by $E = E_0 e^{j\omega t}$ and electron velocity by $v = v_0 e^{j\omega t}$. The equation of motion then becomes

$$m_0 j\omega v_0 = -\frac{m_0}{\tau}v - qE_0 \tag{B.2}$$

## AC impedance and kinetic inductance

Solving for $v_0$ gives

$$v_0 = -\frac{qE}{m_0(1 + j\omega\tau)} \tag{B.3}$$

Given $J = \sigma E_0 = -Nqv_0$ where $J$ is the current density, $\sigma$ is the metal conductivity and $N$ is the density of free electrons in the metal

$$\sigma = \frac{Nq^2\tau}{m_0(1 + j\omega\tau)} \tag{B.4}$$

We can write the impedance of a metal with such a conductivity as

$$
\begin{aligned}
Z &= \sigma^{-1}\frac{\text{length}}{\text{area}} \\
&= \frac{m_0(1 + j\omega\tau)}{Nq^2\tau}\frac{\text{length}}{\text{area}} \\
&= \frac{m_0}{Nq^2\tau}\frac{\text{length}}{\text{area}} + (j\omega)\frac{m_0}{Nq^2}\frac{\text{length}}{\text{area}}
\end{aligned} \tag{B.5}
$$

The first term is real and can be interpreted as the resistance whereas the second term is imaginary and has the form of an inductance such that

$$L_K = \frac{m_0}{Nq^2}\frac{\text{length}}{\text{area}} \tag{B.6}$$

where $L_K$ is called the kinetic inductance. For low-frequencies, the kinetic inductance is safely ignored. However at optical frequencies, $L_K$ may no longer be small. As described in Chapter 3, $L_K$ is the result of the electrons not being able to respond to a an applied electron-field at high frequencies. The electrons movement lags behind the applied electric-field (i.e. current lags behind the voltage as in an inductor).

It is more useful to write $L_K$ in terms of the bulk properties of the metal. We note that $\nabla \times \mathbf{H}$ can be written equivalently as

$$\nabla \times \mathbf{H} = j\omega\epsilon_0\epsilon_R\mathbf{E} = (j\omega\epsilon_0 + \sigma)\mathbf{E} \tag{B.7}$$

where in the first expression the properties of the metal are modeled as a dielectric with relative permittivity $\epsilon_R$ and in the second as a metal with conductivity $\sigma$. Both expressions are equal if

$$\sigma = j\omega\epsilon_0(\epsilon_R - 1). \tag{B.8}$$

Therefore

$$
\begin{aligned}
Z &= \frac{1}{\sigma}\frac{\text{length}}{\text{area}} \\
&= \operatorname{Re}\rho\frac{\text{length}}{\text{area}} + j\omega\frac{\operatorname{Im}\rho}{\omega}\frac{\text{length}}{\text{area}} \\
&= \operatorname{Re}\rho\frac{\text{length}}{\text{area}} + j\omega L_k
\end{aligned} \tag{B.9}
$$

where

$$L_K = \frac{\text{Im}\,\rho}{\omega} \frac{\text{length}}{\text{area}} \tag{B.10}$$

# B.2 "Plasmonicity" of the cavity-backed slot antenna

A back-of-the-envelope calculation is used to derive the fraction of Faraday inductance ($L_F$) to kinetic inductance ($L_K$) to get a sense of the "plasmonicity" of the cavity-backed slot antenna. The Faraday inductance of the cavity-backed slot antenna comes primarily from the cavity inductance which can be roughly modeled as a parallel plate transmission line with inductance given by

$$L_F = \frac{\mu_0 w d_c}{L} \tag{B.11}$$

where $w$ is the slot width, $d_c$ is the cavity depth, and $L$ is the slot length. The kinetic inductance is estimated as

$$L_K = \frac{\text{Im}\,\rho}{\omega} \frac{\text{length}}{\text{area}} \approx \frac{-(\omega\epsilon_0\epsilon_R)^{-1}}{\omega} \frac{d_c}{\delta_s L}$$
$$= \frac{-1}{\omega^2\epsilon_0\epsilon_R} d_c \delta_s L \tag{B.12}$$

where $\delta_s$ is the skin depth and it is assumed that the current flows within the skin depth on either side of the slot into the cavity therefore the cross-sectional area of current flow is approximately given by $2\delta_s L$. As a gauge of "plasmonicity", the ratio of $L_F$ to $L_K$ is calculated as

$$\frac{L_F}{L_K} = \frac{\mu_0 w d_c / L}{(-\omega^2\epsilon_0\epsilon_R)^{-1} d_c(\delta_s L)^{-1}}$$
$$\approx 2\mu_0 w \epsilon_0 \omega_p^2 \delta_s \tag{B.13}$$

where $\epsilon_R$ was approximated as $\epsilon_R \approx -\omega_p^2\omega^2$ and $\omega_p$ is the plasma frequency of the metal. The skin depth is $\delta_s \approx 25$ nm at optical frequencies. For slot width of $w = 30$ nm and silver plasma frequency of $\omega_p = 1.4 \times 10^{16}$ rad/s, $L_F/L_K \approx 3$ therefore the "plasmonicity" is low. As the width ($w$) of the slot is scaled down, it can be seen from (B.13) that the "plasmonicity" will increase. As described in the main text, this will result in a shortening of the slot length to maintain the same resonance frequency and therefore a reduction in the antenna efficiency. High "plasmonicity" should be avoided when possible.

# Appendix C

# Electroluminescence and dark-field scattering: experimental setup

## C.1 Electroluminescence (EL)
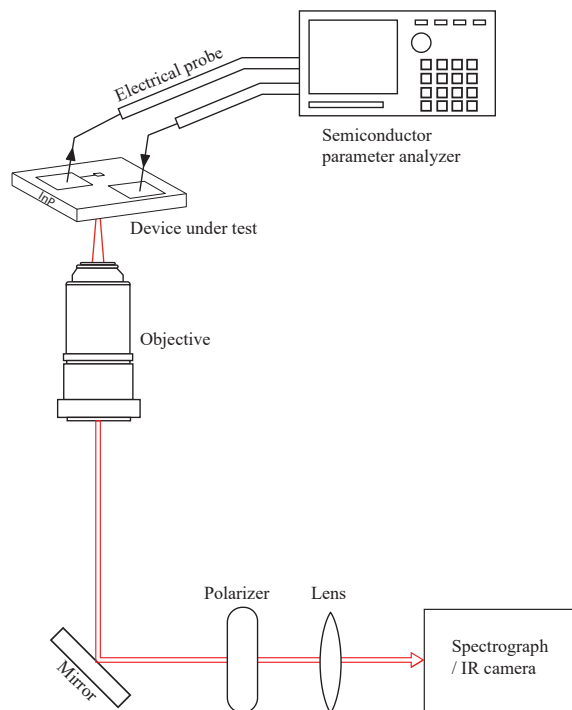


Figure C.1: Simplified schematic of the optical measurement setup used to measure electroluminescence.

Shown in Figure C.1 is a simplified diagram of the optical measurement setup used

to measure electroluminescence (EL) from a forward-biased antenna-LED. The antenna-LED was forward-biased using a constant current source from a HP4145B semiconductor parameter analyzer. An inverted microscope (Nikon TE-2000U) was used to collect and focus this light onto the entrance slight of a spectrometer (Acton instruments). The spectrometer was connected either to a liquid nitrogen cooled linear InGaAs CCD (Princenton Instruments OMA-V) for spectral measurements or thermoelectrically cooled 2D InGaAs CCD (Sensors Unlimited) for imaging. The polarization of the emitted light was measured by inserting a linear polarizer in front of the entrance slit of the spectrometer. For measurements in which spectrally integrated intensity was measured, a long pass filter was inserted in front of the spectrometer slit to block light emission from the p-InGaAsP contact layer (not shown in Figure C.1)

## C.2 Dark-field spectroscopy
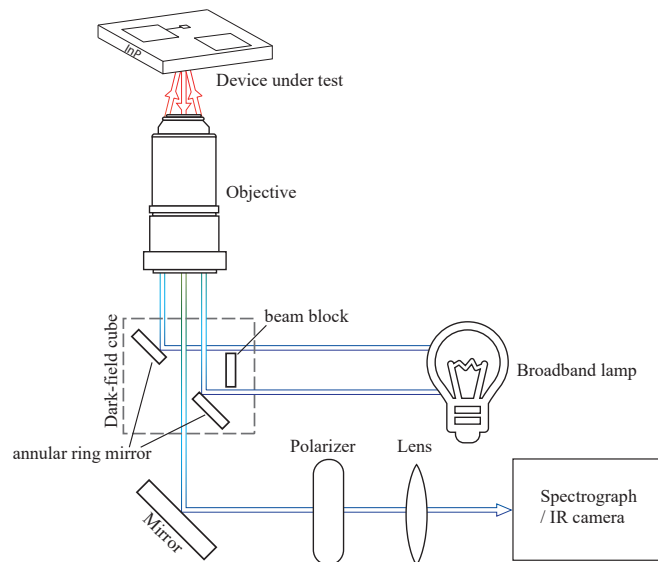


Figure C.2: Simplified schematic of the optical measurement setup used to measure dark-field scattering.

Dark-field spectroscopy was used to measure the resonance behavior of the antenna-LEDs [121]–[126]. The simplified diagram of the dark-field optical setup is shown in Figure C.2. A broadband light source consisting of a tungsten-halogen lamp was used to illuminate the sample with a dark-field objective. A homemade darkfield cube consisting of a beam block and annular ring mirror was placed between the dark-field objective and lamp to ensure that only the outer collar of the objective was illuminated by the lamp. Light that was scattered from the sample and entered the objective front lens was able to transmit through the center

of the annular ring mirror and was focused onto either the spectrometer or imaging CCD camera as shown in the diagram. For all spectral measurements, the measured scattering from the antenna was normalized by the light intensity spectrum of the tungsten-halogen lamp.

# Appendix D

# Conformal angled evaporation
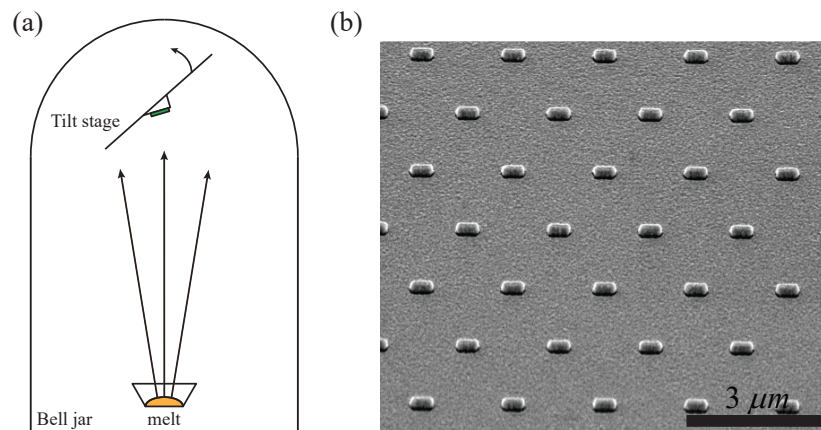


Figure D.1: (a) Simplified diagram of the metal evaporator with in-situ stage tilt mechanism; and (b) oblique angle SEM view of semiconductor ridges covered with evaporated Ag using tilt stage.

Electron-beam evaporation is capable of depositing high-quality and reasonably low-loss metal films for use in metal optics. Unfortunately, deposition is well-known to occur through line-of-sight travel from the melt to the sample therefore resulting in poor coverage of the sidewalls of etched features. To greatly improve the sidewall coverage, angled evaporation with an in-situ tilt stage was employed during evaporation of the antenna on the antenna-LED ridge. Shown in Figure D.1 is the simplified setup of the evaporator. The tilt stage was capable of 0-90° angle adjustment through an external adjustment knob. The sample was mounted on a jig with a 45° angle in order to pre-tilt the sample and allow for -45 to 45° sweep about the normal to the substrate surface .

Figure D.2a shows a focused ion beam cross (FIB) section of an InP ridge covered with evaporated silver (Ag) in which stage tilt was not used. Inserted in between the InP ridge and

evaporated Ag is a 15nm of atomic layer deposited (ALD) $Al_2O_3$. There is poor coverage of the Ag on the sidewall of the ridge and a closure defect which will both unpredictably shift the antenna resonance. When angled evaporation is used, the sidewall coverage is excellent and there is no closure defect as can be seen in Figure D.2b.

It has been reported that a thin germanium (Ge) layer can help improve the wetting of Ag to $Al_2O_3$ to produce ultra smooth surfaces [127]. Therefore, for all devices reported in this dissertation, a thin ( 3 nm) geranium (Ge) interfacial layer was deposited between the Ag and $Al_2O_3$. However, it was later determined that the Ge wetting layer was not needed for a good interface between Ag and $Al_2O_3$ in the antenna-LED [128]. Deposition of Ag without the lossy Ge wetting layer is expected to improve the antenna efficiency [129].
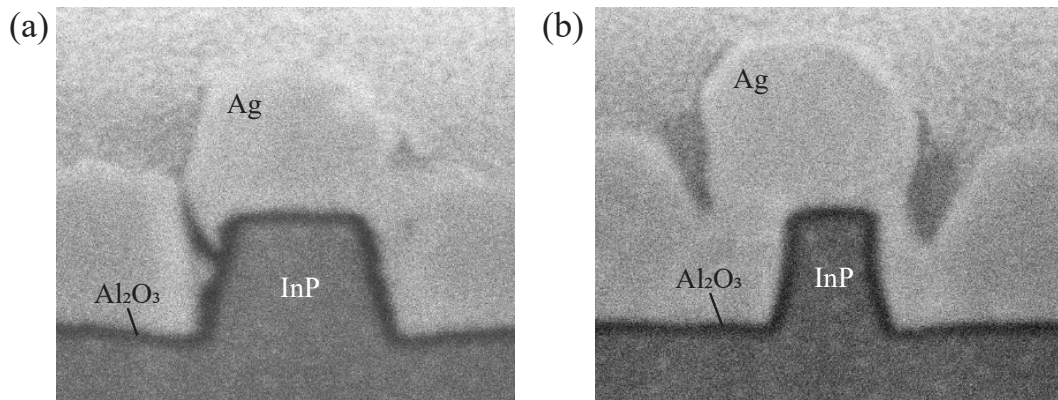


Figure D.2: Focused ion beam (FIB) cross-sections of InP ridge covered with evaporated Ag (a) without stage tilt during evaporation; and (b) with stage tilt during evaporation

The antenna resonance of test antenna-LED structures consisting of Ag deposited with and without evaporator stage tilt was measured using dark-field spectroscopy. Shown in Figure D.3a is the scattering spectra of several identical antenna-LED devices that were fabricated without stage tilt. A large deviation in the antenna resonance wavelength and shape of the spectrum was observed between each of the devices. The antenna behavior improved significantly when stage tilt was used during evaporation as can be seen in Figure D.3. Both the antenna resonance wavelength and spectral shape are consistent between devices.
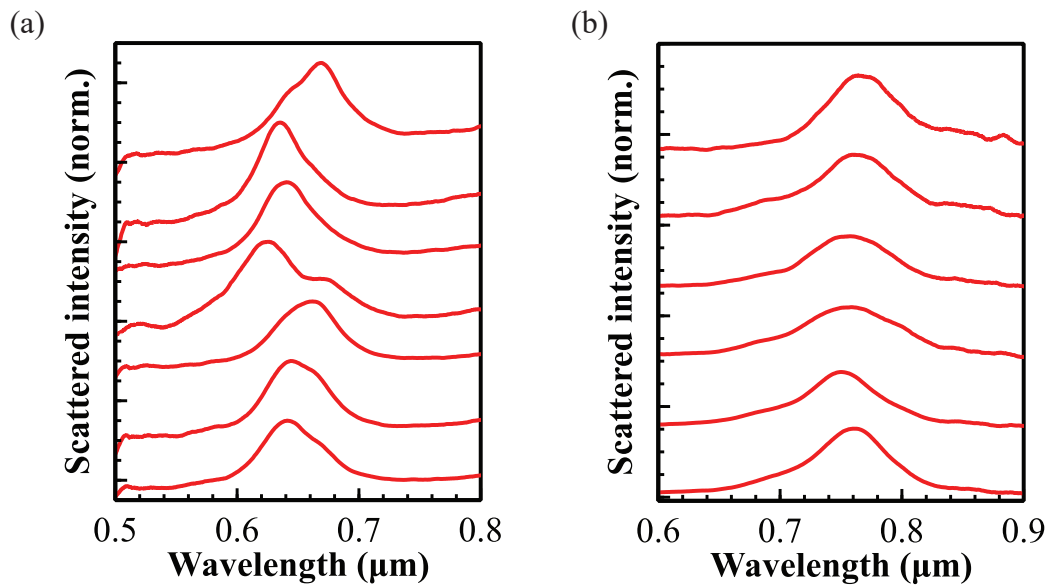
Figure D.3: Dark-field scattering spectrum from antenna-LED devices (a) without stage tilt during evaporation; and (b) with stage tilt during evaporation.

# Appendix E

# Epitaxial III–V wafers for the antenna-LED

(a)

(b)

InP cap (u.i.d.) (20nm)
InGaAs (u.i.d.) (8nm)
n-InP (5 x $10^{19}$ cm$^{-3}$) (20nm)
n-InP ($10^{19}$ cm$^{-3}$) (350nm)
InP setback (u.i.d.) (10nm)

InGaAsP (u.i.d.) (35nm)

InP setback (u.i.d) (25nm)

p-InP (5 x $10^{18}$ cm$^{-3}$) (150nm)

p-InGaAsP ($10^{19}$ cm$^{-3}$) (150nm)

InP buffer (u.i.d.) (50nm)

InP substrate (S.I.)

n-InGaAs ($10^{19}$ cm$^{-3}$) (40nm)

InGaAsP (u.i.d.) (40nm)

InGaAsP (u.i.d.) (60nm)

InP setback (u.i.d.) (100nm)

p-InP (5 x $10^{18}$ cm$^{-3}$) (250nm)

InP substrate (S.I.)

InP cap (u.i.d.) (20nm)

n-InP ($10^{19}$ cm$^{-3}$) (30nm)
InGaAs QW (u.i.d.) (6nm)
InGaAsP (u.i.d.) (10nm)
InGaAs QW (u.i.d.) (6nm)
InGaAsP (u.i.d.) (10nm)
InGaAs QW (u.i.d.) (6nm)

Figure E.1: Epitaxial wafers used for the electrically-injected antenna-LED devices reported in Chapter 4

# Appendix F

# Lifetime measurement with time-correlated single photon counting (TCSPC)

The lifetime of semiconductor ridges was measured using time-correlated single photon counting (TCSPC). Compared with other lifetime measurement techniques such as pump-probe, upconversion, or streak camera, TCSPC has several advantages such as to low cost, large dynamic range, high sensitivity and good timing resolution ($< 20$ ps) [130].

## Principles of TCSPC

The basic operating principle of TCSPC is demonstrated in Figure F.1. A periodically pulsed laser first generates a short (picosecond or less) laser pulse. Some of the laser pulse is sent to the sample and the rest is split off to a fast photodiode. The pulsed laser will generate a short pulse from the photodiode (Figure F.1a) which is sent to the timing electronics and used to sync the laser pulse a $t = 0$ s reference in time. Upon excitation by the laser pulse, the excited sample will begin to photoluminesce and emit photons toward a single photon detector. When a photon reaches the single photon detector, a photon detection event pulse will be generated (Figure F.1b) and sent to the timing electronics. The difference in time between the laser sync and photon detection event will then be recorded into a time bin. This is repeated over many cycles of the laser pulse train to build up a histogram of detection events as a function of time bins. The lifetime decay curve of the sample will simply be the envelope of this histogram (Figure F.1c).

Implied in Figure F.1b, the intensity of the photoluminescence from the sample is kept low enough such that - at most - a single photon detection event is registered for every pulse from the laser. If more than one photon is emitted during each laser pulse, only the first photon will be detected. This would lead to an artificial overemphasis of early photons in the histogram of photon counts thus indicating a faster decay time compared to the actual decay time. This effect is known as pile-up. In practice, to avoid this effect, the count rate
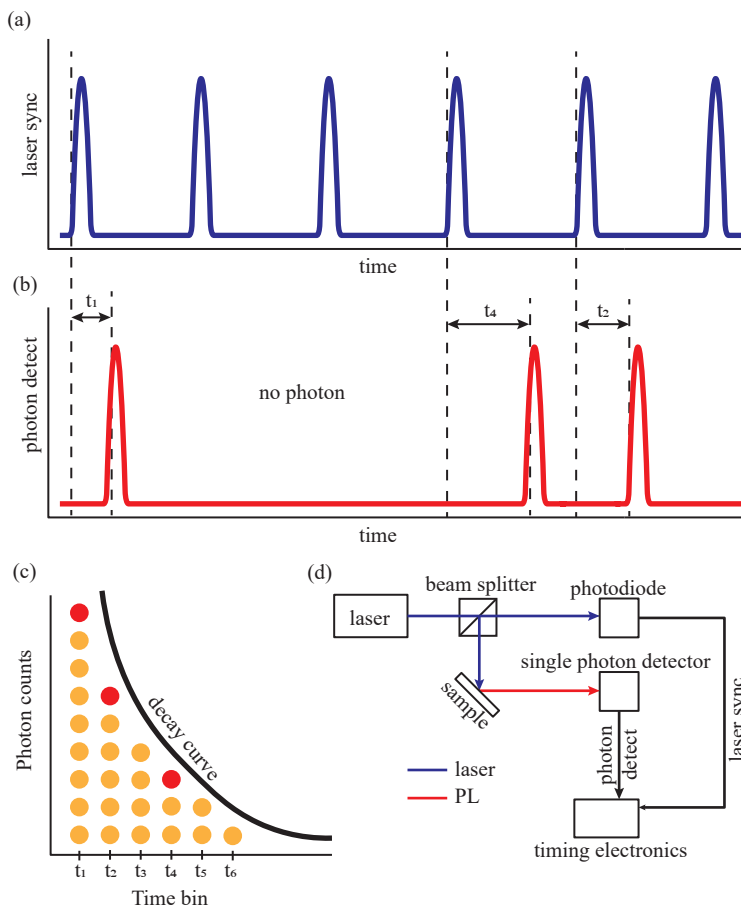
Figure F.1: Simplified diagram of the TCSPC lifetime measurement. (a) Timing diagram of the laser sync output from the fast photodiode; (b) timing diagram of the output of the single photon detector; (c) simplified histogram of photon counts vs. time bin used to build up the semi-continuous decay curve; and (d) simplified block diagram of the TCSPC hardware.

is kept below 10% of the laser pulse repetition rate. The repetition rate itself should be as high as possible while ensuring that the time between laser pulses is at least 10 times as long as the expected decay time of the sample.

The timing resolution of TCSPC is usually limited by the single photon detector which are most commonly avalanche photodetectors (APDs) operating in Geiger-mode. In Geiger-mode, the APD is biased slightly above avalanche breakdown such that a single photon can trigger an avalanche cascade of carriers resulting in short pulse at the output of the APD. Ideally, this pulse would appear as an impulse function, but in reality has some spread which is characterized by a full-width-half-maximum (FWHM). This leads to so-called timing jitter which gives some uncertainty about the true photon arrival time at the APD. Silicon is the choice of material for APDs at visible light frequencies and can achieve quantum efficiencies exceeding 50% with timing jitter < 30 ps. At longer near-IR wavelengths, InGaAs APDs are

commonly employed and have slightly worse quantum efficiency ($\approx 10 - 30\%$) and timing jitter ($< 100$ ps). Recently, superconducting nanowire single photon detectors have become commercially available and have shown excellent efficiency ($> 75\%$) and timing jitter ($< 30$ ps) at both visible and near-IR wavelengths [131].

## TCSPC at near-IR wavelengths
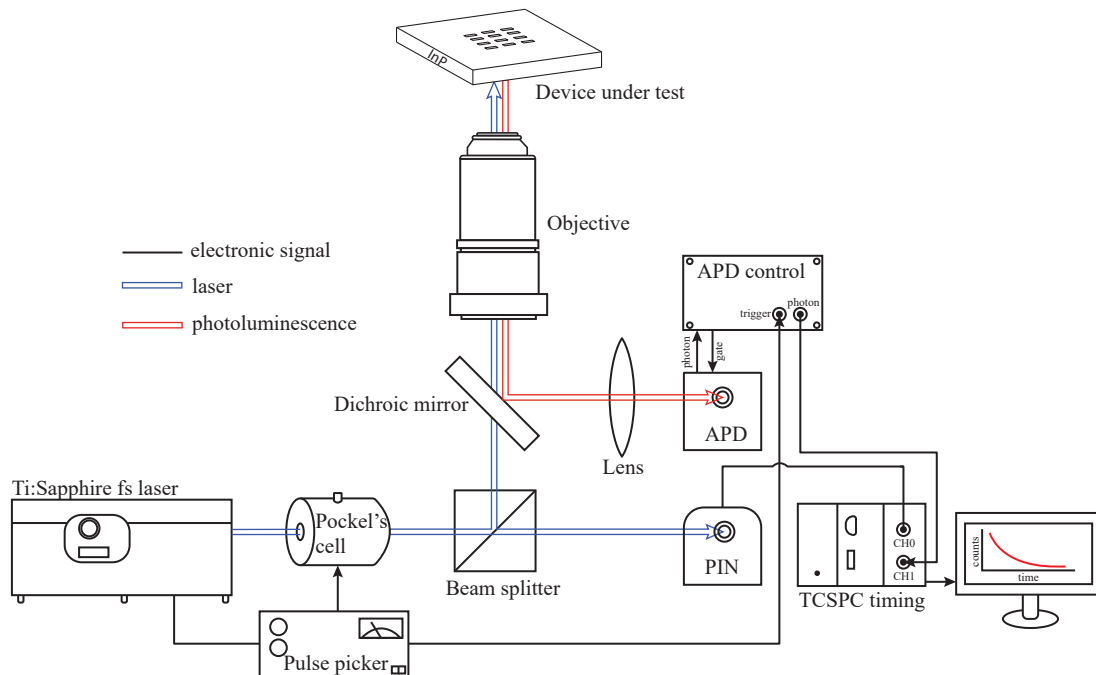


Figure F.2: Block diagram of the TCSPC optical setup at near-IR wavelengths.

### High dark count rate of InGaAs APDs

InGaAs APDs suffer from large dark count rate ($\approx 10,000$ counts per second) due to the low band gap of the material. This becomes a serious issue when compounded with the effect of after-pulsing that is present in InGaAs APDs. During an avalanche event, some carriers may get stuck in trap states for some time after the main avalanche pulse is complete. Eventually, the carriers will become de-trapped and kick off another avalanche pulse leading to an errant triggering of an artificial photon detection; this is called an after-pulse. To avoid this problem, APDs are typically turned off for some time after the first avalanche pulse. This dead-time can be as long as 10s of $\mu$s. Therefore, the InGaAs APD will spend of most of the time turned off because of the high dark count rate if left free-running. Because of

this, InGaAs APDs are usually gated and only turned on during the interval that a photon is expected. In practice, this requires syncing the laser pulse with the gate signal of the APD.

## Experimental setup for TCSPC at near-IR wavelengths

Shown in Figure F.2 is the experimental setup used to measure the lifetime of InP/InGaAs(P) semiconductor ridges in the near-IR. The setup in Figure F.2 is considerably more complex than the simple diagram shown in Figure F.1d because of the addition of the gating. The sample was excited with the output of a Ti:Sapphire femtosecond laser (Coherent Ultra II). Part of the laser pulse was split off and sent to a fast PIN photodiode (Picoquant TDA 200) to trigger the TCSPC timing module (Picoquant Picoharp 300) and establish a time reference. A pulse picker (Conoptics) was used to reduce the repetition rate of the output of a Ti:Sapphire femtosecond laser from 80 MHz to 40 MHz to ensure the period between successive laser pulses was much longer than the decay time of the sample. The sync output of the pulse picker was used trigger the gate and turn-on the InGaAs APD (Micro Photon Devices) in preparation for the arrival of a photon. The gating signal needs to be precisely timed to occur the same time that the laser pulse arrives at the sample; this was achieved through a variable length coaxial cable delay. If a photon was detected by the APD, the gating signal was immediately turned off. Otherwise after 10ns, if no photon was detected, the gate was turned off until the next laser pulse and the cycle was repeated again.

# Appendix G

# Model parameters for the InGaAs quantum well antenna-LED

| Parameter | Description | Value |
| --- | --- | --- |
| Quantum well (InGaAs) | | |
| $E_g$ | bandgap (eV) | 0.755 |
| $d_{qw}$ | thickness (nm) | 5 |
| $m_e$ | electron effective mass ($m_e^*/m_0$) | 0.041 |
| $m_{hh}$ | heavy hole effective mass ($m_{hh}^*/m_0$) | 0.46 |
| $m_{lh}$ | light hole effective mass ($m_{lh}^*/m_0$) | 0.0503 |
| $E_p$ | matrix element energy parameter (eV) | 25.0 |
| $|M|^2$ | matrix element | $(m_0/6)E_p$ |
| $v_s$ | surface recombination velocity (cm/s) | $10^4$ |
| $C_A$ | Auger coefficient ($cm^6/s$) | $10^{-28}$ |
| $n$ | index of refraction | 3.55 |
| Barrier (InGaAsP) | | |
| $E_g$ | bandgap (eV) | 1.03 |
| $d_{sch}$ | thickness (nm) | 100 |
| $m_e$ | electron effective mass ($m_e^*/m_0$) | 0.065 |
| $m_{hh}$ | heavy hole effective mass ($m_{hh}^*/m_0$) | 0.46 |
| $m_{lh}$ | light hole effective mass ($m_{lh}^*/m_0$) | 0.087 |
| $v_s$ | surface recombination velocity (cm/s) | $10^4$ |
| Cladding (InP) | | |
| $E_g$ | bandgap (eV) | 1.34 |
| $m_e$ | electron effective mass ($m_e^*/m_0$) | 0.065 |
| $m_{hh}$ | heavy hole effective mass ($m_{hh}^*/m_0$) | 0.46 |
| $m_{lh}$ | light hole effective mass ($m_{lh}^*/m_0$) | 0.087 |
| $\mu_n$ | electron mobility ($cm^2/V{\cdot}s$) | 1600 |
| $v_s$ | surface recombination velocity (cm/s) | 5000 |
| All semiconductor materials | | |
| CBO | Conduction band offset | $0.4\Delta E_g$ |

Table G.1: Model parameters used for analyzing the quantum well antenna-LED in Chapter 6

# Appendix H

# Derivation of the effect of carrier transport time on modulation speed

In deriving the 3-dB frequency ($f_{3dB}$) in Chapter 6, it was assumed that the carrier density in the active region immediately responds to a change in bias in the electrodes of the antenna-LED. For an antenna-LED with picosecond or shorter spontaneous emission lifetime, this assumption may begin to break down. In this appendix, the full derivation of the $f_{3dB}$ with the inclusion of the transport carrier effect will be given. The analysis largely follows the derivation given for a semiconductor laser in [114] and [132] except without the consideration of gain in the active region.

## H.1   Carrier transport in the antenna-LED

Shown in Figure H.1 is a simplified band structure for an antenna-LED consisting of a quantum well separate confinement heterostructure (SCH) active region. The carrier dynamics that leads to transport of electrons into the active region and an emission of a photon can be qualitatively described as follows.

1. Electrons are injected into the confinement region with current density $J$.

2. Electrons diffuse across the confinement region with transit time $\tau_t$. The density of carriers in the confinement region in the vicinity of the quantum well is given by $n_b$

3. Electrons are captured into the quantum well with capture time $\tau_c$. Electrons may also escape the quantum well with capture time $\tau_e$. The density of carriers in the quantum well is given by $n_{qw}$

4. Electrons recombine with a hole and emit a photon after time $\tau_{qw}$ (or recombine non-radiatively after time $\tau_{nr}$, not shown in Figure H.1).
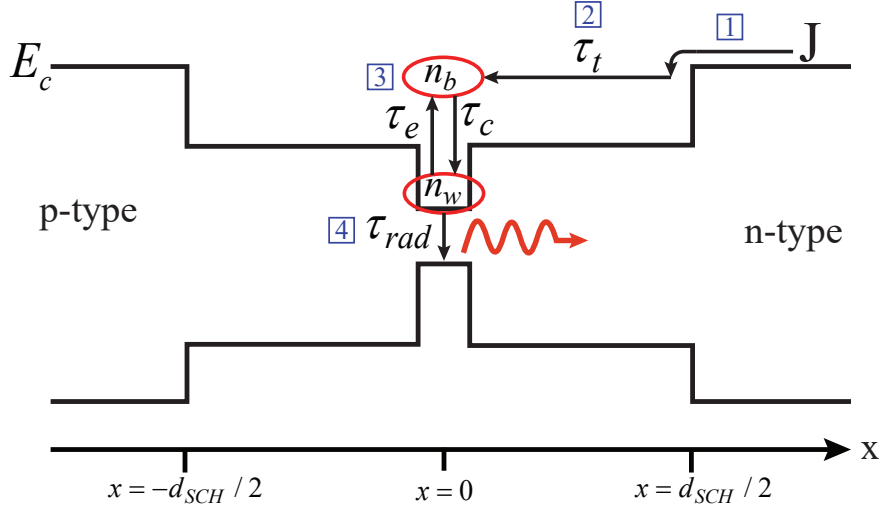
Figure H.1: Carrier transport in the quantum well antenna-LED showing the sequence of carrier transport into the active region

An identical sequence of events also occurs in the valence band. The goal in this appendix is to understand how the transit time ($\tau_t$), capture time ($\tau_c$) and escape time ($\tau_e$) effect the speed of the antenna-LED.

**Coupled rate equations**

A set of coupled rate equations can be written as

$$\frac{J_{qw}}{qd_{qw}} = \frac{n_b}{\tau_c} - \frac{n_{qw}}{\tau_e} \tag{H.1}$$

$$\frac{dn_{qw}}{dt} = \frac{J_{qw}}{qd_{qw}} - \frac{n_w}{\tau_{rad}} - \frac{n_{qw}}{\tau_{nr}} \tag{H.2}$$

$$\frac{dn_b}{dt} = \frac{J_b}{qd_{qw}} - \frac{J_{qw}}{\tau_{rad}} - \frac{n_b}{\tau_{sch}} \tag{H.3}$$

where the undefined variables are given by

$J_{qw}$ = Net current density into the quantum well

$J_b$ = Net current density into the confinement region in the vicinity of the quantum well

$\tau_{sch}$ = Recombination lifetime in the SCH region

$d_{qw}$ = Thickness of the quantum well

Note that for brevity it is assumed that the carrier recombination mechanisms can be modeled as a single rate decay constant.

**Carrier diffusion in the SCH region**

In general, the injected current density ($J$) does not equal the current density that arrives in the SCH region in the vicinity of the quantum well ($J_b$). Carriers that are injected at the edge of the SCH region at ($x = d_{sch}/2$) will diffuse toward the active region by ambipolar diffusion such that

$$\frac{dn_{sch}(x)}{dt} = D_A \frac{d^2 n_{sch}(x)}{dx^2} - \frac{n_{sch}}{\tau_{sch}} \tag{H.4}$$

where $n(x)$ is the position dependent carrier density in the SCH region and $D_A$ is the ambipolar diffusion coefficient. The solution of (H.4) will have the form $n(x) = A\exp(x/L_0) + B\exp(-x/L_0)$ where it is straightforward to show that $L_0 = \left(\frac{D_A \tau_{sch}}{j\omega\tau_{sch}+1}\right)$ if it is assumed that $n(x)$ is time-harmonic. The coefficients $A$ and $B$ can be determined by applying the boundary conditions that the injected carrier density is $J$ at $x = d_{sch}/2$ and that $n(x = 0) = n_b$. After doing so and solving for $J_b$ we find

$$J_b = J\text{sech}(d_{sch}/2L_0) - \frac{qD_A}{L_0}\tanh(d_{sch}/2L_0) \tag{H.5}$$

We would like to know how much incremental increased current density is seen at the barrier ($\Delta J_b$) for an incremental increase in the injected current ($\Delta J$); this is given as

$$\frac{\Delta J_b}{\Delta J} = \text{sech}(d_{sch}/2L_0)$$

$$= \left[\cosh\left(\sqrt{\frac{(d_{sch}/2)^2(j\omega\tau_{sch}+1)}{D_A\tau_{sch}}}\right)\right]$$

$$\approx \frac{1}{1 + \frac{j\omega(d_{sch}/2)^2}{2D_A}} \quad \text{for} \ \ (d_{sch})^2 \ll D_A\tau_{sch}$$

$$= (1 + j\omega\tau_t)^{-1} \quad \text{where} \ \ \tau_t = (d_{sch}/2)^2/(2D_A) \tag{H.6}$$

## Small-signal analysis

Now with a relationship between the injected current density ($J$) and current density in the barrier at the vicinity of the quantum well ($J_b$) the coupled rate equations given in (H.1)-(H.3) can be solved in combination with (H.6) to derive the transfer function for the power ($P$) emitted by the antenna-LED under the small-signal approximation. It can be shown that

$$\frac{\Delta P}{\Delta J} = \frac{V}{d_{qw}}\frac{\tau_{qw}}{\tau_{rad}}\frac{\hbar\omega}{q}B_1 B_3\left(\frac{B_2\frac{\tau_{sch}}{\tau_c}}{1 + B_1\frac{\tau_{rad}}{\tau_e} + B_2\frac{\tau_{sch}}{\tau_c}}\right) \tag{H.7}$$

where

$$\tau_{qw}^{-1} = \tau_{rad}^{-1} + \tau_{nr}^{-1}$$
$$B_1 = (1 + j\omega\tau_{qw})^{-1}$$
$$B_2 = (1 + j\omega\tau_{sch})^{-1}$$
$$B_3 = (1 + j\omega\tau_t)^{-1}$$

Equation (H.7) simplifies considerably under the simplifications that $B_1 \approx 1$ (valid for $\omega < \tau_{rad}^{-1}$), $B_2 \approx (j\omega\tau_{sch})^{-1}$, and $\tau_e \gg \tau_{qw}$ such that

$$\frac{\Delta P}{\Delta J} = \frac{V}{d_{qw}} \frac{\tau_{qw}}{\tau_{rad}} \frac{\hbar\omega}{q} (1 + j\omega\tau_{qw})^{-1}(1 + j\omega\tau_t)^{-1}(1 + j\omega\tau_c)^{-1} \tag{H.8}$$

Thus, the impact of the carrier transport in the antenna-LED can easily be seen. Diffusion of carriers across the SCH region and capture of carriers into the quantum well act like two poles in the transfer function with time constant $\tau_t$ and $\tau_c$ respectively.

(a)                                                          (b)
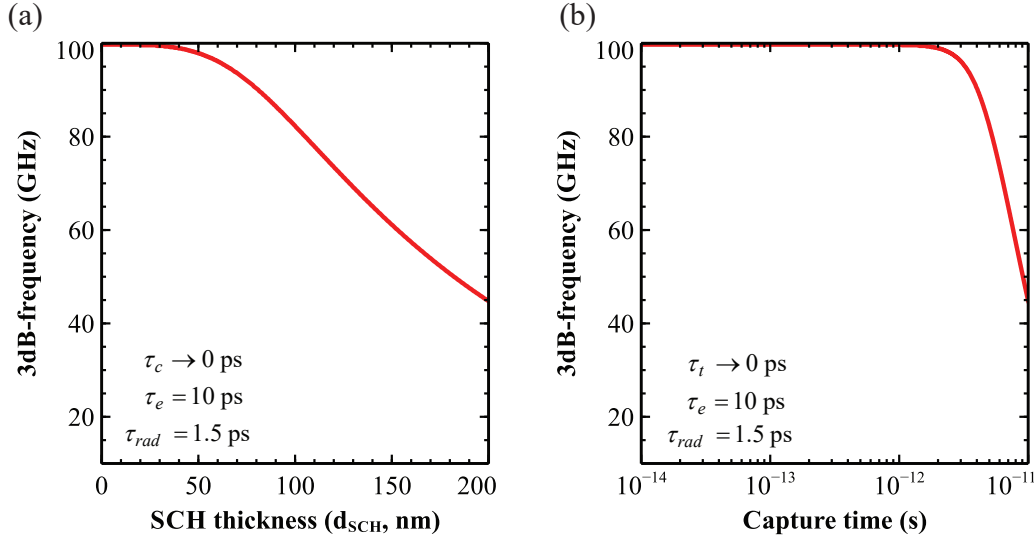


Figure H.2: Plot of the 3dB-frequency showing the effect of (a) carrier transit time and (b) capture time into the quantum well active region.

Two examples are considered in Figure H.2 to illustrate the effect of $\tau_t$ and $\tau_c$ on the 3dB-frequency of the antenna-LED. In the first example shown in Figure H.2a, the transit time $(\tau_t)$ is neglected and the 3dB-frequency is plotted as a function of the SCH thickness $(d_{sch})$ for an antenna-enhanced radiative lifetime of $\tau_{rad} = 1.5$ ps. The impact of finite transit time can be seen for a SCH thickness as small as 50 nm. For a 200 nm thick SCH (typical for a semiconductor laser), the 3dB-frequency has been reduced by a factor of two from 100 to 50 GHz as the result of the transit time. Strategies for engineering the SCH region to minimize the effect of transit time are discussed in the main text.

In the second example shown in Figure H.2b, the transit time is neglected and the 3dB-frequency is plotted as a function of the capture time ($\tau_c$). Not surprisingly, the capture time does not effect the 3dB-frequency until $\tau_c$ is the same order of magnitude $\tau_{rad}$ which in this case is 1.5 ps. It is thought that $\tau_c$ for quantum wells is on the order of $10^{-13}$ s and therefore is expected to be important only for device speeds exceeding a 3dB-frequency of 100 GHz.

# Bibliography

[1] "Scaling up energy efficiency across the data center industry: Evaluating key drivers and barriers," NRDC, Tech. Rep., 2014.

[2] (Feb. 2017). Gartner says 8.4 billion connected "things" will be in use in 2017, up 31 percent from 2016, [Online]. Available: `http://www.gartner.com/newsroom/id/3598917`.

[3] "Cisco visual networking index: Forecast and methodology, 2016-2021," Cisco, Tech. Rep., 2017.

[4] G. Astfalk, "Why optical data communications and why now?" *Applied Physics A*, vol. 95, no. 4, pp. 933–940, Jun. 2009.

[5] C. Helman. (Jun. 2016). Berkeley lab: It takes 70 billion kilowatt hours a year to run the internet, [Online]. Available: `https://www.forbes.com/sites/christopherhelman/2016/06/28/how-much-electricity-does-it-take-to-run-the-internet/#7d0174651fff`.

[6] D. A. B. Miller, "Attojoule optoelectronics for low-energy information processing and communications," *Journal of Lightwave Technology*, vol. 35, no. 3, pp. 346–396, Feb. 2017.

[7] ——, "Device Requirements for Optical Interconnects to Silicon Chips," *Proceedings of the IEEE*, vol. 97, no. 7, pp. 1166–1185, Jul. 2009.

[8] E. Macii, *Ultra Low-Power Electronics and Design*. Springer, 2004.

[9] D. Hodges, H. Jackson, and R. Saleh, *Analysis and Design of Digital Integrated Circuits*, Third edition. Boston: McGraw-Hill Science/Engineering/Math, Jul. 2003.

[10] G. P. Agrawal, *Fiber-Optic Communication Systems*, Fourth edition. New York: Wiley, Oct. 2010.

[11] E. Dulkeith, F. Xia, L. Schares, W. M. J. Green, and Y. A. Vlasov, "Group index and group velocity dispersion in silicon-on-insulator photonic wires," *Optics Express*, vol. 14, no. 9, pp. 3853–3863, May 2006.

[12] S. L. Chuang, *Physics of Photonic Devices*, Second edition. Wiley Publishing, 2009.

[13] K. Yu, A. Lakhani, and M. C. Wu, "Subwavelength metal-optic semiconductor nanopatch lasers," *Optics Express*, vol. 18, no. 9, pp. 8790–8799, Apr. 2010.

[14] M. P. Nezhad, A. Simic, O. Bondarenko, B. Slutsky, A. Mizrahi, L. Feng, V. Lomakin, and Y. Fainman, "Room-temperature subwavelength metallo-dielectric lasers," *Nature Photonics*, vol. 4, no. 6, pp. 395–399, Jun. 2010.

[15] M. T. Hill, Y.-S. Oei, B. Smalbrugge, Y. Zhu, T. d. Vries, P. J. v. Veldhoven, F. W.M. v. Otten, T. J. Eijkemans, J. P. Turkiewicz, H. d. Waardt, E. J. Geluk, S.-H. Kwon, Y.-H. Lee, R. Ntzel, and M. K. Smit, "Lasing in metallic-coated nanocavities," *Nature Photonics*, vol. 1, no. 10, pp. 589–594, 2007.

[16] K. Ding and C. Z. Ning, "Metallic subwavelength-cavity semiconductor nanolasers," *Light: Science & Applications*, vol. 1, no. 7, e20, Jul. 2012.

[17] K. Ding, Z. C. Liu, L. J. Yin, M. T. Hill, M. J. H. Marell, P. J. van Veldhoven, R. Netzel, and C. Z. Ning, "Room-temperature continuous wave lasing in deep-subwavelength metallic cavities under electrical injection," *Physical Review B*, vol. 85, no. 4, p. 041 301, Jan. 2012.

[18] Q. Zhang, G. Li, X. Liu, F. Qian, Y. Li, T. C. Sum, C. M. Lieber, and Q. Xiong, "A room temperature low-threshold ultraviolet plasmonic nanolaser," *Nature Communications; London*, vol. 5, p. 4953, Sep. 2014.

[19] R. F. Oulton, V. J. Sorger, T. Zentgraf, R.-M. Ma, C. Gladden, L. Dai, G. Bartal, and X. Zhang, "Plasmon lasers at deep subwavelength scale," *Nature*, vol. 461, no. 7264, pp. 629–632, Oct. 2009.

[20] Y.-J. Lu, J. Kim, H.-Y. Chen, C. Wu, N. Dabidian, C. E. Sanders, C.-Y. Wang, M.-Y. Lu, B.-H. Li, X. Qiu, W.-H. Chang, L.-J. Chen, G. Shvets, C.-K. Shih, and S. Gwo, "Plasmonic nanolaser using epitaxially grown silver film," *Science*, vol. 337, no. 6093, pp. 450–453, Jul. 2012.

[21] S.-H. Kwon, J.-H. Kang, C. Seassal, S.-K. Kim, P. Regreny, Y.-H. Lee, C. M. Lieber, and H.-G. Park, "Subwavelength plasmonic lasing from a semiconductor nanodisk with silver nanopan cavity," *Nano Letters*, vol. 10, no. 9, pp. 3679–3683, Sep. 2010.

[22] J. Ho, J. Tatebayashi, S. Sergent, C. F. Fong, S. Iwamoto, and Y. Arakawa, "Low-threshold near-infrared GaAs-AlGaAs core-shell nanowire plasmon laser," *ACS Photonics*, vol. 2, no. 1, pp. 165–171, Jan. 2015.

[23] J. B. Khurgin and G. Sun, "Comparative analysis of spasers, vertical-cavity surface-emitting lasers and surface-plasmon-emitting diodes," *Nature Photonics*, vol. 8, no. 6, pp. 468–473, Jun. 2014.

[24] ——, "How small can "nano" be in a "nanolaser"?" *Nanophotonics*, vol. 1, no. 1, pp. 3–8, 2012.

[25] K. Takeda, T. Sato, A. Shinya, K. Nozaki, W. Kobayashi, H. Taniyama, M. Notomi, K. Hasebe, T. Kakitsuka, and S. Matsuo, "Few-fJ/bit data transmissions using directly modulated lambda-scale embedded active region photonic-crystal lasers," *Nature Photonics*, vol. 7, no. 7, pp. 569–575, Jul. 2013.

[26] S. Matsuo, A. Shinya, T. Kakitsuka, K. Nozaki, T. Segawa, T. Sato, Y. Kawaguchi, and M. Notomi, "High-speed ultracompact buried heterostructure photonic-crystal laser with 13fJ of energy consumed per bit transmitted," *Nature Photonics*, vol. 4, no. 9, pp. 648–654, Sep. 2010.

[27] S. Matsuo, K. Takeda, T. Sato, M. Notomi, A. Shinya, K. Nozaki, H. Taniyama, K. Hasebe, and T. Kakitsuka, "Room-temperature continuous-wave operation of lateral current injection wavelength-scale embedded active-region photonic-crystal laser," *Optics Express*, vol. 20, no. 4, pp. 3773–3780, Feb. 2012.

[28] H.-G. Park, S.-H. Kim, S.-H. Kwon, Y.-G. Ju, J.-K. Yang, J.-H. Baek, S.-B. Kim, and Y.-H. Lee, "Electrically driven single-cell photonic crystal laser," *Science*, vol. 305, no. 5689, pp. 1444–1447, Sep. 2004.

[29] B. Ellis, M. A. Mayer, G. Shambat, T. Sarmiento, J. Harris, E. E. Haller, and J. Vukovi, "Ultralow-threshold electrically pumped quantum-dot photonic-crystal nanocavity laser," *Nature Photonics*, vol. 5, no. 5, pp. 297–300, May 2011.

[30] S. Pimputkar, J. S. Speck, S. P. DenBaars, and S. Nakamura, "Prospects for LED lighting," *Nature Photonics*, vol. 3, no. 4, pp. 180–182, Apr. 2009.

[31] P. Anger, P. Bharadwaj, and L. Novotny, "Enhancement and Quenching of Single-Molecule Fluorescence," *Physical Review Letters*, vol. 96, no. 11, p. 113 002, Mar. 2006.

[32] S. Khn, U. Hkanson, L. Rogobete, and V. Sandoghdar, "Enhancement of single-molecule fluorescence using a gold nanoparticle as an optical nanoantenna," *Physical Review Letters*, vol. 97, no. 1, p. 017 402, Jul. 2006.

[33] A. Kinkhabwala, Z. Yu, S. Fan, Y. Avlasevich, K. Mllen, and W. E. Moerner, "Large single-molecule fluorescence enhancements produced by a bowtie nanoantenna," *Nature Photonics*, vol. 3, no. 11, pp. 654–657, Nov. 2009.

[34] P. Bharadwaj and L. Novotny, "Spectral dependence of single molecule fluorescence enhancement," *Optics Express*, vol. 15, no. 21, pp. 14 266–14 274, Oct. 2007.

[35] O. L. Muskens, V. Giannini, J. A. Snchez-Gil, and J. Gmez Rivas, "Strong enhancement of the radiative decay rate of emitters by single plasmonic nanoantennas," *Nano Letters*, vol. 7, no. 9, pp. 2871–2875, Sep. 2007.

[36] T. H. Taminiau, R. J. Moerland, F. B. Segerink, L. Kuipers, and N. F. van Hulst, "$\lambda/4$ resonance of an optical monopole antenna probed by single molecule fluorescence," *Nano Letters*, vol. 7, no. 1, pp. 28–33, Jan. 2007.

[37] J. N. Farahani, D. W. Pohl, H.-J. Eisler, and B. Hecht, "Single quantum dot coupled to a scanning optical antenna: A tunable superemitter," *Physical Review Letters*, vol. 95, no. 1, p. 017 402, Jun. 2005.

[38] H. Mertens, J. S. Biteen, H. A. Atwater, and A. Polman, "Polarization-selective plasmon-enhanced silicon quantum-dot luminescence," *Nano Letters*, vol. 6, no. 11, pp. 2622–2625, Nov. 2006.

[39] T. B. Hoang, G. M. Akselrod, C. Argyropoulos, J. Huang, D. R. Smith, and M. H. Mikkelsen, "Ultrafast spontaneous emission source using plasmonic nanoantennas," *Nature Communications*, vol. 6, p. 7788, Jul. 2015.

[40] M. S. Eggleston, K. Messer, L. Zhang, E. Yablonovitch, and M. C. Wu, "Optical antenna enhanced spontaneous emission," *Proceedings of the National Academy of Sciences*, vol. 112, no. 6, pp. 1704–1709, Feb. 2015.

[41] M. S. Eggleston and M. C. Wu, "Efficient coupling of an antenna-enhanced nanoled into an integrated InP waveguide," *Nano Letters*, vol. 15, no. 5, pp. 3329–3333, May 2015.

[42] J.-H. Song, J. Kim, H. Jang, I. Yong Kim, I. Karnadi, J. Shin, J. H. Shin, and Y.-H. Lee, "Fast and bright spontaneous emission of Er3+ ions in metallic nanocavity," *Nature Communications*, vol. 6, May 2015.

[43] G. M. Akselrod, T. Ming, C. Argyropoulos, T. B. Hoang, Y. Lin, X. Ling, D. R. Smith, J. Kong, and M. H. Mikkelsen, "Leveraging nanocavity harmonics for control of optical processes in 2d semiconductors," *Nano Letters*, vol. 15, no. 5, pp. 3578–3584, May 2015.

[44] D. Arbel, N. Berkovitch, A. Nevet, A. Peer, S. Cohen, D. Ritter, and M. Orenstein, "Light emission rate enhancement from InP MQW by plasmon nano-antenna arrays," *Optics Express*, vol. 19, no. 10, pp. 9807–9813, May 2011.

[45] C.-Y. Cho, M.-K. Kwon, S.-J. Lee, S.-H. Han, J.-W. Kang, S.-E. Kang, D.-Y. Lee, and S.-J. Park, "Surface plasmon-enhanced light-emitting diodes using silver nanoparticles embedded in p-GaN," *Nanotechnology*, vol. 21, no. 20, p. 205 201, May 2010.

[46] D.-M. Yeh, C.-F. Huang, C.-Y. Chen, Y.-C. Lu, and C. C. Yang, "Localized surface plasmon-induced emission enhancement of a green light-emitting diode," *Nanotechnology*, vol. 19, no. 34, p. 345 201, Aug. 2008.

[47] K. Okamoto, I. Niki, A. Shvartser, Y. Narukawa, T. Mukai, and A. Scherer, "Surface-plasmon-enhanced light emitters based on InGaN quantum wells," *Nature Materials*, vol. 3, no. 9, pp. 601–605, Sep. 2004.

[48] A. Neogi, C.-W. Lee, H. O. Everitt, T. Kuroda, A. Tackeuchi, and E. Yablonovitch, "Enhancement of spontaneous recombination rate in a quantum well by resonant surface plasmon coupling," *Physical Review B*, vol. 66, no. 15, p. 153 305, Oct. 2002.

[49] M.-K. Kwon, J.-Y. Kim, B.-H. Kim, I.-K. Park, C.-Y. Cho, C. C. Byeon, and S.-J. Park, "Surface-plasmon-enhanced light-emitting diodes," *Advanced Materials*, vol. 20, no. 7, pp. 1253–1257, Apr. 2008.

[50] D. Fattal, M. Fiorentino, M. Tan, D. Houng, S. Y. Wang, and R. G. Beausoleil, "Design of an efficient light-emitting diode with 10 GHz modulation bandwidth," *Applied Physics Letters*, vol. 93, no. 24, p. 243 501, Dec. 2008.

[51] K. C. Y. Huang, M.-K. Seo, Y. Huo, T. Sarmiento, J. S. Harris, and M. L. Brongersma, "Antenna electrodes for controlling electroluminescence," *Nature Communications*, vol. 3, p. 1005, Aug. 2012.

[52] K. C. Y. Huang, M.-K. Seo, T. Sarmiento, Y. Huo, J. S. Harris, and M. L. Brongersma, "Electrically driven subwavelength optical nanocircuits," *Nature Photonics*, vol. 8, no. 3, pp. 244–249, Mar. 2014.

[53] Y.-S. No, J.-H. Choi, H.-S. Ee, M.-S. Hwang, K.-Y. Jeong, E.-K. Lee, M.-K. Seo, S.-H. Kwon, and H.-G. Park, "A double-strip plasmonic waveguide coupled to an electrically driven nanowire LED," *Nano Letters*, vol. 13, no. 2, pp. 772–776, Feb. 2013.

[54] P. Neutens, L. Lagae, G. Borghs, and P. Van Dorpe, "Electrical excitation of confined surface plasmon polaritons in metallic slot waveguides," *Nano Letters*, vol. 10, no. 4, pp. 1429–1432, Apr. 2010.

[55] J. Li, H. Wei, H. Shen, Z. Wang, Z. Zhao, X. Duan, and H. Xu, "Electrical source of surface plasmon polaritons based on hybrid Au-GaAs QW structures," *Nanoscale*, vol. 5, no. 18, p. 8494, 2013.

[56] J. Kern, R. Kullock, J. Prangsma, M. Emmerling, M. Kamp, and B. Hecht, "Electrically driven optical antennas," *Nature Photonics*, vol. 9, no. 9, pp. 582–586, Sep. 2015.

[57] M. Parzefall, P. Bharadwaj, A. Jain, T. Taniguchi, K. Watanabe, and L. Novotny, "Antenna-coupled photon emission from hexagonal boron nitride tunnel junctions," *Nature Nanotechnology*, vol. 10, no. 12, pp. 1058–1063, Dec. 2015.

[58] E. Purcell, "Spontaneous emission probabilities at radio frequencies," in *Physical Review*, vol. 69, 1946, p. 681.

[59] A. Einstein, "On the quantum theory of radiation," *Physikalische Zeitschrift*, vol. 18, no. 121, 1917.

[60] P. Blood, *Quantum Confined Laser Devices: Optical gain and recombination in semiconductors*. OUP Oxford, Oct. 2015.

[61] P. a. M. Dirac, "The quantum theory of the emission and absorption of radiation," *Proceedings of the Royal Society of London A: Mathematical, Physical and Engineering Sciences*, vol. 114, no. 767, pp. 243–265, Mar. 1927.

[62] A. F. Koenderink, "On the use of Purcell factors for plasmon antennas," *Optics Letters*, vol. 35, no. 24, pp. 4208–4210, Dec. 2010.

[63] C. Sauvan, J. P. Hugonin, I. S. Maksymov, and P. Lalanne, "Theory of the spontaneous optical emission of nanosize photonic and plasmon resonators," *Physical Review Letters*, vol. 110, no. 23, p. 237 401, Jun. 2013.

[64] E. Yablonovitch, "Metal optics: The new frontier," in *SPIE Photonics West*, 2011.

[65] S. Ramo, "Currents induced by electron motion," *Proceedings of the IRE*, vol. 27, no. 9, pp. 584–585, Sep. 1939.

[66] W. Shockley, "Currents to conductors induced by a moving point charge," *Journal of Applied Physics*, vol. 9, no. 10, pp. 635–636, Oct. 1938.

[67] C. A. Balanis, *Antenna Theory: Analysis and Design*, Third edition. Hoboken, NJ: Wiley-Interscience, Apr. 2005.

[68] L. Novotny and N. van Hulst, "Antennas for light," *Nature Photonics*, vol. 5, no. 2, pp. 83–90, Feb. 2011.

[69] P. Mhlschlegel, H.-J. Eisler, O. J. F. Martin, B. Hecht, and D. W. Pohl, "Resonant optical antennas," *Science*, vol. 308, no. 5728, pp. 1607–1609, Jun. 2005.

[70] T. J. Seok, A. Jamshidi, M. Kim, S. Dhuey, A. Lakhani, H. Choo, P. J. Schuck, S. Cabrini, A. M. Schwartzberg, J. Bokor, E. Yablonovitch, and M. C. Wu, "Radiation engineering of optical antennas for maximum field enhancement," *Nano Letters*, vol. 11, no. 7, pp. 2606–2610, Jul. 2011.

[71] T. H. Taminiau, F. D. Stefani, F. B. Segerink, and N. F. v. Hulst, "Optical antennas direct single-molecule emission," *Nature Photonics*, vol. 2, no. 4, pp. 234–237, Apr. 2008.

[72] A. Al and N. Engheta, "Tuning the scattering response of optical nanoantennas with nanocircuit loads," *Nature Photonics*, vol. 2, no. 5, pp. 307–310, May 2008.

[73] J. C. Prangsma, J. Kern, A. G. Knapp, S. Grossmann, M. Emmerling, M. Kamp, and B. Hecht, "Electrically connected resonant optical antennas," *Nano Letters*, vol. 12, no. 8, pp. 3915–3919, Aug. 2012.

[74] J.-M. Jin, *Theory and Computation of Electromagnetic Fields*, First edition. Hoboken, N.J: Wiley-IEEE Press, Nov. 2010.

[75] J. Zhang, W. Zhang, X. Zhu, J. Yang, J. Xu, and D. Yu, "Resonant slot nanoantennas for surface plasmon radiation in optical frequency range," *Applied Physics Letters*, vol. 100, no. 24, p. 241 115, Jun. 2012.

[76] Y. Chen, Y. Chen, J. Chu, and X. Xu, "Bridged bowtie aperture antenna for producing an electromagnetic hot spot," *ACS Photonics*, Jan. 2017.

[77] Q.-H. Park, "Optical antennas and plasmonics," *Contemporary Physics*, vol. 50, no. 2, pp. 407–423, Mar. 2009.

[78] H. Guo, T. P. Meyrath, T. Zentgraf, N. Liu, L. Fu, H. Schweizer, and H. Giessen, "Optical resonances of bowtie slot antennas and their geometry and material dependence," *Optics Express*, vol. 16, no. 11, pp. 7756–7766, May 2008.

[79] H. Booker, "Slot aerials and their relation to complementary wire aerials (Babinet's principle)," *Journal of the Institution of Electrical Engineers - Part IIIA: Radioloca-tion*, vol. 93, no. 4, pp. 620–626, 1946.

[80] M. S. Eggleston, "Metal optics based nanoleds : In search of a fast, efficient, nanoscale light emitter," PhD thesis, UC Berkeley, 2015.

[81] D. M. Pozar, *Microwave Engineering*, Fourth edition. Hoboken, NJ: Wiley, Nov. 2011.

[82] C. Cockrell, "The input admittance of the rectangular cavity-backed slot antenna," *IEEE Transactions on Antennas and Propagation*, vol. 24, no. 3, pp. 288–294, May 1976.

[83] S. A. Fortuna, C. Heidelberger, K. Messer, K. Han, E. A. Fitzgerald, E. Yablonovitch, and M. C. Wu, "Optical antenna enhanced spontaneous emission rate in electrically injected nanoscale III-V LED," in *2016 International Semiconductor Laser Confer-ence (ISLC)*, Sep. 2016, pp. 1–2.

[84] S. A. Fortuna, M. Eggleston, K. Messer, E. Yablonovitch, and M. C. Wu, "Electrically injected nanoled with enhanced spontaneous emission from a cavity backed optical slot antenna," in *2014 IEEE Photonics Conference*, Oct. 2014, pp. 158–159.

[85] S. A. Fortuna, M. S. Eggleston, K. Messer, E. Yablonovitch, and M. C. Wu, "Large spontaneous emission rate enhancement from an electrically-injected nanoLED cou-pled to an optical antenna," in *2015 IEEE Photonics Conference (IPC)*, Oct. 2015, pp. 172–173.

[86] J. Lin, X. Zhao, D. A. Antoniadis, and J. A. d. Alamo, "A novel digital etch technique for deeply scaled III-V MOSFETs," *IEEE Electron Device Letters*, vol. 35, no. 4, pp. 440–442, Apr. 2014.

[87] K. Ding and C. Z. Ning, "Fabrication challenges of electrical injection metallic cavity semiconductor nanolasers," *Semiconductor Science and Technology*, vol. 28, no. 12, p. 124 002, 2013.

[88] K. M. McPeak, S. V. Jayanti, S. J. P. Kress, S. Meyer, S. Iotti, A. Rossinelli, and D. J. Norris, "Plasmonic films can easily be better: Rules and recipes," *ACS Photonics*, vol. 2, no. 3, pp. 326–333, Mar. 2015.

[89] J. Wang, M. S. Gudiksen, X. Duan, Y. Cui, and C. M. Lieber, "Highly polarized photo-luminescence and photodetection from single indium phosphide nanowires," *Science*, vol. 293, no. 5534, pp. 1455–1457, Aug. 2001.

[90] C. Heidelberger, "Unpublished,"

[91] T.-T. D. Tran, H. Sun, K. W. Ng, F. Ren, K. Li, F. Lu, E. Yablonovitch, and C. J. Chang-Hasnain, "High brightness InP micropillars grown on silicon with Fermi level splitting larger than 1 eV," *Nano Letters*, vol. 14, no. 6, pp. 3235–3240, Jun. 2014.

[92] D. Neamen, *Semiconductor Physics And Devices*. McGraw-Hill Education, 2003.

[93] M. Boroditsky, I. Gontijo, M. Jackson, R. Vrijen, E. Yablonovitch, T. Krauss, C.-C. Cheng, A. Scherer, R. Bhat, and M. Krames, "Surface recombination measurements on IIIV candidate materials for nanostructure light-emitting diodes," *Journal of Applied Physics*, vol. 87, no. 7, pp. 3497–3504, Apr. 2000.

[94] H. J. Joyce, J. Wong-Leung, C.-K. Yong, C. J. Docherty, S. Paiman, Q. Gao, H. H. Tan, C. Jagadish, J. Lloyd-Hughes, L. M. Herz, and M. B. Johnston, "Ultralow surface recombination velocity in inp nanowires probed by terahertz spectroscopy," *Nano Letters*, vol. 12, no. 10, pp. 5325–5330, Oct. 2012.

[95] E. Yablonovitch, D. L. Allara, C. C. Chang, T. Gmitter, and T. B. Bright, "Unusually low surface-recombination velocity on silicon and germanium surfaces," *Physical Review Letters*, vol. 57, no. 2, pp. 249–252, Jul. 1986.

[96] E. Yablonovitch, C. J. Sandroff, R. Bhat, and T. Gmitter, "Nearly ideal electronic properties of sulfide coated GaAs surfaces," *Applied Physics Letters*, vol. 51, pp. 439–441, Aug. 1987.

[97] R. Aleksiejunas, M. Sudius, T. Malinauskas, J. Vaitkus, K. Jarasinas, and S. Sakai, "Determination of free carrier bipolar diffusion coefficient and surface recombination velocity of undoped GaN epilayers," *Applied Physics Letters*, vol. 83, no. 6, pp. 1157–1159, Aug. 2003.

[98] A. Higuera-Rodriguez, B. Romeira, S. Birindelli, L. E. Black, E. Smalbrugge, P. J. van Veldhoven, W. M. M. Kessels, M. K. Smit, and A. Fiore, "Ultralow surface recombination velocity in passivated InGaAs/InP nanopillars," *Nano Letters*, vol. 17, no. 4, pp. 2627–2633, Apr. 2017.

[99] X. Miao and X. Li, "Scalable monolithically grown AlGaAs-GaAs planar nanowire high-electron-mobility transistor," *IEEE Electron Device Letters*, vol. 32, no. 9, pp. 1227–1229, Sep. 2011.

[100] L. A. Coldren, S. W. Corzine, and M. L. Masanovic, *Diode Lasers and Photonic Integrated Circuits*, Second edition, K. Chang, Ed. Wiley, Feb. 2012.

[101] J. Hu, A. Nainani, Y. Sun, K. C. Saraswat, and H.-S. Philip Wong, "Impact of fixed charge on metal-insulator-semiconductor barrier height reduction," *Applied Physics Letters*, vol. 99, p. 252 104, Dec. 2011.

[102] Y. Wang, Y.-T. Chen, H. Zhao, F. Xue, F. Zhou, and J. C. Lee, "Improved electrical properties of $HfO_2$-based gate dielectrics on InP substrate using $Al_2O_3/HfO_2$ and $SF_6$ plasma treatment," *Electrochemical and Solid-State Letters*, vol. 14, no. 7, H291–H293, Jul. 2011.

[103] M. Tsuchiya, J. M. Gaines, R. H. Yan, R. J. Simes, P. O. Holtz, L. A. Coldren, and P. M. Petroff, "Optical Anisotropy in a Quantum-Well-Wire Array with Two-Dimensional Quantum Confinement," *Physical Review Letters*, vol. 62, no. 4, pp. 466–469, Jan. 1989.

[104] M. Asada, Y. Miyamoto, and Y. Suematsu, "Theoretical gain of quantum-well wire lasers," *Japanese Journal of Applied Physics*, vol. 24, pp. L95–L97, Feb. 1985.

[105] V. A. Shchukin, N. N. Ledentsov, and D. Bimberg, *Epitaxy of nanostructures*, ser. Nanoscience and technology. Berlin ; New York : Springer, c2004., 2004.

[106] V. C. Elarde and J. J. Coleman, "Nanoscale selective area epitaxy for optoelectronic devices," *Progress in Quantum Electronics*, vol. 31, no. 6, pp. 225–257, Jan. 2007.

[107] V. B. Verma, U. Reddy, N. L. Dias, K. P. Bassett, X. Li, and J. J. Coleman, "Patterned quantum dot molecule laser fabricated by electron beam lithography and wet chemical etching," *IEEE Journal of Quantum Electronics*, vol. 46, no. 12, pp. 1827–1833, Dec. 2010.

[108] M. E. Prise, M. R. Taghizadeh, S. D. Smith, and B. S. Wherrett, "Picosecond measurement of Auger recombination rates in InGaAs," *Applied Physics Letters*, vol. 45, no. 6, pp. 652–654, Sep. 1984.

[109] S. Hausser, G. Fuchs, A. Hangleiter, K. Streubel, and W. T. Tsang, "Auger recombination in bulk and quantum well InGaAs," *Applied Physics Letters*, vol. 56, no. 10, pp. 913–915, Mar. 1990.

[110] T. J. d. Lyon, J. M. Woodall, D. T. McInturff, P. D. Kirchner, J. A. Kash, R. J. S. Bates, R. T. Hodgson, and F. Cardone, "High frequency operation of heavily carbon doped $Ga_{0.51}In_{0.49}P$/GaAs surface emitting light emitting diodes grown by metalorganic molecular beam epitaxy," *Applied Physics Letters*, vol. 59, no. 4, pp. 402–404, Jul. 1991.

[111] T. J. d. Lyon, J. M. Woodall, D. T. McInturff, R. J. S. Bates, J. A. Kash, P. D. Kirchner, and F. Cardone, "Doping concentration dependence of radiance and optical modulation bandwidth in carbon doped $Ga_{0.51}In_{0.49}P$/GaAs light emitting diodes grown by gas source molecular beam epitaxy," *Applied Physics Letters*, vol. 60, no. 3, pp. 353–355, Jan. 1992.

[112] R. K. Ahrenkiel, R. Ellingson, S. Johnston, and M. Wanlass, "Recombination lifetime of $In_{0.53}Ga_{0.47}As$ as a function of doping density," *Applied Physics Letters*, vol. 72, no. 26, pp. 3470–3472, Jun. 1998.

[113] S. A. Fortuna, "Unpublished,"

[114] R. Nagarajan, M. Ishikawa, T. Fukushima, R. S. Geels, and J. E. Bowers, "High speed quantum-well lasers and carrier transport effects," *IEEE Journal of Quantum Electronics*, vol. 28, no. 10, pp. 1990–2008, Oct. 1992.

[115] P. S. Zory, *Quantum Well Lasers*. Academic Press, 1993.

[116] H. Shichijo, R. M. Kolbas, N. Holonyak, R. D. Dupuis, and P. D. Dapkus, "Carrier collection in a semiconductor quantum well," *Solid State Communications*, vol. 27, no. 10, pp. 1029–1032, Sep. 1978.

[117] J. Y. Tang, K. Hess, N. Holonyak Jr., J. J. Coleman, and P. D. Dapkus, "The dynamics of electron-hole collection in quantum well heterostructures," *Journal of Applied Physics*, vol. 53, pp. 6043–6046, Sep. 1982.

[118] B. Deveaud, J. Shah, T. C. Damen, and W. T. Tsang, "Capture of electrons and holes in quantum wells," *Applied Physics Letters*, vol. 52, pp. 1886–1888, May 1988.

[119] J. A. Brum and G. Bastard, "Resonant carrier capture by semiconductor quantum wells," *Physical Review B*, vol. 33, no. 2, pp. 1420–1423, Jan. 1986.

[120] P. W. M. Blom, C. Smit, J. E. M. Haverkort, and J. H. Wolter, "Carrier capture into a semiconductor quantum well," *Physical Review B*, vol. 47, no. 4, pp. 2072–2081, Jan. 1993.

[121] M. W. Knight, J. Fan, F. Capasso, and N. J. Halas, "Influence of excitation and collection geometry on the dark field spectra of individual plasmonic nanostructures," *Optics Express*, vol. 18, no. 3, pp. 2579–2587, Feb. 2010.

[122] M. Hu, C. Novo, A. Funston, H. Wang, H. Staleva, S. Zou, P. Mulvaney, Y. Xia, and G. V. Hartland, "Dark-field microscopy studies of single metal nanoparticles: Understanding the factors that influence the linewidth of the localized surface plasmon resonance," *Journal of Materials Chemistry*, vol. 18, no. 17, pp. 1949–1960, Apr. 2008.

[123] C. Huang, A. Bouhelier, G. Colas des Francs, A. Bruyant, A. Guenot, E. Finot, J.-C. Weeber, and A. Dereux, "Gain, detuning, and radiation patterns of nanoparticle optical antennas," *Physical Review B*, vol. 78, no. 15, p. 155 407, Oct. 2008.

[124] J. J. Mock, D. R. Smith, and S. Schultz, "Local refractive index dependence of plasmon resonance spectra from individual nanoparticles," *Nano Letters*, vol. 3, no. 4, pp. 485–491, Apr. 2003.

[125] A. D. McFarland and R. P. Van Duyne, "Single silver nanoparticles as real-time optical sensors with zeptomole sensitivity," *Nano Letters*, vol. 3, no. 8, pp. 1057–1062, Aug. 2003.

[126] J. J. Mock, M. Barbic, D. R. Smith, D. A. Schultz, and S. Schultz, "Shape effects in plasmon resonance of individual colloidal silver nanoparticles," *The Journal of Chemical Physics*, vol. 116, no. 15, pp. 6755–6759, Apr. 2002.

[127] Logeeswaran VJ, N. P. Kobayashi, M. S. Islam, W. Wu, P. Chaturvedi, N. X. Fang, S. Y. Wang, and R. S. Williams, "Ultrasmooth silver thin films deposited with a germanium nucleation layer," *Nano Letters*, vol. 9, no. 1, pp. 178–182, Jan. 2009.

[128] N. Andrade, "Unpublished,"

[129] P. Wrbel, T. Stefaniuk, M. Trzcinski, A. A. Wronkowska, A. Wronkowski, and T. Szoplik, "Ge wetting layer increases Ohmic plasmon losses in Ag film due to segregation," *ACS Applied Materials & Interfaces*, vol. 7, no. 17, pp. 8999–9005, May 2015.

[130] P. Kapusta, M. Wahl, and R. Erdmann, *Advanced Photon Counting: Applications, Methods, Instrumentation*. Springer, Apr. 2015.

[131] C. M. Natarajan, M. G. Tanner, and R. H. Hadfield, "Superconducting nanowire single-photon detectors: Physics and applications," *Superconductor Science and Technology*, vol. 25, no. 6, p. 063 001, 2012.

[132] S. C. Kan, D. Vassilovski, T. C. Wu, and K. Y. Lau, "On the effects of carrier diffusion and quantum capture in high speed modulation of quantum well lasers," *Applied Physics Letters*, vol. 61, no. 7, pp. 752–754, Aug. 1992.